


University of Alberta

**CMOS OPTICAL MICRO-RADIATOR VACUUM SENSOR**

By

Yuan Ma 

A thesis submitted to the Faculty of Graduate Studies and Research in partial fulfillment  
of the requirements for the degree of Doctor of Philosophy

Department of Electrical and Computer Engineering

Edmonton, Alberta

Fall 2002



National Library  
of Canada

Acquisitions and  
Bibliographic Services

395 Wellington Street  
Ottawa ON K1A 0N4  
Canada

Bibliothèque nationale  
du Canada

Acquisitions et  
services bibliographiques

395, rue Wellington  
Ottawa ON K1A 0N4  
Canada

*Your file Votre référence*

*Our file Notre référence*

The author has granted a non-exclusive licence allowing the National Library of Canada to reproduce, loan, distribute or sell copies of this thesis in microform, paper or electronic formats.

The author retains ownership of the copyright in this thesis. Neither the thesis nor substantial extracts from it may be printed or otherwise reproduced without the author's permission.

L'auteur a accordé une licence non exclusive permettant à la Bibliothèque nationale du Canada de reproduire, prêter, distribuer ou vendre des copies de cette thèse sous la forme de microfiche/film, de reproduction sur papier ou sur format électronique.

L'auteur conserve la propriété du droit d'auteur qui protège cette thèse. Ni la thèse ni des extraits substantiels de celle-ci ne doivent être imprimés ou autrement reproduits sans son autorisation.

0-612-81230-8

**Canada**

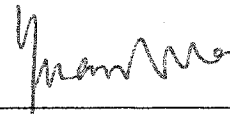
**University of Alberta**

**Library Release Form**

**Name of Author:** Yuan Ma  
**Title of Thesis:** CMOS Optical Micro-Radiator Vacuum Sensor  
**Degree:** Doctor of Philosophy  
**Year this Degree Granted:** 2002

Permission is hereby granted to the University of Alberta Library to reproduce single copies of this thesis and to lend or sell such copies for private, scholarly or scientific research purposes only.

The author reserves all other publication and other rights in association with the copyright in the thesis, and except as herein before provided, neither the thesis nor any substantial portion thereof may be printed or otherwise reproduced in any material from whatever without the author's prior written permission.



---

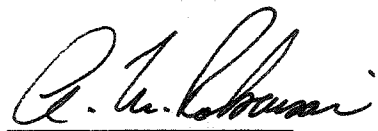
40 Greatwood Cr.  
Nepean, ON  
Canada K2G 6T7

Date: 13 May, 2002

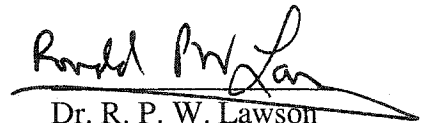
University of Alberta

Faculty of Graduate Studies and Research

The undersigned certify that they have read, and recommend to the Faculty of Graduate Studies and Research for acceptance, a thesis entitled *CMOS Optical Micro-Radiator Vacuum Sensor* submitted by *Yuan Ma* in partial fulfillment of the requirements for the degree of Doctor of Philosophy.



Dr. A. M. Robinson



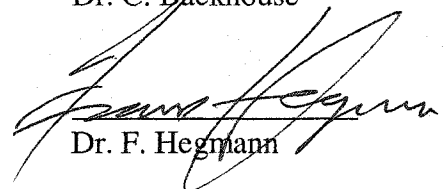
Dr. R. P. W. Lawson



Dr. M. Brett



Dr. C. Backhouse



Dr. F. Hegmann



Dr. T. Hubbard

Dalhousie University

Date: 13 May 2002

## ABSTRACT

The purpose of this project is to develop a high sensitivity vacuum gas sensor using Complementary Metal Oxide Silicon (CMOS) micromachining technology.

A CMOS optical micro-radiator vacuum sensor has been designed, tested and calibrated. The package is comprised of a micromachined radiator and a photodetector. The measurement technique for this device involves an automated system.

MEMS technology helps to lower the power consumption of the device and minimizes the characteristic dimension of the system. Monitoring the radiation improves the sensitivity of measurement by several orders of magnitude compared to the conventional technique of measuring the resistance variation. A power-switching scheme has been introduced to increase the pressure measurement range and extend the lifetime of the device.

A three-mode CMOS photodetector has been designed and tested for the purpose of integration of the system. Output of the photodetector is proportional to the sensitive area of the device and varies linearly with the intensity of incident light.

An automated system has been demonstrated for pressure sensing with constant photodetector output. Calibration of the system has been performed by comparison with secondary standards. Experimental results showed a measurement range from  $10^{-3}$  Pa to  $10^5$  Pa and relative error is less than 8% compared with secondary standards.

Analytical and numerical modeling packages have been used to obtain the photodetector response with the pressure variation and temperature distribution of the device. Simulation results demonstrated a good agreement with experimental data.

## ACKNOWLEDGEMENTS

I would like to express my sincere gratitude to my supervisors, Dr. A. M. Robinson and Dr. R. P. W. Lawson, for their continuous guidance, encouragement and patience throughout this research work, without whom this thesis would not be possible. Special appreciation should be extended to Dr. W. Allegretto, Dr. F. Vermeulen, Dr. M. Brett, Dr. C. Backhouse and Dr. F. Hegmann, for their enlightening discussions and help in various areas.

I gratefully acknowledge the assistance from R. Schmaus, G. Braybrook, S. Kennedy and K. Lui. K. Brown, D. Lu, S. Esteves, and M. Hu provided tremendous help, which is greatly appreciated.

I thank my husband Qiang for his understanding and support, my daughter Annie for bringing happiness into difficult times. Finally, my heartfelt gratitude goes to my parents. This thesis is dedicated to them.

# CONTENTS

<b>1 Introduction</b>	<b>1</b>
1.1 CMOS micromachining	1
1.2 Thermal conductivity gauge	2
1.3 Thermal radiation	5
1.4 Thesis overview	9
References	10
<b>2 CMOS Micromachining and MEMS Design Packages</b>	<b>12</b>
2.1 A typical CMOS micromachining process	12
2.2 MEMS design packages	15
2.2.1 Mentor Graphics MEMS design kit	16
2.2.2 Cadence IC layout editor and Multi-User MEMS Processes (MUMPS) design kit for Cadence	17
2.2.3 MEMSCAP® MEMS Pro	17
References	19
<b>3 CMOS Optical Micro-Radiator</b>	<b>21</b>
3.1 CMOS optical micro-radiator	21
3.2 Micro-radiator electro-thermal model	24

3.2.1	Conduction heat loss through the gas and through the supports	26
3.2.2	Convection heat loss	29
3.2.3	Radiation heat loss	30
3.2.4	Total heat loss	30
3.2.5	Thermal conductivity gauge useful range	33
	References	35
<b>4</b>	<b>Experiment Configuration and Measurement Sensitivity</b>	<b>37</b>
4.1	Variable pressure chamber	37
4.2	Photodiode and point source of light	39
4.3	Digital constant power supply unit and data acquisition unit	44
4.3.1	Test of constant power supply unit	47
4.3.2	Test of experiment control unit	51
4.4	Measurement sensitivity	53
	References	58
<b>5</b>	<b>Device Characterization</b>	<b>59</b>
5.1	Micro-radiator radiation measurement	59
5.1.1	Micro-radiator radiation response with input power	59
5.1.2	Micro-radiator radiation spectral analysis	61
5.1.3	Micro-radiator radiation spatial distribution	67
5.2	Reliability study of polysilicon	69
	References	75



<b>6 Vacuum Pressure Sensing and Power-Switching Scheme</b>	<b>76</b>
6.1 Micro-radiator radiation response with pressure	76
6.2 Power-Switching Scheme	81
6.3 Calibration by comparison	87
6.3.1 Calibration curves	87
6.3.2 System automation	89
6.3.3 Test results	91
6.3.4 Factors that affect the calibration	92
References	94
<b>7 CMOS Photodetector Design</b>	<b>95</b>
7.1 P-N junction and photodiode	95
7.2 Phototransistor	100
7.3 Three-mode CMOS photodetector design	102
7.4 Test of three-mode CMOS photodetector	106
7.4.1 Test with a point light source	106
7.4.2 Test with a laser diode	106
7.5.3 Test with a micro-radiator	110
7.5 Noise in CMOS photodetector	112
7.6 Integration of the micro-radiator and photodetector	112
References	115

<b>8 Numerical Modeling</b>	<b>116</b>
8.1 Model building	117
8.2 Temperature distribution analysis	118
8.3 Radiation calculation	123
References	124
<b>9 Conclusions and Future Work</b>	<b>125</b>
9.1 Conclusions	125
9.2 Future work	126
9.2.1 Micro-radiator matrix design	126
9.2.2 Variation of the characteristic dimension of the system	127
9.2.3 Integration of the system	128
9.2.4 Gas analysis using micro-radiator pressure sensing system	128
References	128
<b>Appendix A Micro-radiator electro-thermal model analysis</b>	<b>129</b>
<b>Appendix B Experiment control system</b>	<b>131</b>
B.1 User interface	131
B.2 Experiment control system flow chart	133
B.3 Experiment control system program	135
<b>Appendix C Automated pressure measurement system program</b>	<b>147</b>
<b>Appendix D ANSYS input file</b>	<b>149</b>

## List of Tables

5.1 Optical filters and lock-in amplifier output	63
6.1 J-K flip-flop truth table	82
6.2 Parameter table for Figure 6.4	83
6.3 Typical measurement results using calibration curve obtained from same device	91
7.1 Function table of three-mode photodetector	105
8.1 Tables of thermo-physical properties	118

## List of Figures

1.1 Heat transfer regimes in a thermal conductivity gauge	3
1.2 Spectrum of electromagnetic radiation	7
1.3 Spectral blackbody emissive power	8
2.1 Cross-section of a wafer of a typical CMOS micromachining fabrication	13
2.2 Cross-section of a typical MEMS structure released with $\text{XeF}_2$	15
2.3 L-Edit user interface with a polysilicon resistor layout as an example	18
3.1 SEM picture of a serpentine-shaped polysilicon micro-radiator	22
3.2 Micro-radiator layout (A) and cross-sectional diagram (B)	24
3.3 Heat transfer related to the micro-radiator	25
3.4 A simplified micro-radiator structure	26
3.5 Average temperature of the micro-radiator versus the surrounding gas pressure operating at a power of 10 mW	32
3.6 Temperature variation of a typical thermal-conductivity gauge operating at constant power inputs of 10 mW and 50 mW	34
4.1 Experiment setup	38
4.2 Response data for silicon photodiode 13 DAS 011/C	39
4.3 Spherical wavefronts produced by a point source of light at O	41
4.4 Schematic of point source of light	42
4.5 Photodetector signal versus inverse distance squared of the light source	43
4.6 Variation of photodetector signal versus time operating with constant	

current at atmospheric pressure	45
4.7 Variation of photodetector signal versus time operating with constant voltage at atmospheric pressure	45
4.8 Photodetector signal (bottom) showing the radiation follows in a non-linear fashion the variation of the power supplied to the micro-radiator (top)	46
4.9 (a) Test of digital constant power supply unit with step function power output	49
4.9 (b) Test of digital constant power supply unit showing the "homing-in" procedure of the system	49
4.10 Test of constant power system operating at different powers	50
4.11 Magnified part of Figure 4.8 showing the details of photodetector and power signal	52
4.12 Extrapolated response of silicon photodetector 13 DAS 011/C	54
4.13 Comparison of the photodetector output with the total radiation and resistance of the micro-radiator as a function of temperature	55
4.14 Micro-radiator temperature and photodetector output versus pressure operating at input powers of 10 and 50 mW	57
5.1 Experiment setup for radiation measurement	60
5.2 Photodetector signal versus the micro-radiator input power ( $\theta = 0$ )	61
5.3 Apparatus used for radiation spectral analysis	62
5.4 Normalized spectral distribution of a micro-radiator with 50 mW input power. The points are measured values	64
5.5 Spectral emissive power analysis experiment setup	66
5.6 Spectral emissive power of the micro-radiator from 650 nm to 1200 nm	67

5.7 Normalized angular radiant intensity of a micro-radiator as a function of the incidence angle $\theta$	68
5.8 (a) Voltage-current characteristics of micro-radiator for a current from 0 to 2 mA	69
5.8 (b) Voltage-current characteristics of micro-radiator for a current from 0 to 3 mA	70
5.9 (a) Resistance of micro-radiator as a function of input current from sweep 1,4,6 and 10 of Figure 5.8 (b)	73
5.9 (b) Resistance of micro-radiator as a function of power input	73
5.9 (c) Temperature versus input power curves for the first and last sweep	74
6.1 Photodetector signal versus pressure under a constant power of 10 mW	78
6.2 Analytical simulation compared with experimental results	79
6.3 Analytical simulation and experimental results showing photodetector signal versus pressure operating at constant powers of 10 and 20 mW	80
6.4 Photodetector signal versus pressure operating at different constant powers showing power-switching scheme	84
6.5 Conceptual diagram of power switching scheme	85
6.6 Relationship between parameter $k$ and the applied power	85
6.7 Relationship between parameter $B$ and the applied power	86
6.8 Power consumption of the micro-radiator versus the pressure with constant photodetector output of 1 and 3 $\mu\text{A}$	86
6.9 (a) A typical calibration curve with data below 33.5 mW being fitted onto a polynomial curve	88

6.9 (b) A typical calibration curve with data above 33.5 mW being fitted onto a polynomial curve	88
6.10 Flow-chart of the pressure measurement system	90
6.11 Photodetector signal versus pressure with different distance between micro-radiator and photodetector	92
6.12 Photodetector outputs for air and He	94
7.1 (a) An idealized model of the p-n junction without bias showing the neutral and depletion areas	97
7.1 (b) A schematic showing various current and particle flow components in the P-N diode at equilibrium	97
7.2 (a) Optical generation of carriers in a P-N junction	99
7.2 (b) P-N junction symbol	99
7.2 (c) I-V characteristics of an illuminated junction	99
7.3 Schematic of an n-p-n transistor showing hole and electron flow	101
7.4 Structure and equivalent circuits of the CMOS multi-mode photodetector	103
7.5 Structure and equivalent circuit of the three-mode photodetector	104
7.6 (a) Output of photodetector working in photodiode mode versus inverse distance squared of the light source	107
7.6 (b) Output of photodetector working in phototransistor mode versus inverse distance squared of the light source	107
7.7 Measured response of the CMOS photodetector operating in different modes	109
7.8 Comparison of CMOS photodetector output with two different sensitive areas in the ratio of 8.7:1	109

7.9 Output of CMOS photodetector working in phototransistor mode versus power input of micro-radiator	111
7.10 Output of CMOS photodetector working in phototransistor mode versus pressure	111
7.11 Integration of the photodetector and micro-radiator with flip-chip technique	113
7.12 The joined micro-radiator / photodetector pair is die-attached and wire-bonded to a DIP	114
7.13 Assembling of the photodetector and micro-radiator with two DIPs	115
8.1 Micro-radiator model built in ANSYS	117
8.2 Temperature distributions operating at a power of 15 mW at $10^{-3}$ Pa simulated with Allegretto's package	119
8.3 Temperature distributions operating at a power of 15 mW at $10^{-3}$ Pa simulated with ANSYS	119
8.4 Temperature distributions operating at a power of 15 mW at $10^5$ Pa simulated with Allegretto's package	121
8.5 Temperature distributions operating at a power of 15 mW at $10^5$ Pa simulated with ANSYS	121
8.6 Picture of burnt out micro-radiator showing the hottest point at the center of the platform at $10^5$ Pa	122
8.7 Picture of micro-radiator at $10^{-3}$ Pa showing the hottest point at two corners of the platform without supporting arms	122
8.8 Allegretto's simulated photodetector output compared with experimental data	123



9.1 Micro-radiator matrix ( $2^n \times 2^m$ ) design	127
B.1 Constant power supply unit user interface	132
B.2 Simplified flow-chart of the digital constant power supply unit and data acquisition unit	134

## List of Symbols

$\alpha$	accommodation coefficient
$\alpha_T, \beta_T$	temperature coefficients of resistance
$\beta$	coefficient of thermal expansion
$\gamma$	ratio of specific heats $C_p / C_v$
$\varepsilon$	emissivity
$\eta$	coefficient to account for first order approximation
$\eta_s$	coefficient to account for the number of micro-radiator supports
$\theta$	incident angle of light
$\kappa$	proportional constant to account for the photodetector-radiator geometry
$\lambda$	optical wavelength
$\lambda_{mfp}$	mean free path
$\mu$	dynamic viscosity
$\nu$	kinematic viscosity
$\rho$	mass density
$\sigma$	Stefan-Boltzmann constant
$\tau$	time constant
$\phi$	azimuth angle
$\chi$	thermal diffusivity
$a$	molecular diameter
$A$	diode cross-sectional area
$A_s$	cross-section area of micro-radiator support
$c_0$	speed of light in vacuum
$C_p$	specific heat at constant pressure
$C_v$	specific heat at constant volume
$d$	characteristic dimension of micro-radiator
$d_c$	critical dimension defined as the ratio of surface area to perimeter
$D$	chamber diameter
$e$	length of micro-radiator support
$E_b$	emissive power of a blackbody
$E_{\lambda,b}$	spectral distribution of blackbody emission
$g$	acceleration of gravity
$g_{op}$	excess carrier generation rate in a photodiode
$Gr$	Grashof number
$h$	Planck constant
$h(v,p)$	convective heat-transfer coefficient
$H$	heat flow
$I_0$	constant current
$I_d$	photodetector output
$I_{op}$	photocurrent
$J$	light intensity
$k$	thermal conductivity
$K$	free molecule conductivity

$k_0$	Boltzmann constant
$Kn$	Knudsen's number
$k_s$	thermal conductivity of the support arm material
$L_n$	diffusion length of electron
$L_p$	diffusion length of hole
$m$	mass of gas molecule
$p$	pressure
$P$	power
$Pr$	Prandtl number
$\dot{Q}$	total heat loss
$r, r'$	radius of spherical wavefronts
$R$	resistance
$R_0$	room temperature resistance
$Ra$	Rayleigh number
$s$	distance from micro-radiator to silicon substrate
$t$	time
$T$	absolute temperature
$T_0$	room temperature
$T_g$	average temperature of the gas far from the micro-radiator
$T_g'$	average temperature of gas molecule arrival at the micro-radiator
$T''$	average temperature of gas molecule departure from the micro-radiator
$T_s$	temperature of silicon substrate
$V_0$	constant voltage
$W$	input power
$W_{cm}$	conduction heat loss through the gas
$W_{cs}$	conduction heat loss through the supports
$W_r$	radiation heat loss
$W_v$	convection heat loss
$x, y$	micro-radiator dimension

# Chapter 1

## Introduction

Micro-fabrication technologies are shrinking devices into micro- and nanometer scales [1-2]. Many interesting and potentially useful micro-electro-mechanical sensors and actuators have been produced by these technologies. Pressure sensors have been predicted to capture the lion's share of the micro-system market for some time [3-4]. In this project, a highly sensitive optical radiator vacuum sensor system has been designed, fabricated with Complementary Metal Oxide Silicon (CMOS) micromachining technology, and tested. Micromachining technology helps to lower the power consumption of the sensor to the 10 mW range. With a power-switching scheme introduced in this thesis, the optical sensor system is capable of measuring pressure from  $10^5$  Pa down to  $10^{-3}$  Pa, with a sensitivity several orders of magnitude better than conventional Pirani type vacuum gauges. Background information related to this project includes CMOS micromachining, thermal conductivity pressure gauges and thermal radiation. A brief introduction on each part is given in this chapter. An overview of the whole thesis is given at the end of this chapter.

### **1.1 CMOS micromachining**

Micromachining is also called MicroElectroMechanical Systems (MEMS) in North America and Micro-Systems Technology (MST) in Europe. MEMS refers to the micro-devices or systems that combine mechanical, electrical, magnetic, thermal and other physical phenomena to form precision systems. These systems can sense, control, and actuate on the micro-scale, and function individually or in arrays to generate effects on

the macro-scale. Most micromachining fabrication technologies are borrowed from the microelectronics industry. The microelectronics fabrication process has the potential of producing large quantity micromachined systems at low cost. Post-processing steps of selective etching of silicon are added after the fabrication process in order to release microstructures, making them freestanding.

Over the past decades, CMOS integrated circuits have become a mainstream technology for VLSI system design. Parameswaran initiated CMOS micromachining in 1989 by implementing unconventional layout designs in standard CMOS Integrated Circuit (CMOSIC) technology without altering the process sequence [5]. A single post-processing etching step was introduced to release microstructures on a CMOS IC without affecting the circuitry formed on the chip. Compared to the other non-standard microfabrication methods, CMOS micromachining has the advantages of a high degree of reliability and repeatability because of well-defined CMOS IC process parameters.

Standard CMOS IC processes can be accessed by universities through the Canadian Microelectronics Corporation (CMC) in Canada, which provides a fruitful environment for CMOS micromachining research and development.

## **1.2 Thermal conductivity gauge**

The thermal conductivity  $k$  of a substance is defined by

$$k = -H / \frac{dT}{ds} \quad (1.1)$$

in which  $H$  is the amount of heat flowing per unit area per second in the direction parallel to  $s$ , and  $dT/ds$  is the temperature gradient in this direction [6].

The thermal conductivity gauge is one of the most commonly used vacuum pressure gauges. The gauge depends on the loss of heat from a hot wire to its surroundings. The hot wire in a gaseous environment loses heat in four ways: (1) radiation, (2) conduction to supports, (3) conduction to the gas, and (4) convection.

The heat transfer regimes in a thermal conductivity gauge are illustrated in Figure 1.1 [7].  $Kn$  is Knudsen's number, defined as the ratio of the mean free path  $\lambda_{mfp}$  of the gas molecules to the characteristic dimension  $d$  of the system, which is defined as the diameter of the hot wire here. The mean free path  $\lambda_{mfp}$  of the gas molecules is defined as the mean distance traveled by a gas molecule between collisions. In terms of the pressure  $p$ ,  $\lambda_{mfp}$  can be expressed by [6]:

$$\lambda_{mfp} = \frac{k_0 T}{\sqrt{2} \pi a^2 p} \quad (1.2)$$

where  $k_0 = 1.3805 \times 10^{-23}$  J/K is the Boltzmann constant,  $T$  is the absolute temperature, and  $a$  is the molecular diameter.

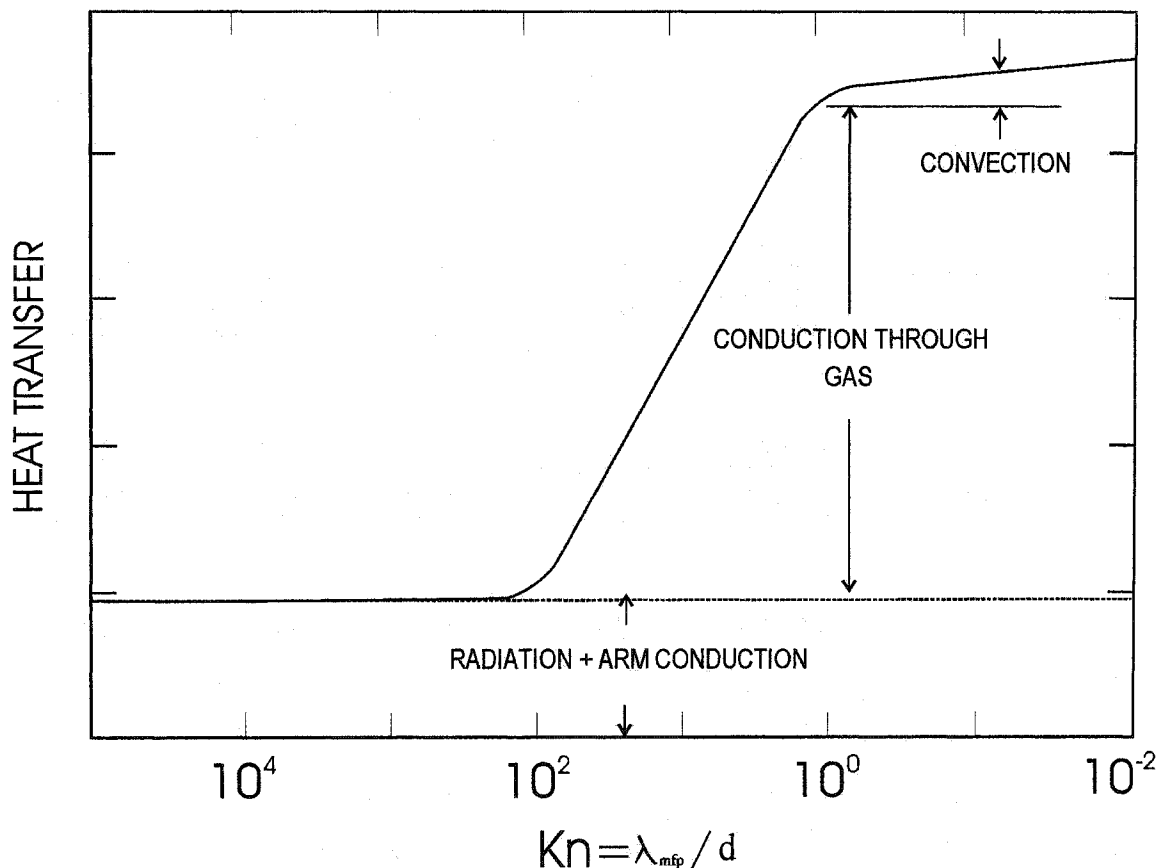


Figure 1.1 Heat transfer regimes in a thermal conductivity gauge

At high pressures where  $Kn < 1$ , the heat flow is independent of pressure except for a small convection effect. In the pressure range where  $1 < Kn < 100$ , the conduction heat loss from the hot filament to the molecules of surrounding gas dominates the heat transfer and is pressure dependent. It is this effect that is used to make a thermal-conductivity-based pressure gauge. In the lowest pressure region where  $Kn > 10^2$ , the heat flow is predominantly accounted for by radiation and conduction through the wire to the supports. If we assume the average temperature of the wire is kept constant at different pressures, radiation and conduction through the supports establish a constant background loss. The magnitude and stability of this background determine the lowest useful pressure of the gauge.

Two common types of thermal conductivity gauges are the thermocouple gauge and the Pirani gauge.

The thermocouple pressure gauge measures the temperature variation of a hot filament, as the pressure changes, by using a thermocouple. The Pirani gauge, on the other hand, measures the electrical resistance of the hot filament and calibrates this resistance change as a function of the gas pressure.

In recent years, some work has been reported on micromachined Pirani-type pressure sensors [8-10]. The principle of operation of these sensors is based on the resistance variation of a temperature-sensitive resistive element, e.g. polysilicon. As the pressure in the gauge tube increases, the thermal conduction of the gas surrounding the hot filament increases, and therefore the temperature of the filament tends to decrease. The electrical resistance of the filament varies with the temperature and is measured to reflect the pressure change. The resistance-temperature characteristics for a material at temperature  $T$  may be expressed by

$$R = R_0[1 + \alpha_T(T - T_0)] \quad (1.3)$$

where  $\alpha_T$  is the temperature coefficient of resistance (TCR) and  $\alpha_T \cong 1 \times 10^{-3} \text{ K}^{-1}$  for polysilicon.  $R_0$  is the resistance at reference temperature  $T_0$ . The pressure measurement range of these sensors is from  $10^{-1} \text{ Pa}$  to  $10^4 \text{ Pa}$  [9].

In contrast to previous work, this project describes a micromachined thermal conductivity sensor based on the thermal radiation emitted from a thermally isolated polysilicon micro-radiator and the photodetector measurement. In the initial work done by Kleckner *et al.* [11], the authors claim that monitoring the radiation to measure gas pressure changes should be four times as sensitive as conventional Pirani gauge. In fact, the sensitivity of this method will be much better than that due to photodetector spectral response. This will be discussed in detail in Chapter 4.

### **1.3 Thermal radiation**

Radiation is the emission of either particles or electromagnetic rays from a source [12]. It is usual to classify radiation according to its frequency or wavelength as a fundamental property. Figure 1.2 shows the spectrum of radiation from the highest energy cosmic ray particles (with shortest wavelength) down to the lowest energy radio waves (with longest wavelength).

The intermediate portion of the spectrum, which extends from approximately  $10^{-7}$  m to  $10^{-4}$  m, is termed thermal radiation and is pertinent to heat transfer. Thermal radiation includes a portion of the ultraviolet, all of the visible and the infrared. Visible radiation (normally called light) can be detected by the human eye, and has a wavelength from 400 nm to 700 nm.

When describing the radiation characteristics of real surfaces, it usually involves the concept of a blackbody. A blackbody is an ideal surface having the following properties [13]:

1. A blackbody absorbs all incident radiation, regardless of wavelength and direction.
2. For a prescribed temperature and wavelength, no surface can emit more energy than a blackbody.
3. Although the radiation emitted by a blackbody is a function of wavelength and temperature, it is independent of direction. This kind of emitter is usually called a diffuse emitter.



The spectral distribution of blackbody emission  $E_{\lambda,b}$  refers to the power per unit area of the blackbody surface radiated in all directions per unit wavelength with units of  $W/(m^2 \cdot \mu m)$ . It is a function of the absolute temperature and radiation wavelength of the blackbody. The emission  $E_{\lambda,b}$  can be described by the Planck distribution [14]:

$$E_{\lambda,b}(\lambda, T) = \frac{2\pi h c_0^2}{\lambda^5 (e^{\frac{hc_0}{\lambda k_0 T}} - 1)} \quad (1.4)$$

where  $h = 6.6256 \times 10^{-34}$  J·s and  $k_0 = 1.3805 \times 10^{-23}$  J/K are the universal Planck and Boltzmann constants, respectively,  $c_0 = 2.998 \times 10^8$  m/s is the speed of light in vacuum,  $T$  is the absolute temperature (K), and  $\lambda$  is the wavelength ( $\mu m$ ). Planck distributions are plotted in Figure 1.3 for selected temperatures using MatLab.

The total emissive power of a blackbody,  $E_b$ , can be calculated by integrating equation (1.4) over the wavelength range from 0 to  $\infty$ . The result is called Stefan-Boltzmann law:

$$E_b = \sigma T^4 \quad (1.5)$$

in which  $\sigma$  is called the Stefan-Boltzmann constant, and has the numerical value

$$\sigma = 5.670 \times 10^{-8} W / m^2 \cdot K^4$$

Real surface emission differs from the Planck distribution. The ratio of the radiation emitted by a real surface to the radiation emitted by a blackbody at the same temperature is defined as the emissivity  $\varepsilon$ . Typical values of some commonly used materials can be found in engineering handbooks, e.g. CRC Handbook of Chemistry and Physics.

Usually the emissivity is a function of temperature and wavelength. However, the emissivity of silicon dioxide, the surface material of the micro-radiator studied in this project, is relatively constant with temperature and wavelength. Therefore, a constant value of 0.8 is used in this thesis for the simplicity of calculation [13].

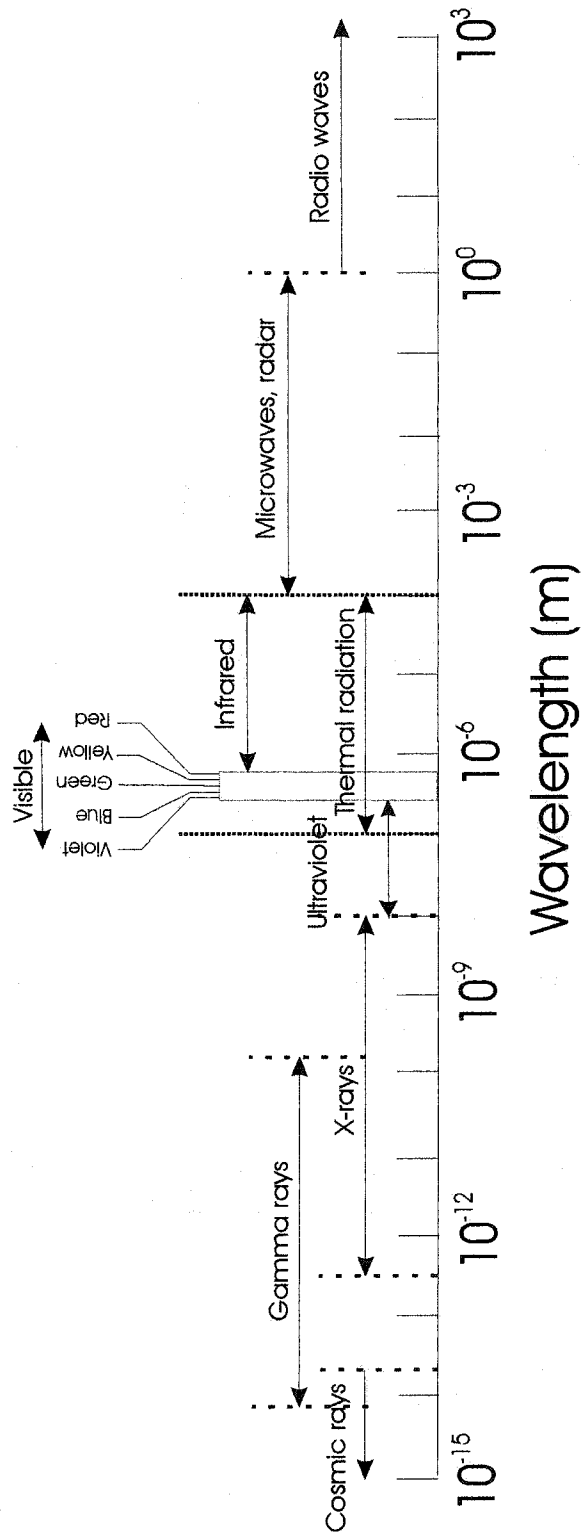


Figure 1.2 Spectrum of electromagnetic radiation

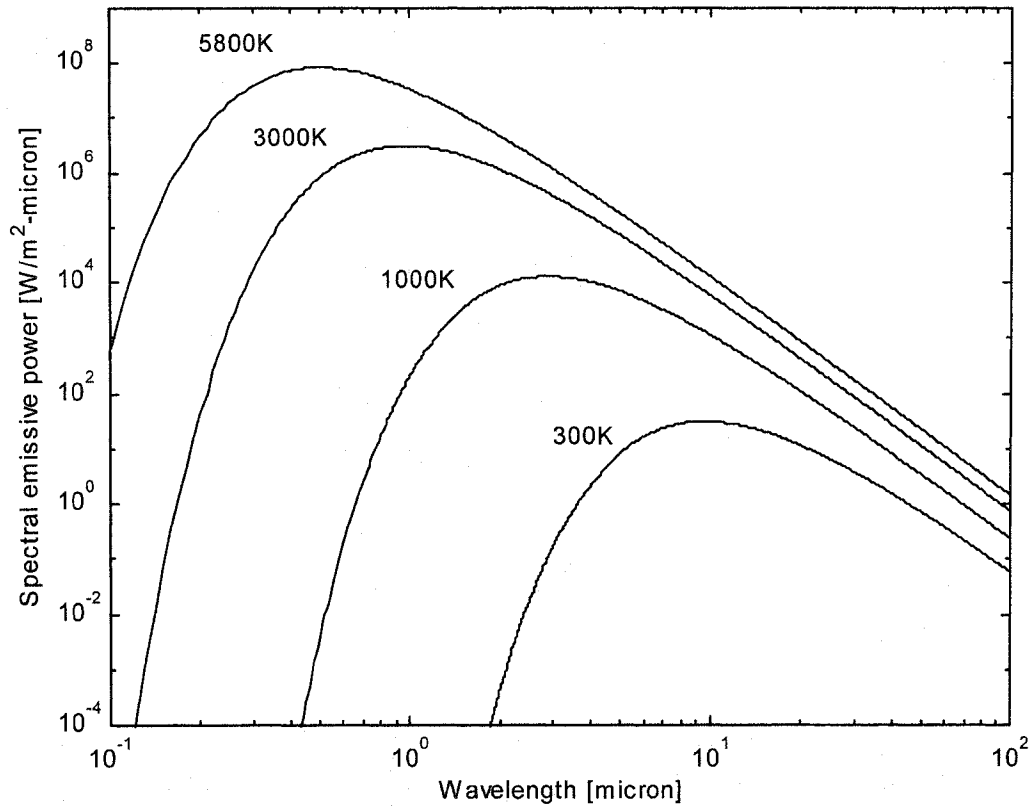


Figure 1.3 Spectral blackbody emissive power

## **1.4 Thesis overview**

The purpose of this project is to develop a high sensitivity CMOS optical micro-radiator vacuum sensor with extended pressure measurement range.

MEMS design packages are introduced in Chapter 2. Several different design packages, including MEMS PRO V2.0™, Mentor Graphics and Cadence, are compared as the design tools for the MEMS devices.

The CMOS optical micro-radiator is introduced in Chapter 3. The post-processing technique for fabricated chips is provided. A micro-radiator electro-thermal model is discussed to illustrate the heat transfers of the system.

Chapter 4 describes the experimental configuration, which includes a digital constant power supply unit used to apply constant power to the micro-radiator regardless of the resistance variation and a data acquisition unit used to measure and record the magnitude of the radiation from the micro-radiator. Sensitivity of the radiation measurement is calculated in this chapter by considering the response of the photodetector at different micro-radiator temperatures when approximating the micro-radiator as a blackbody.

Device characterization is discussed in Chapter 5. This includes a micro-radiator radiation analysis and reliability study of polysilicon, which provides threshold conditions for operating the micro-radiator as a reliable pressure sensor.

The radiation from the micro-radiator is calibrated versus pressure in the range from  $10^5$  Pa down to  $10^{-3}$  Pa in Chapter 6. A power-switching scheme used to increase the measurement sensitivity and lifetime of the device is also described. Automation of the measurement system with constant photodetector signal is introduced and realized in the chapter.

A three-mode CMOS photodetector design used for the integration of the system is introduced in Chapter 7. Fabricated photodetector design is calibrated at 670 nm in the power range from 0.01 mW to 10 mW.

Chapter 8 covers the numerical modeling of the device. Temperature distribution of the micro-radiator at 15 mW and photodetector output at different pressures at 10 mW is included. Simulation results are compared with experimental data.

Conclusions and future work are described in Chapter 9.

## References:

- [1] M. Gad-el-Hak (Editor), *The MEMS Handbook*, CRC Press, London, 2001.
- [2] D. E. Koshland, "Engineering a small world, from atomic manipulation to microfabrication", *Science*, vol. 254, 1991, pp. 1300-1342.
- [3] H. Kahn, M. de Boer, M. Judy, S. M. Spearing, "Materials Science of Microelectromechanical Systems (MEMS) Devices III", *MRS Symposium Proceedings*, vol. 657, Fall 2000.
- [4] Sid Marshall, "Kona Conference raises four issues about commercialization of MEMS", SUSS report, Karl Suss America, Inc., Waterbury Center, VT 05677, USA, vol. 10, third/fourth quarter 1996, p. 4.
- [5] M. Parameswaran, H. P. Baltes, Lj. Ristic, A. C. Dhaded and A. M. Robinson, "A new approach for the fabrication of micromechanical structures", *Sensors and Actuators*, 19, 1989, pp. 289-307.
- [6] C. M. Van Atta, *Vacuum Science and Engineering*, McGraw-Hill Book Company, New York, 1965.
- [7] J. F. O'Hanlon, *A User's Guide To Vacuum Technology*, 2<sup>nd</sup> Edition, John Wiley & Sons, Inc., New York, 1989.
- [8] C. H. Mastrangelo and R. S. Muller, "Microfabricated thermal absolute-pressure sensor with on-chip digital front-end processor", *IEEE J. Solid-State Circuits*, Vol. 26, 1991, pp. 1998-2007.
- [9] A. M. Robinson, P. Haswell, R. P. W. Lawson and M. Parameswaran, "A thermal conductivity microstructural pressure sensor fabricated in standard complementary metal-oxide semiconductor", *Rev. Sci. Instrum.*, Vol. 63, 1992, pp. 2026-2029.
- [10] P. K. Weng and J. S. Shie, "Micro-Pirani vacuum gauge", *Rev. Sci. Instrum.*, Vol. 65, 1994, pp. 492-499.

- [11] T. C. Kleckner, R. P. W. Lawson, and A. M. Robinson, "Constant power operation of incandescent micromachined polysilicon microresistors for use as vacuum pressure sensors", *J. Vac. Sci. Technol. A.*, Vol. 15(5), Sep/Oct 1997, pp. 2812-2815.
- [12] J. W. Gardner, *Microsensors – Principles and Applications*, John Wiley & Sons, Inc., New York, 1995, p. 117.
- [13] F. P. Incropera, D. P. DeWitt, *Introduction to Heat Transfer*, 3<sup>rd</sup> edition, John Wiley & Sons, Inc., New York, 1985, pp. 8-10.
- [14] M. Planck, *The Theory of Heat Radiation*, Dover Publications, New York, 1959.

## Chapter 2

### CMOS Micromachining and MEMS Design Packages

CMOS micromachining is a combination of the standard CMOS process and silicon micromachining technology. First, the standard CMOS process is used to build a MEMS structure with electric circuitry on a silicon substrate. An opening is created on the substrate by making all the films absent in that region. Afterwards, isotropic or anisotropic etching is used to release the MEMS structure. In this chapter, a typical CMOS micromachining fabrication process is described to illustrate the general procedure of fabricating CMOS micromachined devices.

Since micromachining fabrication technologies are borrowed from the microelectronics industry, IC design packages are naturally used for MEMS design. In recent years, some design packages focusing on MEMS designing, e.g. MEMS Pro from MEMSCAP<sup>®</sup> Inc. (headquarters: St. Ismier, France and Oakland, CA, USA), have been developed. In this chapter, MEMS design strategies along with the MEMS design packages available to Canadian universities through the Canadian Microelectronics Corporation (CMC) are briefly introduced and compared on the basis of the criteria such as working environment, ease of use, etch simulation and design rule checking.

#### ***2.1 A typical CMOS micromachining process***

Figure 2.1 shows a cross-section of a MEMS structure built with the Mitel 1.5  $\mu\text{m}$  process and with all the layers present.

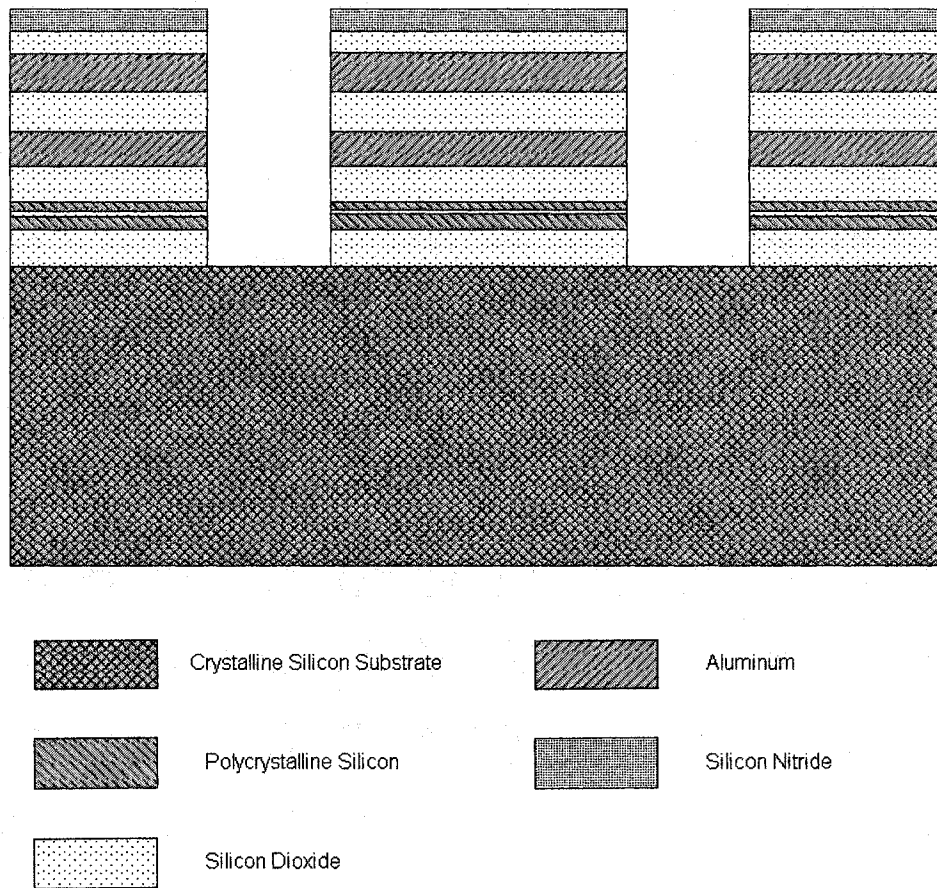


Figure 2.1 Cross-section of a wafer of a typical CMOS micromachining fabrication (not drawn to scale)

A typical Mitel 1.5  $\mu\text{m}$  CMOS micromachining fabrication process may include the following steps.

- Highly conductive n+ doped layers are diffused over the n-type silicon wafer.
- A 0.9  $\mu\text{m}$  field oxide layer may be used as a dielectric layer which electrically isolates the polysilicon structure from the crystalline substrate. It may also be used as structural material.
- After the field oxidation and gate oxidation (about 0.027  $\mu\text{m}$ , not shown in Figure 2.1), two layers of low-stress, doped polysilicon are then deposited (about 0.32  $\mu\text{m}$  and 0.25  $\mu\text{m}$  thick, respectively) with a 0.02  $\mu\text{m}$  oxide layer between. The polysilicon layers can also be used as electrically conductive layers.

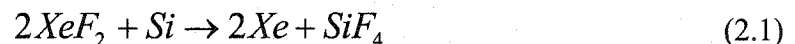


- Then a 0.8  $\mu\text{m}$  dielectric layer mainly composed of low-stress phosphosilicate glass (PSG) is deposited.
- Two 0.8  $\mu\text{m}$  patterned aluminum layers are then used to form conducting layers and electrical interconnects. There is a 1.0  $\mu\text{m}$  inter-dielectric oxide layer between two metal layers.
- Finally, two layers of passivation (0.5  $\mu\text{m}$  oxide and 0.5  $\mu\text{m}$  nitride) are deposited.

After the MEMS structures are fabricated, etching of the silicon substrate is used to release the structure from the substrate. There are two different types of etching: anisotropic and isotropic etching. Anisotropic etching is a process of preferential directional etching of material using liquid etchants like Ethylene Diamine Pyrocatechol (EDP) or Tetra Methyl Ammonium Hydroxide (TMAH). Isotropic etching refers to the etching of material regardless of crystallographic-orientation using an etchant such as Xenon difluoride.

Xenon difluoride has come into use as a replacement for anisotropic etchants EDP and TMAH recently [1-4] because of safety considerations. Xenon difluoride is a white solid at room temperature and pressure and sublimates at a pressure of about 500 Pa. Xenon difluoride vapor can etch silicon isotropically without external excitation and it has extremely high selectivity to many materials commonly used in MEMS.

The overall silicon/xenon difluoride reaction equation is given by:



The reaction is exothermic and the main product  $\text{SiF}_4$  is volatile at room temperature. It should be noted that moisture on the chip, which causes HF formation with exposure to  $\text{XeF}_2$  gas, is a safety hazard to operating personnel and can also result in silicon dioxide etching.

Figure 2.2 is a schematic picture showing the CMOS micromachined structure in Figure 2.1 isotropically released from the substrate. The actual shape of the etched cavity and the roughness of the etched surfaces depend on the amount of undercutting, the ease of circulation of  $\text{XeF}_2$ , etc.

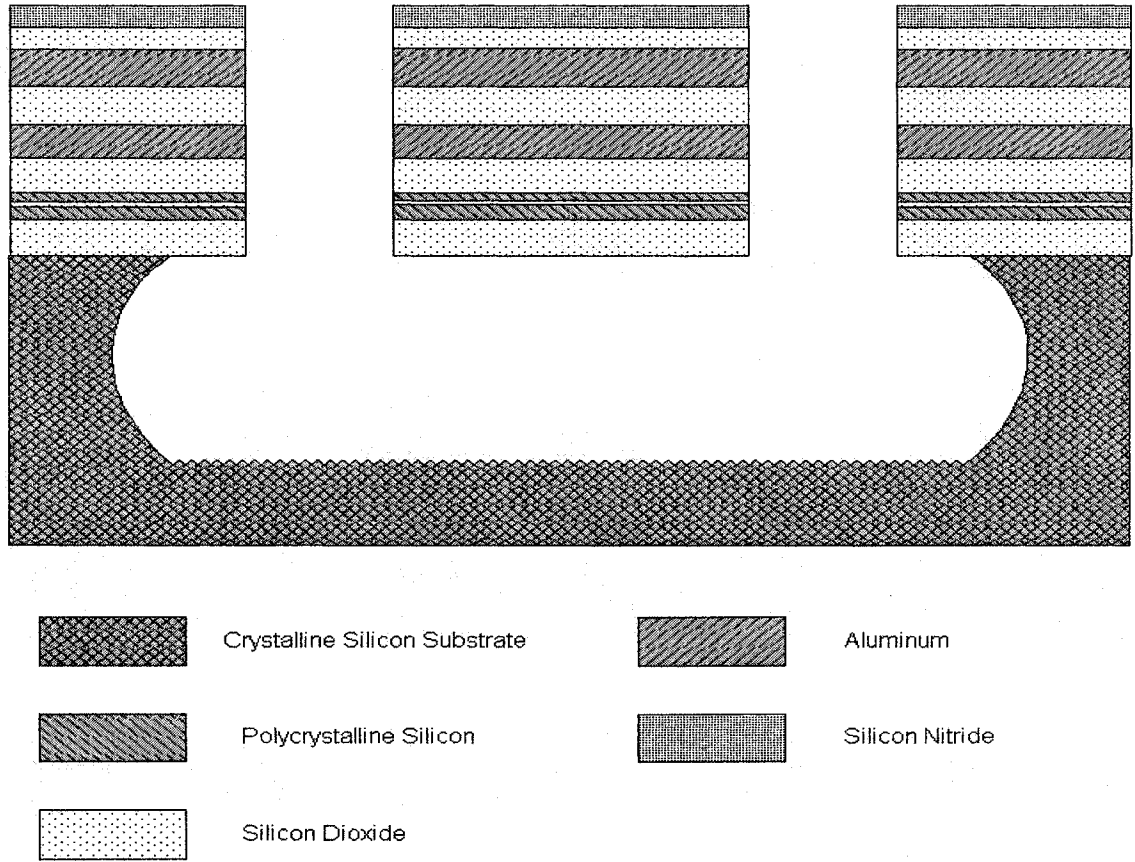


Figure 2.2 Cross-section of a typical MEMS structure released with  $\text{XeF}_2$

## 2.2 MEMS design packages

There are two different MEMS design strategies: the system approach and the device approach. The system approach starts from a schematic, which uses symbols or hardware description language (HDL) models to build the system. The schematic is then simulated and mask layout is generated for fabrication. The device approach starts directly from a mask layout, which is a scaled layer-by-layer drawing of the MEMS structures. Different colors are used to represent different layers of the structure. Finite element analysis (FEA) software, such as ANSYS, can be used to simulate the device by transferring the mask information directly into the FEA software to build the model for simulation.

There is an increasing interest in hardware description languages recently because of the rapid increase in circuit complexities, an industry-wide desire for more formal (correct-by-design) engineering methods, and a general maturing of low-cost, more accessible HDL tools [5]. HDL models convert mechanical systems to equivalent electrical models. However, the HDL models are limited to systems that are simple enough to be described by closed-form equations. All the design related to this project used the device approach.

There are three software packages currently used in the universities for IC and MEMS design: Cadence, Mentor Graphics and MEMS Pro. The advantages and disadvantages of each of the software packages are discussed below from the design experience of the author.

### **2.2.1 Mentor Graphics MEMS design kit**

A CMP<sup>®</sup> (Circuits Multi-Projects, Grenoble, France) / Mentor Graphics MEMS design-kit was used and evaluated for about one year under a contract with CMC [6].

The kit was installed on a Sun workstation running the Solaris operating system. Learning Mentor Graphics proved to be challenging, especially for new users who had no previous experience with Mentor Graphics and HDL modeling. The design kit provides a system design possibility using HDL simulation tools within the package. However, as mentioned above, it is only appropriate to MEMS structures simple enough to be described by a closed form equation, which then can be converted to its electrical “equivalent”.

The package also has a cross-sectional viewer and an etch simulator. The cross-sectional viewer provides the user with a feel for the three dimensional representation of the object under design. The etch simulator gives the user a view of the released device after etching. However, the etch simulator gives reasonable predictions for simple structures, but not for more complex structures like the Cantilever-In-Cantilever [7]. The design rule checker provided with Mentor Graphics MEMS design kit proved to be adequate.

In general, the package is satisfactory for designing MEMS devices. It is neither significantly better nor worse than other MEMS design packages.

### **2.2.2 Cadence IC layout editor and Multi-User MEMS Processes (MUMPs) design kit**

Cadence does not have a package for general MEMS design; the layout editor for IC design is used for mask design. Cadence uses the Solaris operating system. Design can only be implemented from the device approach.

The IC layout editor has many useful functions for object editing and learning to use it is relatively straightforward. It does not have any MEMS-related functionality like a cross-sectional viewer or etch simulator. However, Cadence has a Multi-User MEMS Processes (MUMPs) design kit available through CMC for surface micromachining design using the MUMPs technology of JDS Uniphase Inc. – MEMS Business Unit. The kit has a MUMPs device library, including some commonly used devices like comb drives, and electrostatic motors. Although the MUMPs technology is different to the CMOS technology, the design kit can be used for CMOS micromachining design by modifying its technology file. The design rule checker (DRC) of the kit needs improvement. Some parts of the layout with DRC violations turned out to be fine after fabrication; some parts without DRC violations did not work as expected afterwards.

In general, the layout editor of Cadence and the MUMPs design kit is satisfactory for MEMS and especially MUMPs design. The IC layout editor in Cadence is very convenient for mask design.

### **2.2.3 MEMSCAP® MEMS Pro**

MEMS Pro is a full suite of tools for MEMS and IC design and layout. The package includes schematic entry for IC design, IC circuit simulation and waveform viewing, layout editing, design rule checking and MEMS libraries.

MEMS Pro runs on a PC with Windows 95, Windows 98, or Windows NT 4.0. It needs a Pentium processor or better and 150 MB of disk space.

The layout editor, L-Edit, is originally from Tanner Research, Inc. and is very efficient and easy to use for mask designing. Figure 2.3 shows the design interface of L-Edit with a serpentine-shaped polysilicon resistor as an example. The interface screen can be divided into three parts: the tool palettes on the top of the screen; the layer palette on the left of the screen and the work area, where the polysilicon resistor layout is drawn.

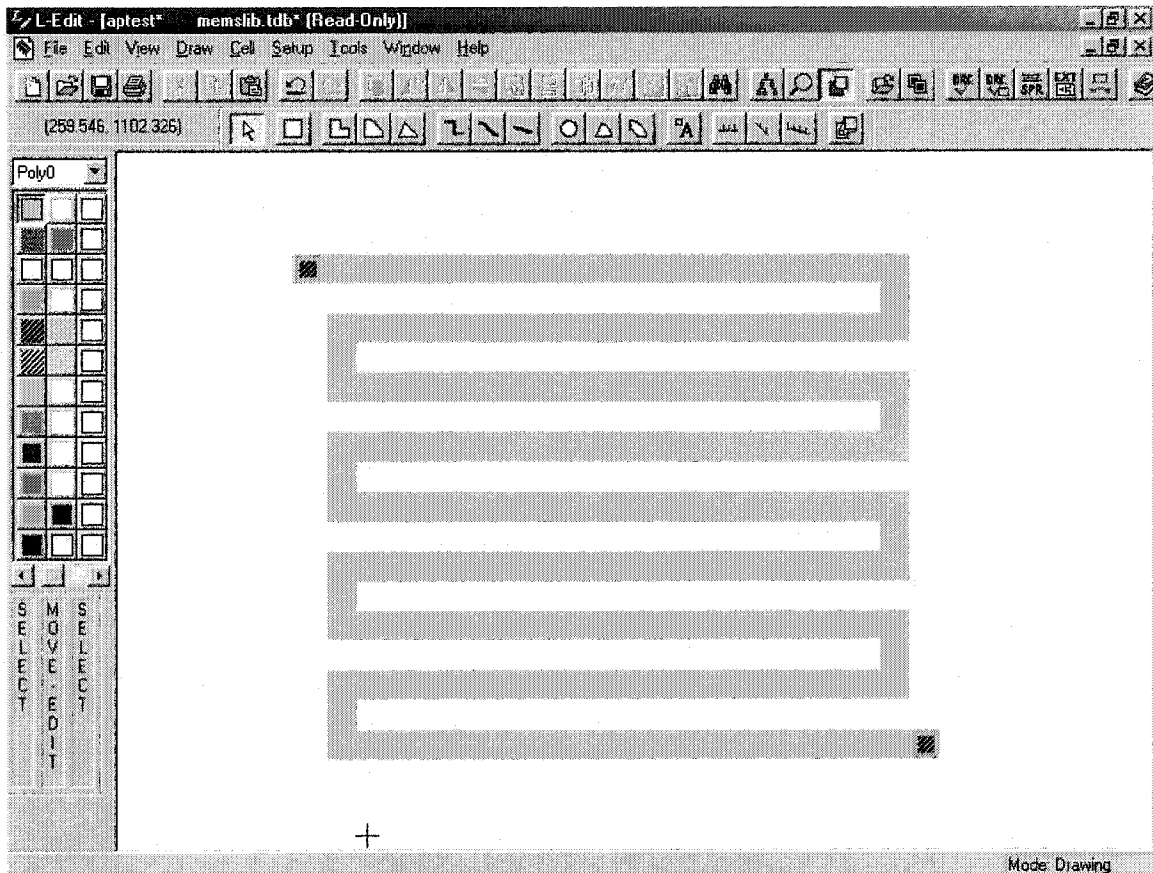


Figure 2.3 L-Edit user interface with a polysilicon resistor layout as an example

L-Edit provides standard shape selection, such as squares, circles and polygons. It also supports all-angle wire placement. The editing of shapes is easy with functionality such as stretch, rotate, flip and emerge. The design rule checker is also adequate.

Comparing the three packages introduced in this chapter, MEMS Pro has the advantage of ease of use and is amply equipped with the most features MEMS designer request. Its operating system is Windows. For designers with a preference for the Solaris operating system or designers with previous IC design experience, Cadence can be the best choice. It should be noted that both MEMS Pro and Cadence do not have an etch simulator by the time of writing this thesis. If the etching profile is critical to the design, a design package equipped with an etch simulator like the Mentor Graphics MEMS design kit will be necessary.

Both MEMS Pro and Cadence have been used in this project for the design and mask layout.

## References:

- [1] P. B. Chu, J. T. Chen, R. Yeh, G. Lin, J. C. Huang, B. A. Warneke, and K. S. J. Pister, "Controlled Pulse-Etching with Xenon Difluoride", *Ninth Int. Conf. Solid-State Sensors and Actuators (Transducers '97)*, Chicago, June 1997, pp. 665-668.
- [2] R. Toda, K. Minami, and M. Esashi, "Thin Beam Bulk Micromachining Based on RIE and Xenon Difluoride Silicon Etching", *Ninth Int. Conf. Solid-State Sensors and Actuators (Transducers '97)*, Chicago, June 1997, pp. 671-674.
- [3] F. I. Chang, R. Yeh, G. Lin, P. B. Chu, E. Hoffman, E. J. J. Kruglick, and K. S. J. Pister, "Gas-phase Silicon Micromachining with Xenon Difluoride", *Sym. on microelectronic structures and MEM devices for optical proc. and multimedia appl. (Proc. SPIE 2641)*, October 1995, pp. 117-128.
- [4] I. W. T. Chan, K. B. Brown, R. P. W. Lawson, A. M. Robinson, Y. Ma and D. Strembicke, "Gas Phase Pulse Etching of Silicon for MEMS with Xenon Difluoride", *IEEE Can. Conf. On Electrical and Computer Engineering*, Edmonton, May 1999, pp. 1637-1641.
- [5] D. Pellerin, D. Taylor, *VHDL Made Easy*, Prentice-Hall, Inc., London, 1997.

[6] Y. Ma and A. M. Robinson, "CMP/Mentor MEMS Design-kit Trial and Evaluation Report", Canadian Microelectronics Corporation, *Seminar on CMC's CAD support for MST*, Ottawa, January, 1998.

[7] B. Shen, CMOS Actuators, PhD Thesis, Department of Electrical Engineering, University of Alberta, Spring 1996.

## Chapter 3

### CMOS Optical Micro-Radiator

Incandescent filament light sources emit broadband radiation that extends from the visible wavelength to the infrared, which makes these sources very useful in optical signal generation. In recent years, miniature light sources have been fabricated utilizing micro-fabrication technologies [1-3]. In the sources described and used in these works, the filaments are electrically heated polycrystalline silicon bridges standing a few microns above a silicon substrate. The filaments are exposed to the atmosphere and thus are susceptible to rapid oxidation and contamination. In contrast to previous designs, our CMOS micromachined light source has a polycrystalline silicon filament embedded in layers of silicon dioxide and silicon nitride, which provides a degree of protection to these types of deterioration.

Design, post-processing and characterization of the CMOS optical micro-radiator are introduced in this chapter.

#### ***3.1 CMOS optical micro-radiator***

Figure 3.1 shows a Scanning Electron Microscope (SEM) picture of a fabricated micro-radiator. A layer of serpentine-shaped polysilicon is embedded in a silicon dioxide platform. The polysilicon is employed as a resistor. The serpentine shape is chosen to increase the amount of heat generated on the micro-radiator platform and thus radiation emitted. Radiation aspects will be discussed in Chapter 4. Two supporting arms are used instead of the more commonly used four-arm configurations [4] in order to minimize the



conduction heat loss through the arms. Because it is thermally isolated on its platform, modest currents are sufficient to heat the polysilicon to incandescence.

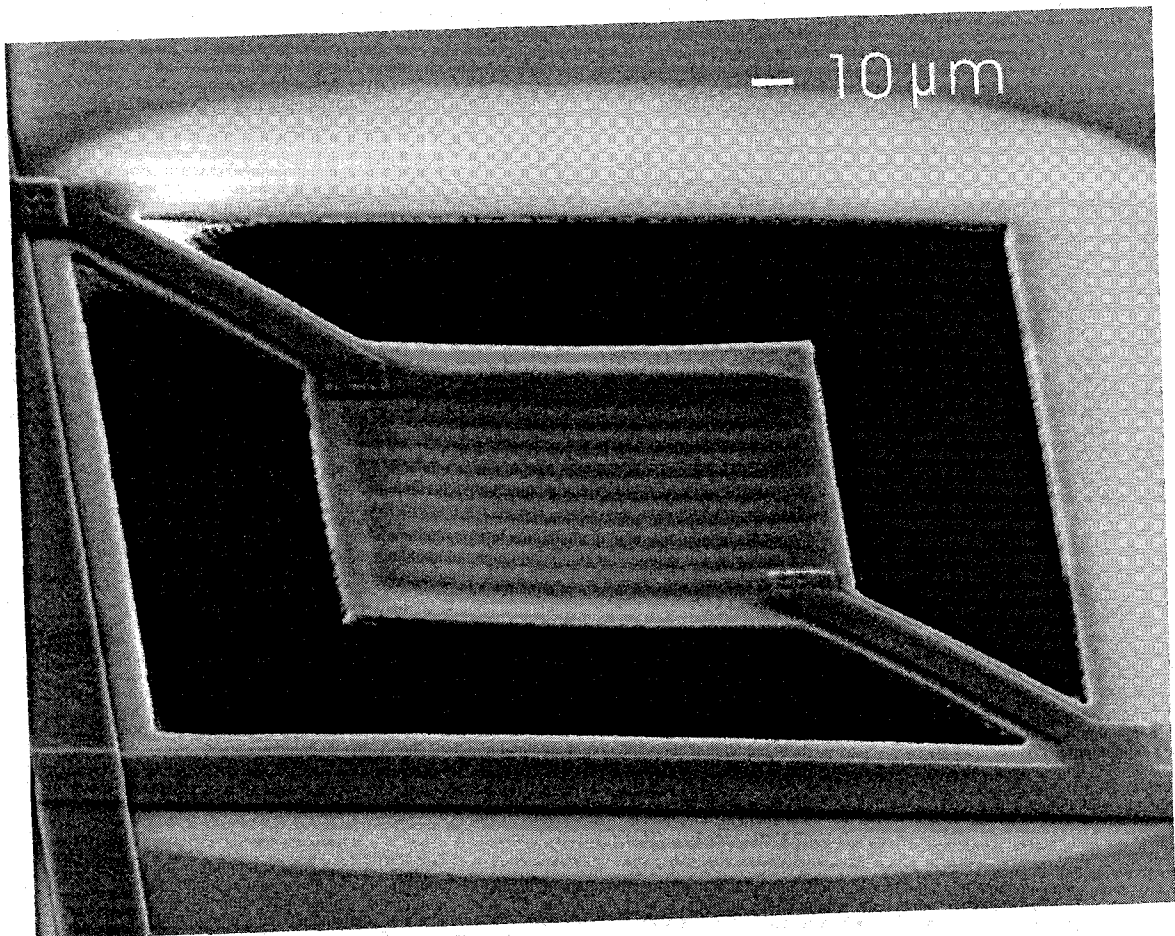


Figure 3.1 SEM picture of a serpentine-shaped polysilicon micro-radiator

The layout of the micro-radiator is shown in Figure 3.2 (A). The size of the platform is  $120\ \mu\text{m} \times 120\ \mu\text{m}$ . The width of the polysilicon is  $5\ \mu\text{m}$  and the total length is about  $940\ \mu\text{m}$ . Two arms suspend the platform and the length of each arm is  $85\ \mu\text{m}$ . Electrical power is supplied to the micro-radiator by the aluminum traces running through the arms. Polysilicon and aluminum are connected together in the regions called "contact".

A cross-sectional diagram of the micro-radiator platform along line CC' is shown in Figure 3.2 (B). The thickness of the platform is about  $3.5\ \mu\text{m}$ . At the bottom of the structure is a  $0.9\ \mu\text{m}$  field oxide layer, which is normally used to electrically isolate the polysilicon structure from the crystalline substrate. It is also widely used as structural material in MEMS. The field oxide layer may be etched a little during the fabrication and post-processing, which means a thickness smaller than  $0.9\ \mu\text{m}$  is possible. On top of the field oxide layer is a  $0.32\ \mu\text{m}$  layer of low-stress doped polysilicon. Then three layers of silicon dioxide are deposited to a total thickness of  $2.3\ \mu\text{m}$ . All thickness dimensions quoted here are specified by the CMOS manufacturer. The last layer deposited is a  $0.5\ \mu\text{m}$  layer of silicon nitride, which is used as a passivation layer in CMOS process. It has been suggested that the silicon nitride layer may be etched partly or totally during the etching process used to release the structure [5]. An follow-up experiment has been done to measure the etching rate of silicon nitride using  $\text{XeF}_2$  as etchant [6]. A layer of  $0.6\ \mu\text{m}$  silicon nitride was patterned with photoresist to protect some surface area and etched with  $\text{XeF}_2$  for 20 pulses. Then a profilometer was used to measure the thickness difference of the nitride layer between the protected and the etched areas. Experimental results indicated that the silicon nitride not protected was etched by  $\text{XeF}_2$ , but the thickness difference was very small and was not measurable by the profilometer.

A different configuration with polysilicon supporting arms instead of aluminum has also been designed. Heat loss through the arms decreases with this kind of configuration because of the smaller thermal conductivity of the polysilicon material compared with Al. Also, Ohmic heating of the polysilicon in the arms will tend to reduce the temperature gradient between the platform and the base of the arms at the substrate. Some experimental results obtained with this configuration are also presented in the following chapters.

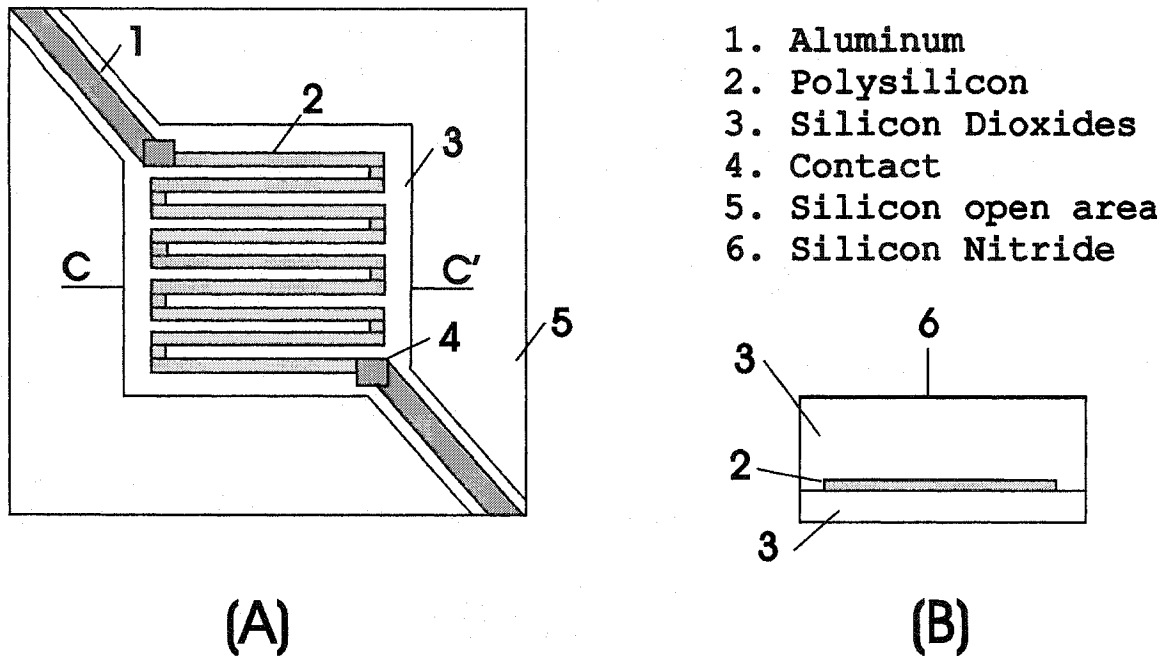


Figure 3.2 Micro-radiator layout (A) and cross-sectional diagram (B)

The micro-radiator is released by  $\text{XeF}_2$ . The  $\text{XeF}_2$  etching system used to release the micro-radiators can be found in reference [7]. The etched pit as shown in Figure 3.1 is  $85 \mu\text{m}$  in depth and the undercutting of the oxide layer due to the isotropic etching of silicon is about  $50 \mu\text{m}$  on each side. The undercut is seen as the lighter colored regions extending from the edge of the square opening in the oxide layers in Figure 3.1.

### 3.2 Micro-radiator electro-thermal model

When electrical power  $W$  is supplied to the micro-radiator, it heats up. Because the micro-radiator platform is released and the presence of the air underneath the structure provides good thermal isolation, the temperature of the micro-radiator can be raised easily to several hundred degrees above the substrate temperature with a modest input power.

Three heat dissipation mechanisms occur for the power applied to the micro-radiator: conduction, convection and radiation. Figure 3.3 is a schematic representation showing the heat transfers related to the micro-radiator.

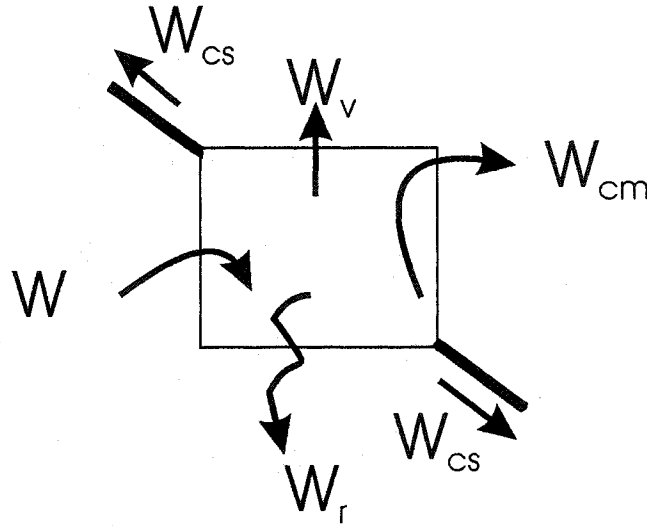


Figure 3.3 Heat transfers related to the micro-radiator

The micro-radiator temperature depends upon: (1) Rate of supply of electrical energy  $W$ ; (2) Conduction heat loss through the gas  $W_{cm}$ , conduction heat losses from the micro-radiator platform via the support arms  $W_{cs}$ ; (3) Convection heat loss  $W_v$ ; (4) Radiation heat loss  $W_r$ .

Considering a simplified micro-radiator of width  $x$ , length  $y$ , and thickness  $z$ , suspended from the substrate by a distance  $s$ , as shown in Figure 3.4, the heat balance equation is given by

$$W - \dot{Q} = W - W_{cm} - W_{cs} - W_v - W_r = \rho cxyz \frac{\partial T}{\partial t} \quad (3.2.1)$$

in which,  $\dot{Q}$  is the total heat loss from the platform,  $\rho$  is the mass density of the micro-radiator material,  $c$  is the specific heat and  $T$  is the average temperature of the micro-radiator.

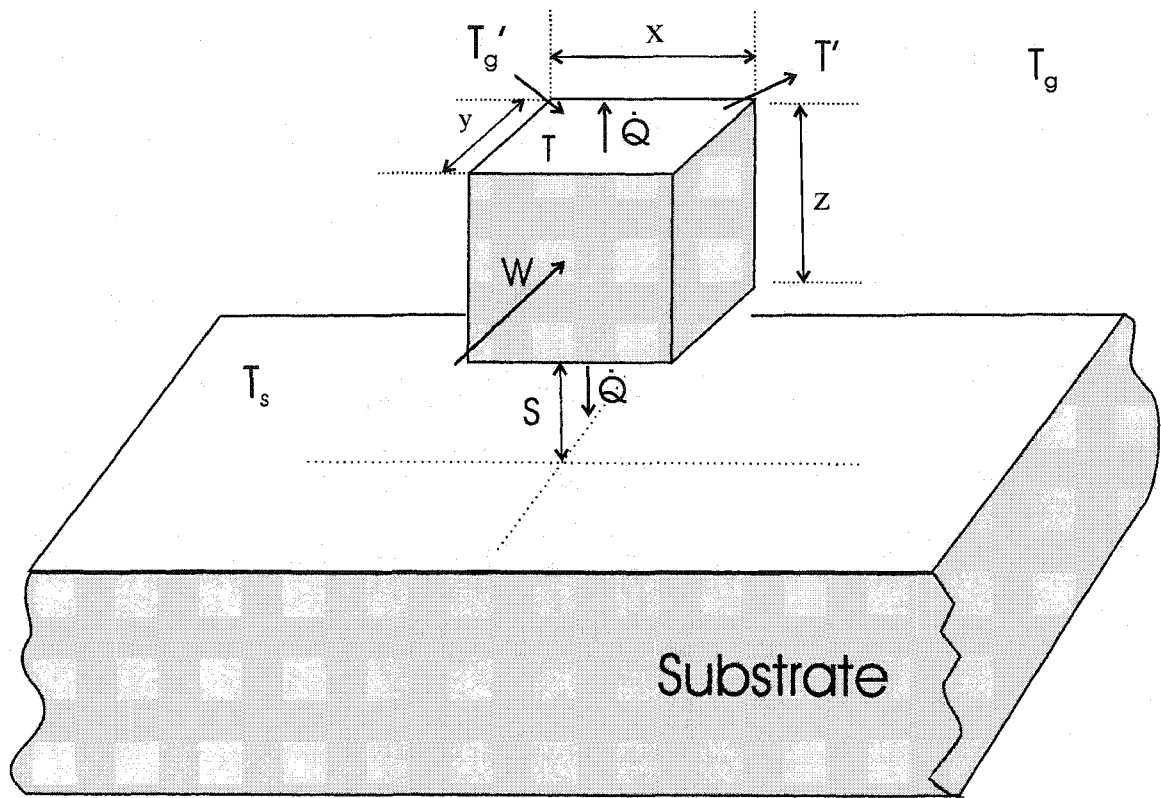


Figure 3.4 A simplified micro-radiator structure

### 3.2.1 Conduction heat loss through the gas and through the supports

The actual physical process of conduction heat loss through the free molecules of surrounding gas is very complex. If the gas molecules have average temperatures of  $T_g'$  and  $T'$  on arrival to, and departure from, the micro-radiator, respectively, as shown in Figure 3.4, the rate of energy transfer  $W_{cm}$  from the micro-radiator to the gas and to the substrate, is given by

$$W_{cm} = k_1 n (T' - T_g') = Kxy(T' - T_g')p \quad (3.2.2)$$

where  $k_1, K$  are related constants,  $n$  is the number of molecules striking the micro-radiator per second,  $xy$  indicates the surface area of the micro-radiator as shown in Figure 3.4, and  $p$  is the gas pressure.  $W_{cm}$  is directly proportional to the pressure at any given gas temperature. Knudsen defined a constant  $\alpha$ , called the accommodation coefficient, as [8]

$$\alpha = \frac{T' - T_g'}{T - T_g'} \quad (3.2.3)$$

where  $T, T_g'$  and  $T'$  are the temperatures of micro-radiator surface, the incident and the reflected molecules, respectively. Introducing this constant into equation (3.2.2) gives

$$W_{cm} = \alpha K xy (T - T_g') p \quad (3.2.4)$$

$K$  can be calculated from [9,10,11]

$$K = \frac{1}{4} \frac{\gamma + 1}{\gamma - 1} \sqrt{\frac{2k_0}{\pi m T_g}} \times 10^{-2} \quad (3.2.5)$$

where  $\gamma = C_p/C_v$  is the ratio of the specific heats of the gas,  $k_0$  is the Boltzmann constant,  $m$  is the mass of the gas molecule, and  $T_g$  the average temperature of the gas far from the micro-radiator. For air,  $\gamma = 7/5$ ;  $m = 28.98$  AMU.

$T_g'$ , the only unknown in equation (3.2.4), depends upon the gas mean free path  $\lambda_{mfp}$  and therefore upon the pressure. We assume the micro-radiator, with a platform dimension  $x$  by  $y$ , is placed in a chamber with diameter  $D$  and the distance from the bottom of the micro-radiator to the substrate,  $s$ , is always smaller than  $d$ , the larger one of  $x$  and  $y$ . There are four distinct conditions to consider in estimating  $T_g'$ , (a) when  $\lambda_{mfp} > D$ , (b) when  $d < \lambda_{mfp} < D$ , (c) when  $s < \lambda_{mfp} < d$ , and (d) when  $\lambda_{mfp} < s$ . For (a), when  $\lambda_{mfp} > D$ , each molecule above the micro-radiator makes many collisions with the outer walls of the chamber and below the micro-radiator makes many collisions with the substrate and so is always in temperature equilibrium with the chamber wall and the substrate on striking the micro-radiator, making  $T_g' = T_g$  or  $T_g' = T_s$ , the substrate

temperature as shown in Figure 3.4. For (b), when  $d < \lambda_{mfp} < D$ , the molecules, although they may not reach the chamber wall, have many collisions with other molecules above the micro-radiator and have many collisions with the substrate below the micro-radiator between each collision with the micro-radiator. Therefore,  $T_g' = T_s$  or  $T_g' \approx T_g$ . For (c), when  $s < \lambda_{mfp} < d$ , some molecules return to the micro-radiator before reaching equilibrium with the main body of the gas or the substrate, some reach the equilibrium with the substrate.  $T_g'$  is then very difficult to estimate because of the temperature gradient through the gas and the unknown percentage of collision with the substrate. For (d), when  $\lambda_{mfp} < s$ , most molecules return to the micro-radiator before reaching equilibrium with the main body of the gas and thus  $T_g' > T_g$ . The difference increases with increasing pressure.

A first order approximation that only considers the heat flow to the substrate at the base of the etched cavity may be calculated by

$$W_{cm} = \eta \alpha K x y \frac{(T - T_s)}{s} p \quad (3.2.6)$$

where  $K$  is the constant calculated in (3.2.5);  $\alpha$  the accommodation coefficient;  $s$  the distance from the micro-radiator to the substrate. The factor  $\eta$  denotes the coefficient accounting for the first order approximation.

The equation for the heat conduction from the platform to the substrate via each support arm is averaged out along the whole arm for simplicity:

$$W_{cs} = n_s k_s A_s (T - T_s) / e \quad (3.2.7)$$

The factor  $n_s$  denotes the number of supporting arms,  $k_s$  is the thermal conductivity of the support arm material,  $A_s$  the cross-section area of the arm and  $e$  is the length of the arm.

### 3.2.2 Convection heat loss

Heat transition in a free convection boundary layer depends on the relative magnitude of the buoyancy and viscous forces in the gas. When natural convection occurs, all the convected heat is carried by the gas floating upward and eventually is carried away by the gas far above the device. The convection heat loss  $W_v$  is assumed to obey Newton's cooling law [12]

$$W_v = 2h(v, p)xy(T - T_g) \quad (3.2.8)$$

where  $h(v, p)$  is the convective heat-transfer coefficient from the micro-radiator platform to the gas as a function of gas flow velocity  $v$  and absolute pressure  $p$ .  $T_g$  is the temperature of the gas very far from the substrate.

It is customary to correlate the occurrence of natural convection in terms of the Rayleigh number,  $Ra$ . This number, characterizing the strength of the heat flow driving the turbulence, is defined as the product of the Prandtl and Grashof numbers  $Pr$  and  $Gr$  [13]:

$$\begin{aligned} Ra &= Gr \times Pr \\ &= \left( \frac{g\beta\rho^2 d_c^3 \Delta T}{\mu^2} \right) \left( \frac{\mu c_p}{k} \right) \\ &= \frac{g\beta d_c^3 \Delta T}{\nu \chi} \end{aligned} \quad (3.2.9)$$

where  $g$  is the acceleration due to gravity,  $\beta$  is the coefficient of thermal expansion of the air,  $\rho$  is the density of air,  $d_c$  the critical dimension of the structure defined as the ratio of the structure surface area to its perimeter,  $\mu$  is the dynamic viscosity of air,  $C_p$  its specific heat at constant pressure,  $k$  its thermal conductivity, and  $\chi$  its thermal diffusivity. The kinematic viscosity of air,  $\nu$ , is a coefficient defined as the ratio of the dynamic viscosity of air  $\mu$  to its density  $\rho$ . The relationship between thermal conductivity  $k$  and thermal diffusivity  $\chi$  is given by  $k = \rho c_p \chi$ .



The Grashof number  $Gr$  is a measure of the ratio between buoyancy forces and viscous forces. The Prandtl number  $Pr$  measures the relative propensities of the fluid to diffuse momentum and heat.

In the case of our micro-radiator,  $Gr \cong 7 \times 10^{-4}$  at atmospheric pressure and is even smaller at lower pressure, indicating that the buoyancy forces are minute compared with the viscous forces. The Prandtl number  $Pr$  is about 0.7 for air, so the Rayleigh number is about  $5 \times 10^{-4}$ . Usually the Rayleigh number needs to exceed 600 for convection to occur. The smallest Rayleigh number published is about 0.1 [13]. Therefore, it is reasonable to assume that natural convection contributes virtually nothing to the cooling of the micro-radiator. Experimental results also proved the response of the micro-radiator to be independent of device orientation [14], which means the convection heat loss is negligible compared to other types of heat losses.

### 3.2.3 Radiation heat loss

The radiation heat losses can be approximated by

$$W_r = \varepsilon \sigma xy (T^4 - T_g^4) + \varepsilon \sigma xy (T^4 - T_s^4) \quad (3.2.10)$$

where  $\varepsilon$  is the emissivity of the micro-radiator material and  $\sigma$  is the Stefan-Boltzmann constant.  $T_g$ , as mentioned above, is the temperature of the gas and  $T_s$  is the temperature of the substrate. Here we assume that the upper face of the platform radiates to the gas while the bottom face radiates to the substrate. Radiation from the side faces of the platform is assumed small and is neglected here.

### 3.2.4 Total heat loss

If we assume  $T_g \approx T_s$ ,  $W_{cm}$ ,  $W_{cs}$  and  $W_r$  can be written as

$$W_{cm} = K_{CM} \alpha (T - T_g) p \quad (3.2.11)$$

$$W_{cs} = K_{CS}(T - T_g) \quad (3.2.12)$$

$$W_r = K_R(T^4 - T_g^4) \quad (3.2.13)$$

where  $K$  is defined as equation (3.2.5),  $K_{CM}$ ,  $K_{CS}$  and  $K_R$  are equal to

$$K_{CM} = \eta K_{xy} / s \quad (3.2.14)$$

$$K_{CS} = n_s k_s A_s / e \quad (3.2.15)$$

$$K_R = 2\epsilon\alpha xy \quad (3.2.16)$$

Therefore the heat balance equation of the micro-radiator can be written as:

$$W - K_{CM}\alpha(T - T_g)p - K_R(T^4 - T_g^4) - K_{CS}(T - T_g) = \rho cxyz \frac{\partial T}{\partial t} \quad (3.2.17)$$

It is very difficult to analytically solve the heat balance equation, equation (3.2.17), with each term included. A simple calculation that ignores the convection and radiation heat losses, has been done in reference [15]. The calculation shows the average temperature rise yields an exponential time variation

$$\Delta \bar{T}(t) \propto (1 - e^{-(t/\tau)}) \quad (3.2.18)$$

with a time constant  $\tau$  that depends on the surrounding gas pressure. A measurement of the time constant shows  $\tau$  is about 30 ms at  $10^{-4}$  Torr and about 15 ms at one atmosphere [14].

An analytical solution for the average temperature of micro-radiator,  $T$ , is difficult to get from equation (3.2.17), but the relationship between  $T$  and the surrounding gas pressure  $p$ , can be plotted by solving  $p$  from equation (3.2.17) at equilibrium:

$$p = (W - K_R(T^4 - T_g^4) - K_{CS}(T - T_g)) / K_{CM}\alpha(T - T_g) \quad (3.2.19)$$

Figure 3.5 shows a curve of micro-radiator average temperature versus the surrounding gas pressure at equilibrium with an input power of 10 mW and a room temperature of 293 K. The curve was plotted using Matlab and the source code can be found in Appendix A. A series of temperatures from 273 K to 2000 K was used to calculate the corresponding equilibrium pressure using equation (3.2.19) and the results were plotted by temperature as a function of pressure. Please refer to Appendix A for details.

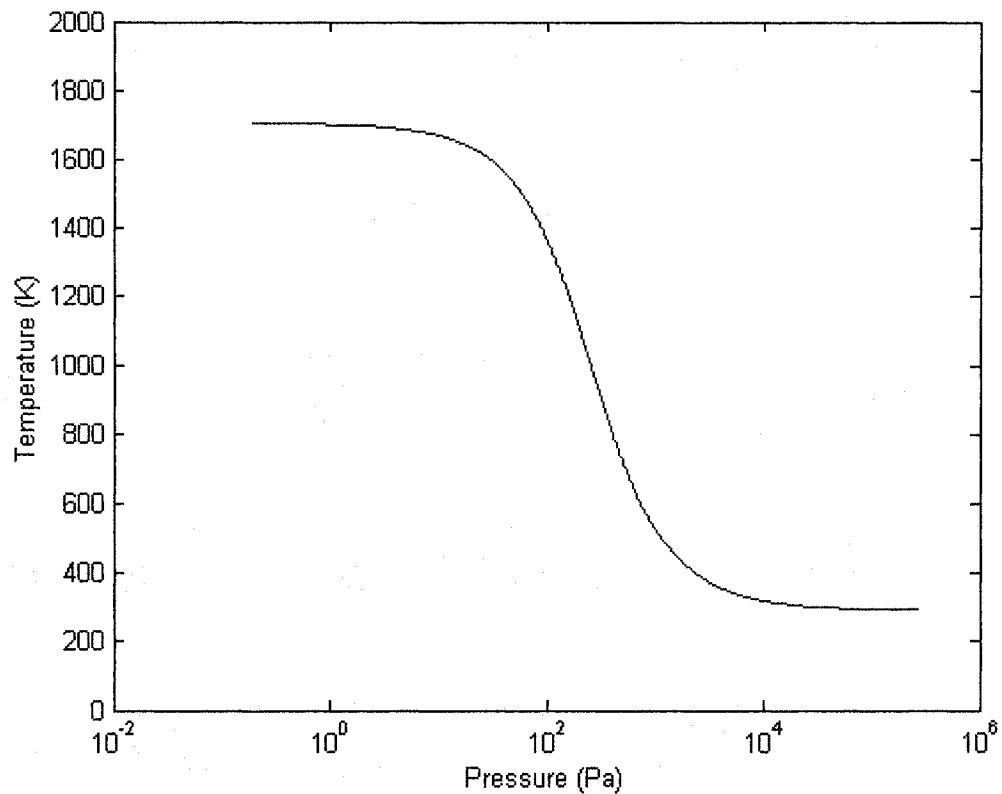


Figure 3.5 Average temperature of the micro-radiator versus the surrounding gas pressure operating at a power of 10 mW

Figure 3.5 demonstrates the typical shape for a thermal conductivity pressure gauge. In the middle part of the curve (pressure range from  $10^1$  Pa to  $10^3$  Pa), the gas conduction heat loss tends to dominate and the temperature of the micro-radiator is a strong function of the gas pressure. At high pressure, the thermal conductivity of the gas is independent of the pressure and therefore the temperature of the structure is almost constant as a

function of pressure. At low pressure, the conduction heat loss through air becomes significantly smaller than the radiation and the conduction through the arms and the temperature becomes again independent of the pressure. The temperature simulated by the Matlab program in Figure 3.5 is lower than the temperature derived from measured resistance at high pressure and higher than the temperature derived at low pressure. The difference between the experimental data and the simulation results is due to the assumptions made in the theoretical model and considered acceptable in this project.

### 3.2.5 Thermal conductivity gauge useful range

Figure 3.6 shows temperature variations of a micro-radiator under two different power inputs  $W_1$  and  $W_2$ , with  $W_1 < W_2$ . Temperature variations between points  $A$  and  $B$  on curve  $W_1$  and  $A'$ ,  $B'$  on curve  $W_2$  vary sharply with pressure and are regarded as the sensitive and useful ranges of the gauge.

The lowest useful pressures indicated as point  $A$  and  $A'$  are determined when the radiation  $W_r$  and conduction heat loss through the supports of the device  $W_{cs}$  equal the conduction through the gas  $W_{cm}$ . The upper pressure limit indicated by point  $B$  and  $B'$  are determined when the mean free path becomes comparable to the dimension of the micro-radiator and the distance between the micro-radiator to the substrate (Knudsen number  $Kn \approx 1$ ), so that molecules departing from the radiator lose their thermal energy within a short distance. This forms a hot sheath of gas that inhibits further heat transport.

For the input powers of  $W_1$  and  $W_2$ , the average temperature of micro-radiator at a certain pressure is higher with power  $W_2$  than the temperature obtained with power  $W_1$ . Thus the radiation heat loss and conduction heat loss through the supports are higher and the conduction heat loss through the gas  $W_{cm}$  becomes comparable to  $W_r$  and  $W_{cs}$  (points  $A$  and  $A'$ ) at a higher pressure. The lowest useful pressure limit  $A$  on curve  $W_1$  moves to a higher pressure point  $A'$  on curve  $W_2$  as indicated in Figure 3.6.

The micro-radiator operating at power  $W_2$  also heats up the surrounding air to a higher temperature than the one at power  $W_1$ . The mean free path of the surrounding gas

under  $W_2$  is therefore larger at a certain pressure because  $\lambda_{mfp} \propto \frac{T}{p}$ . The upper pressure limit  $B$  moves to a higher pressure  $B'$ , where the mean free path becomes comparable to the characteristic dimension of the system again.

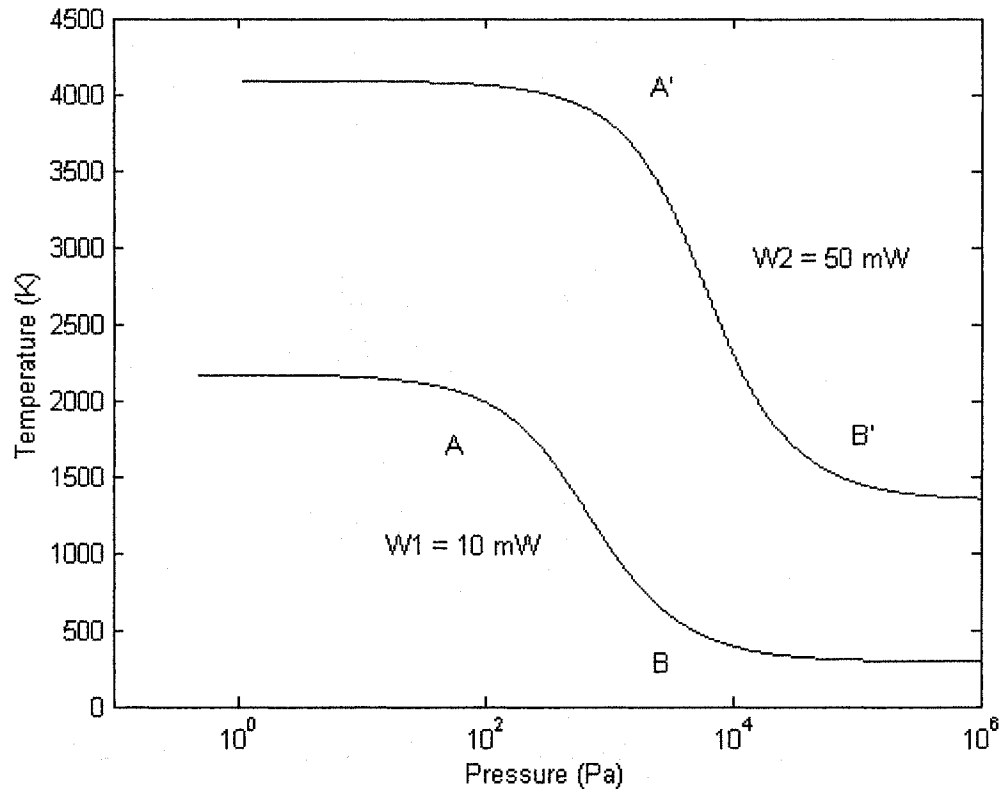


Figure 3.6 Temperature variation of a typical thermal-conductivity gauge operating at constant power inputs of 10 and 50 mW

Comparing the temperature variation curves under power  $W_1$  and  $W_2$  in Figure 3.6, we can see the sensitive pressure range shifts to the right when the input power increases. In the next chapter, we will see the spectral emission of the micro-radiator not only increasing in absolute magnitude, but also shifting more into the response region of the photodetector when the input power increases. This enables the sensitivity and pressure range of the gauge to be varied by manipulating the input power to the micro-radiator.

## References:

- [1] M. Tuma, K. King, L. Kim, R. Hansler, E. Jones and T. George, "MEMS incandescent light source", SPIE Proceeding, vol. 4139, August 2000.
- [2] G. Lamb, M. Jhabvala, and A. Burgess, "Integrated-circuit broadband infrared sources", *NASA Tech. Briefs*, March 1989, p. 32.
- [3] R. T. Howe and R. S. Muller, "Polycrystalline silicon micromechanical beams", Extended Abstract, Electrochemical Society Meeting, , Montreal, Canada, May 9-14, 1982, pp. 186-189.
- [4] M. Parameswaran, A. M. Robinson, D. L. Blackburn, M. Gaitan and J. Geist, "Micromachined Thermal Radiation Emitter from a Commercial CMOS Process", *IEEE Electron Device Letters*, Vol. 12, no. 2, 1991, pp. 57-59.
- [5] Sandra Esteves, "CMOS Micromachined Devices for Applications in Fluids", M.Sc. Thesis, Department of Electrical and Computer Engineering, University of Alberta, 2000.
- [6] Private communication, Dr. A. M. Robinson, University of Alberta; M. Hu / D. Lu 's report, unpublished, February 2001.
- [7] I. W. T. Chan, K. B. Brown, R. P. W. Lawson, A. M. Robinson, Y. Ma and D. Strembicke, "Gas Phase Pulse Etching of Silicon for MEMS with Xenon Difluoride", *IEEE Can. Conf. Electrical and Computer Engineering*, Edmonton, May 1999, pp. 1637-1641.
- [8] M. Knudsen, *Ann. Phys., Lpz.*, vol. 34, 1911, p. 593.
- [9] J. M. Lafferty, *Fundations of Vacuum Science and Technology*, John Wiley & Sons, Inc., New York, 1998, p. 406.
- [10] A. Bejan, *Convection Heat Transfer*, Wiley-Interscience, New York, 1984.
- [11] H. Von Ubisch, "On the Conduction of Heat in Rarefied Gases and Its Manometric Application", *Appl. Sci. Res.*, Vol. A2, 1951, pp. 364-430.
- [12] C. H. Mastrangelo, *Thermal Applications of Microbridges*, Ph.D. Thesis, University of California, Berkeley, 1991, p.14.
- [13] Private communication, J. Jones, *Cooling of a Circuit Element*, Simon Fraser University, School of Engineering Science Memo, June 5<sup>th</sup>, 1990.

[14] B. Shen, Z. Lai, A. M. Robinson and W. Allegretto, "Thermal response of CMOS-micromachined thermistor sensors under constant power and constant current excitation", *Rev. Sci. Instrum.* 65 (11), November 1994, pp. 3528-3534.

[15] B. Shen, CMOS Actuators, PhD Thesis, Department of Electrical Engineering, University of Alberta, Spring 1996.

## Chapter 4

### Experiment Configuration and Measurement Sensitivity

Figure 4.1 shows the experimental configuration in a diffusion-pumped bell jar working chamber. A 3 mm by 3 mm silicon loose die with a linear array of micro-radiators is mounted in a Dual In-line Package (DIP) with silver paint. Manual wire bonding was performed to provide electrical connection to the micro-radiators. The DIP is then put into the vacuum chamber with wires directly wrapped around the pins as shown in Figure 4.1. For testing in air, the DIP is put into a Zero Insertion Force (ZIF) socket which provides electrical connections from the DIP pins to the Experiment Control System. The zero insertion pressure feature of the socket allows easy insertion and removal without pin distortion. The radiation from the micro-radiator is measured by a photodetector. The experiment Control System consists of two parts: a digital constant power supply unit, which supplies constant power to the micro-radiator, and a data acquisition unit, which measures the output of the photodetector. Details of each part of the configuration will be given in the following sections.

#### **4.1 Variable pressure chamber**

The variable pressure chamber is a glass bell jar vacuum chamber. A diffusion pump along with a mechanical rotary pump controls the pressure of the system.

The chamber is first pumped down to  $10^{-2}$  Torr by the rotary pump, then down to  $10^{-5}$  Torr by the diffusion pump. The pumps are then isolated from the chamber and air is slowly bled into the bell jar. The controlled inflow rate is low enough to avoid forced convective cooling of the device.



Four pressure gauges measure the pressure of the chamber: Two Wallace & Tiernan diaphragm manometers (20 – 700 torr, 0.5 – 20 torr), a Pirani gauge (0.01 – 0.5 torr), and a Bayard-Alpert ionization gauge ( $10^{-5}$  – 0.01 torr).

The micro-radiator is mounted in the chamber with the photodetector directly above. The distance between the micro-radiator and the photodetector is about 2.5 cm. Six feed-through connectors connect the micro-radiator and photodetector within the chamber to the outside equipment.

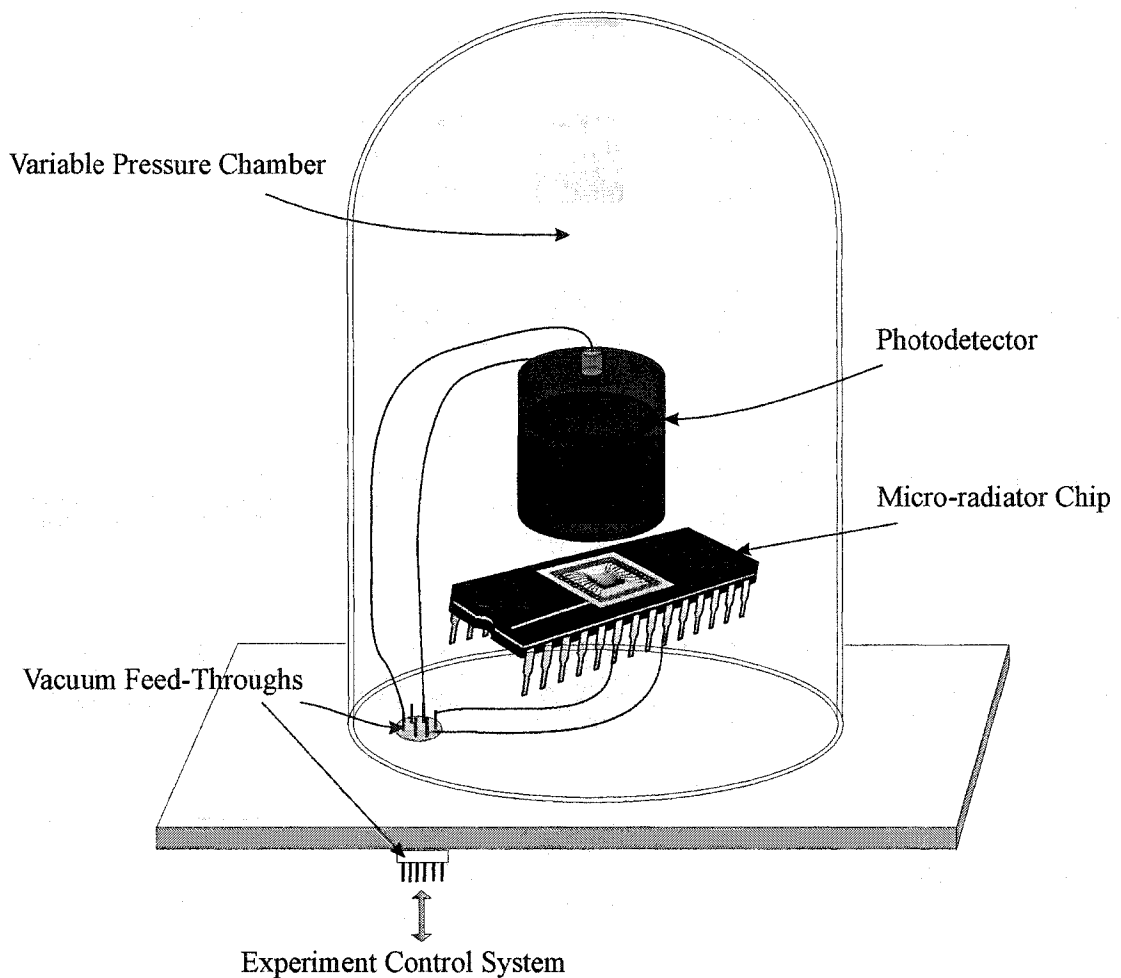


Figure 4.1 Experiment setup

## 4.2 Photodetector and point source of light

The photodetector used in the experiment is a silicon photodetector fabricated by Melles Griot, model: 13DAS 011/C, with an active area of  $100 \text{ mm}^2$ . Response from 400 nm to 1100 nm at 10 nm intervals of the photodetector provided by the manufacturer is shown in Figure 4.2. Responsivity of the photodetector is defined as the ratio of the output current (in Amperes) from the detector to the intensity of incident light (in Watts). From Figure 4.2, we can see the photodetector is most sensitive at 985 nm. Response data below 400 nm and above 1100 nm are not available.

The photodetector signal is amplified by a large dynamic amplifier fabricated by Melles Griot (model 13 AMP 003) and can be directly read into the computer by an Hewlett Packard Instrument Basic interface card. The measured dark current of the photodetector is about 0.008 nA.

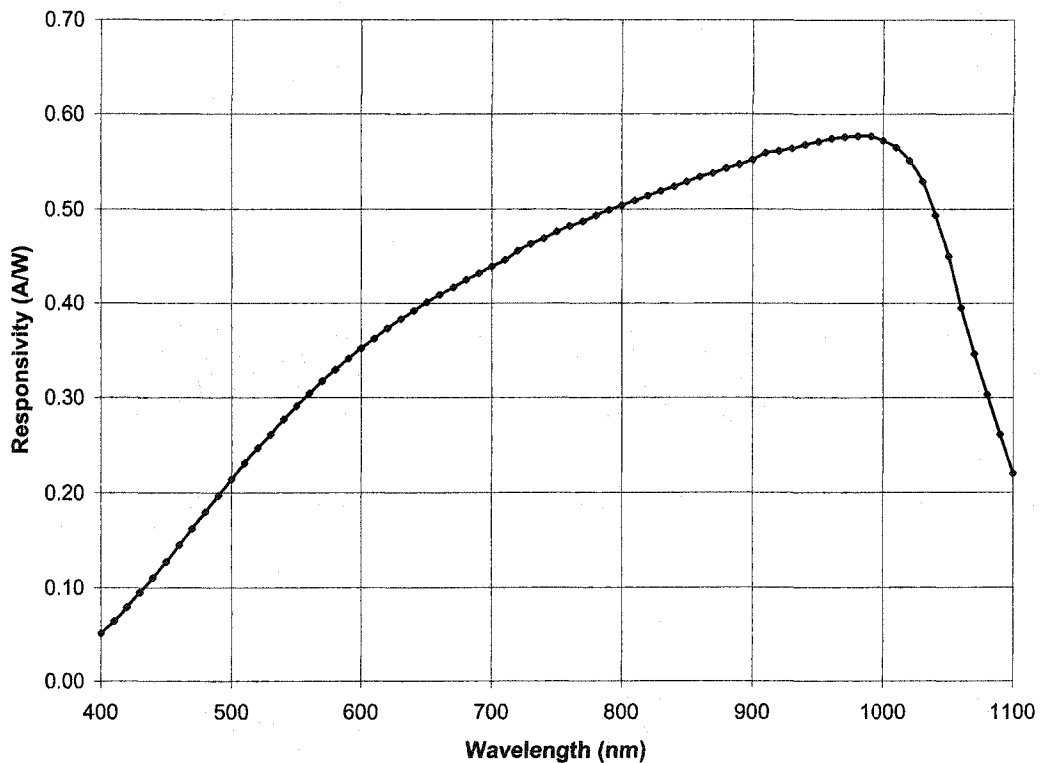


Figure 4.2 Response data for silicon photodiode 13 DAS 011/C

The relationship between the photodetector response and the intensity of light incident upon it was measured using a light bulb as a point source and varying the distance of the light source from the photodetector.

As we know, light is electromagnetic waves. The wavefronts of a point source of light are spherical surfaces and light intensity  $J$  represents the amount of energy per unit time per unit area transported across any surface oriented normally to the propagation direction. The total rate of flow of electromagnetic energy  $dU/dt$  across any such spherical surface of radius  $r$  may be obtained by integrating the intensity over the area of the spherical surface as shown in Figure 4.3:

$$\frac{dU}{dt} = \oint J da = 4\pi r^2 J \quad (4.2.1)$$

Since the total rate of flow of energy across any spherical surface is the same, for two surfaces of radii  $r$  and  $r'$  at which the intensity has the values of  $J$  and  $J'$ , we have

$$\frac{J}{J'} = \frac{r'^2}{r^2} \quad (4.2.2)$$

Thus the intensity for a point source of light at any point is inversely proportional to the square of the distance from the point to the source

$$J = k' \frac{1}{r^2} \quad (4.2.3)$$

where  $k'$  is a constant that depends on the point source.

The point source constructed for the measurement is shown in Figure 4.4. A 12 V tungsten filament light bulb is used as the light source. A piece of frosted glass and several pieces of plain paper are put in front of the light bulb to diffuse the light completely to get a uniformly scattered light output. An iris is put in front of the frosted glass and set to its smallest size, which has a diameter of about 0.5 mm.

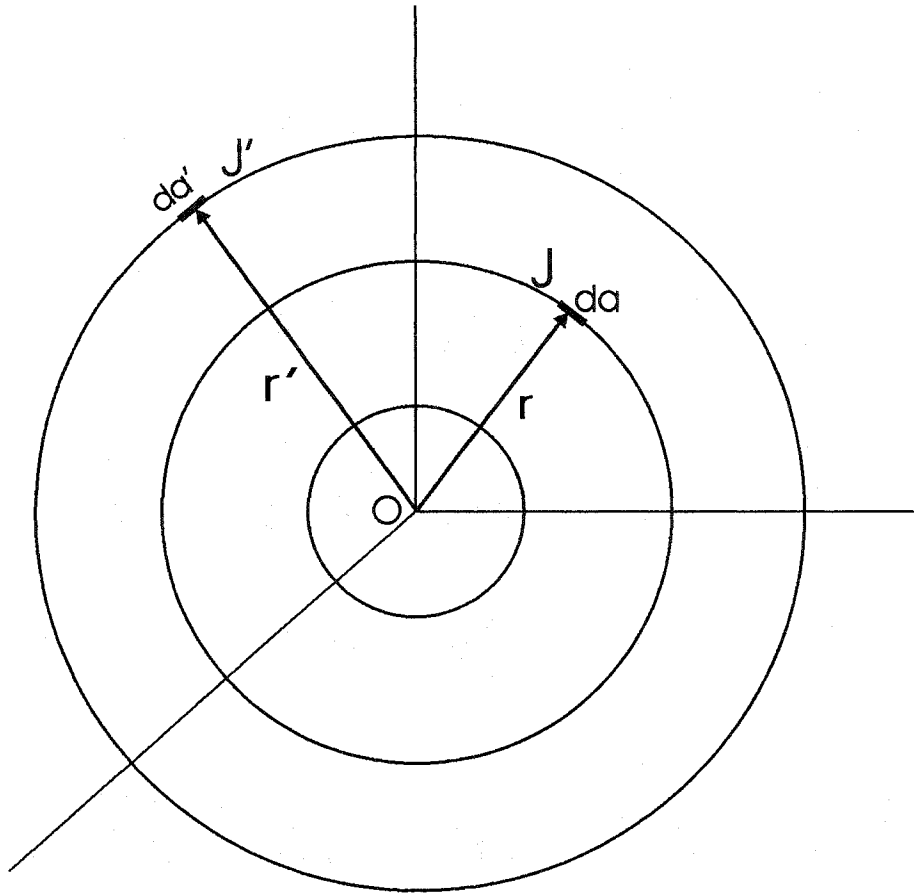


Figure 4.3 Spherical wavefronts produced by a point source of light at O

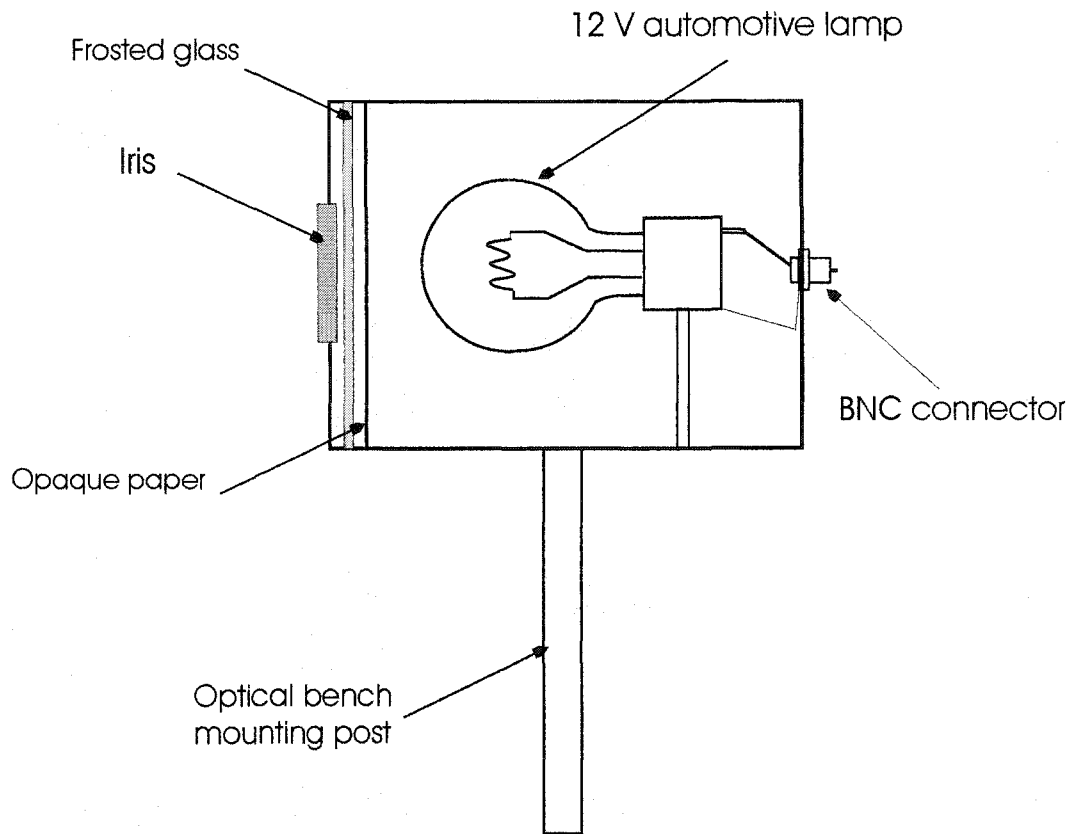


Figure 4.4 Schematic of point source of light

The photodetector response versus the inverse distance squared from the light source is shown in Figure 4.5. The photodetector signal is negative due to the characteristics of the photodetector, which will be discussed in detail in Chapter 7. In the following parts of the thesis, most of the photodetector output except the ones in Figure 4.8 and Figure 4.11 will be plotted in absolute value of the photodetector output current for the ease of understanding and data processing. The distance from the light source to the photodetector varies from 7.9 cm to about 50 cm. Experimental data are least square fitted onto a straight line and the equation of the line is shown on the graph.

From equation (4.2.3) and the experimentally fitted equation of Figure 4.5, we can see the photodetector signal at any point is linear with respect to the intensity of the light at that point:

$$I_d = k'J \quad (4.2.4)$$

where  $k'$  is a constant depending on the characteristics of the photodetector and the light source. If we assume the Melles Griot photodetector has a linear response to the intensity of the incident light, this experiment proves that the light source behaves as a point source of light. This light source will be used as a point source of light to test for linearity of the CMOS detector in Chapter 7.

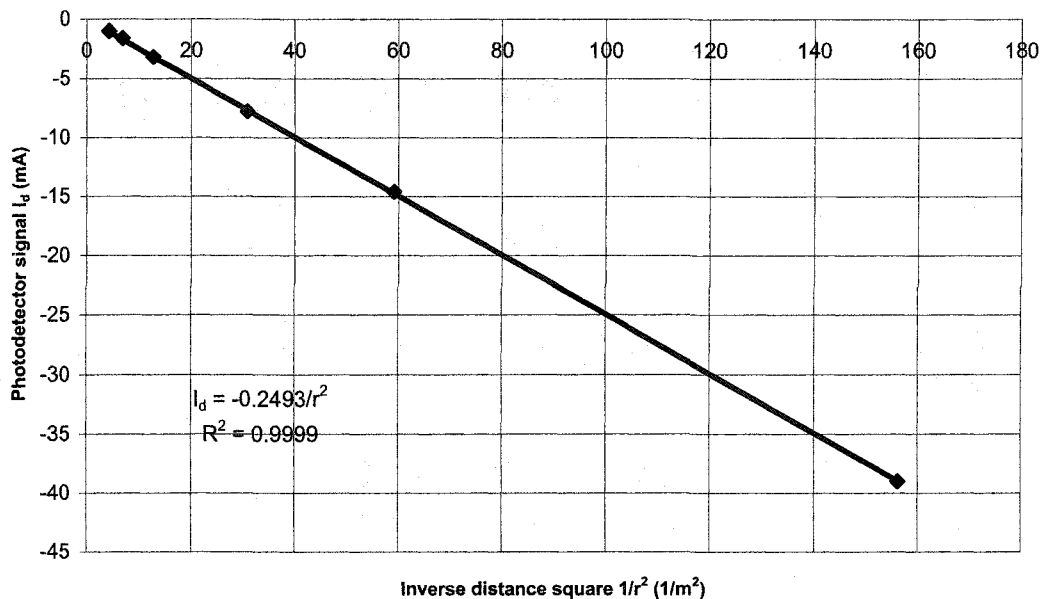


Figure 4.5 Photodetector signal versus inverse distance squared of the light source

### **4.3 Digital constant power supply unit and data acquisition unit**

The mode of operation of the micro-radiator system is crucial to its successful functioning. The signal from the photodetector must be constant under constant operational conditions. This is especially critical for the measurement of radiation and its sensitive dependence on the emitter temperature. This section examines the three modes of operation of the emitter: constant current, constant voltage and constant power.

The polysilicon has a positive temperature coefficient of resistance  $\alpha_T$ , which is constant provided the power supplied to it is lower than a threshold value [1]. The resistance  $R$  will increase when a current passes through the polysilicon due to Joule heating and for large currents can lead to thermal runaway and ultimately to destruction. We described earlier that the thermal response time of these micro-radiator is approximately 20 ms. However, there exists a phenomenon where the polysilicon resistance increases slowly with time while under power when the power is above a threshold value. The threshold power can be as low as 9 mW for microresistors similar to the ones used in this project [1]. Figure 4.6 shows the radiation signal from the micro-radiator detected by the photodetector versus time when a constant current  $I_0 = 1.7 \text{ mA}$  is supplied to the micro-radiator at atmosphere pressure. The micro-radiator is operating above the threshold power where the resistance slowly increases. The magnitude of photodetector signal increases from 0.075 nA to about 0.14 nA in 350 seconds, which means the magnitude of photodetector signal increases about 87% in this time. This is due to the power supplied to the polysilicon,  $W = I_0^2 R$ , which increases when  $R$  increases; the corresponding increase in temperature  $T$  shifts the polysilicon emission further into the response region of the detector.

At the cessation of the experiment in Figure 4.6, the micro-radiator room temperature resistance,  $R_0$  and the temperature coefficient of resistance,  $\alpha_T$ , have permanently changed. The existence of changing values of  $R_0$  and  $\alpha_T$  are linked to the polysilicon resistance trimming process that has been investigated for a number of years [2]. A number of mechanisms for these changes will be discussed in Chapter 5.

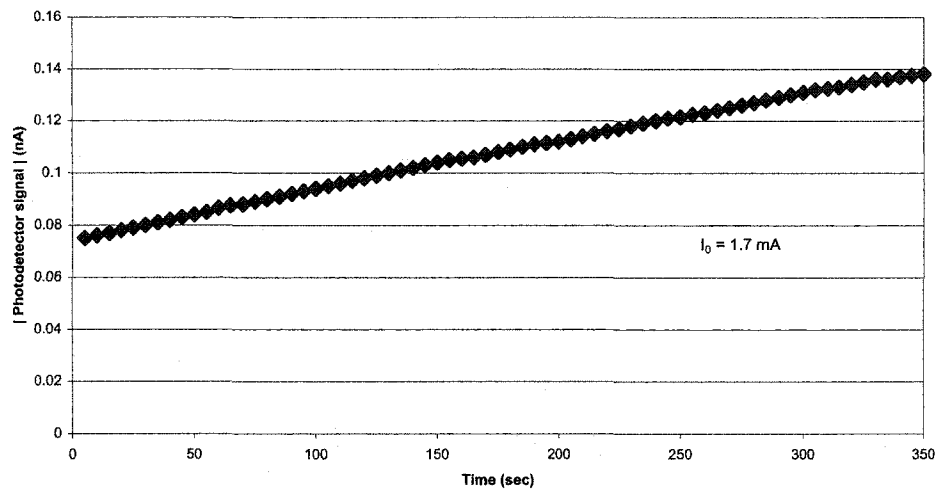


Figure 4.6 Variation of photodetector signal versus time operating with constant current at atmospheric pressure

Figure 4.7 shows the photodetector signal when a constant voltage  $V_0 = 10\text{ V}$  is applied to the micro-radiator. Data were recorded every five seconds. The power supplied to the polysilicon,  $W = V_0^2 / R$ , decreases when  $R$  again slowly increases due to the effect discussed above. The corresponding decrease in temperature  $T$  also shifts the polysilicon emission out of the detector response region. The magnitude of the photodetector signal decreases from 0.65 nA to about 0.51 nA in 350 seconds, a decrease of about 22%.

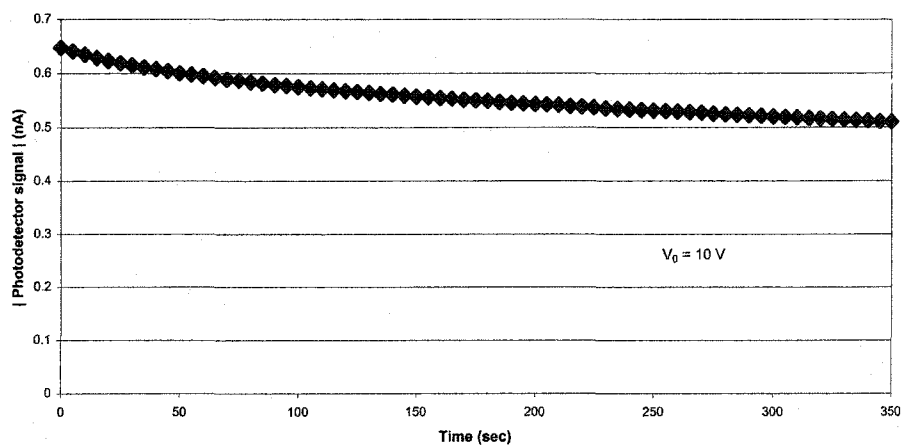


Figure 4.7 Variation of photodetector signal versus time operating with constant voltage at atmospheric pressure



Because the resistance of polysilicon and hence the radiation signal increases or decreases with time in the above two modes of operation above the power threshold, neither of them is suitable for use as a pressure sensor.

In order to keep the radiation from the micro-radiator constant at a given pressure, we keep the power supplied to the micro-radiator constant. Haswell and Robinson developed an analog constant power system [3] and Hogg, Warkentin and Thurston developed a digital constant power system in 1994 [4]. The digital constant power system is modified and used in this project to allow the users to not only apply constant power, but also to be able to apply power waveform functions other than just constant power to the micro-radiator.

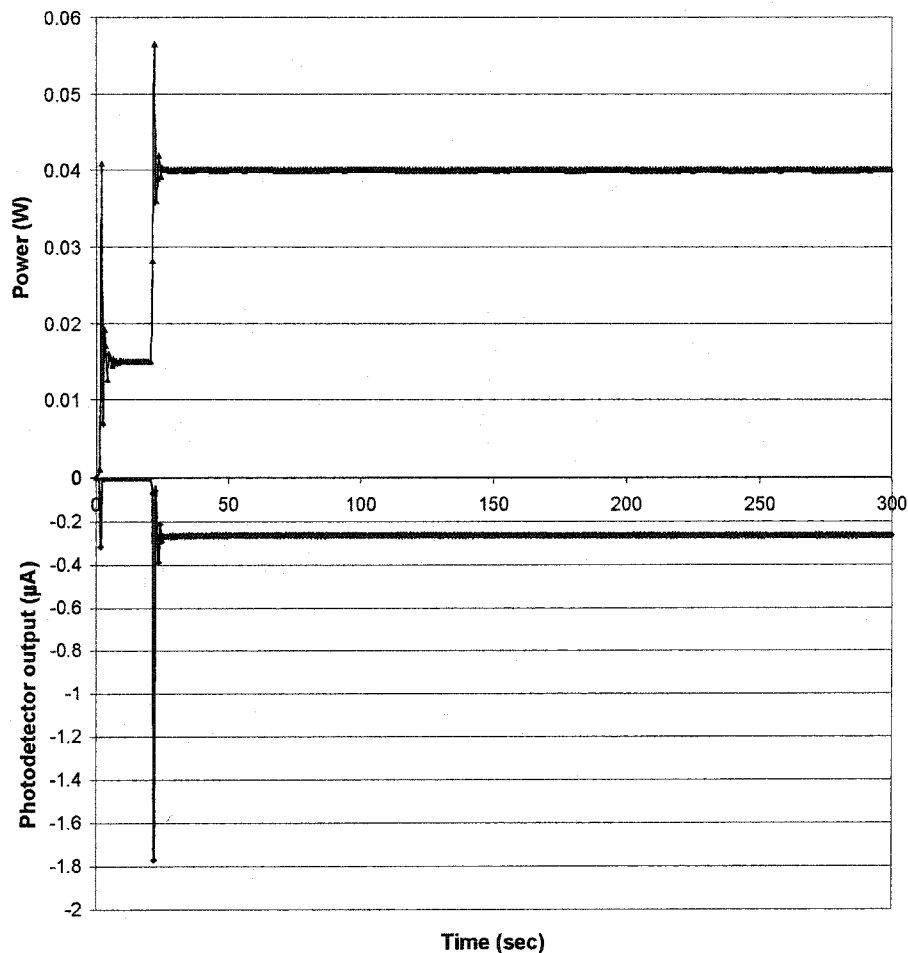


Figure 4.8 Photodetector signal (bottom) showing the radiation follows in a non-linear fashion the variation of the power supplied to the micro-radiator (top)

Figure 4.8 shows the output of the photodetector when it is used to monitor the radiation from a micro-radiator heated under a constant power of 40 mW using the CPS. The top half of the figure shows the electrical power applied to the micro-radiator while the lower half shows the photodetector signal. Before the constant power level reaches 40 mW, a power level of 15 mW was used to pre-heat the device for about 20 seconds to decrease the magnitude of the overshooting at the beginning of 40 mW power stage. Details about the overshooting will be described in the following section. The radiation from the micro-radiator at 40 mW was in the visible range, which indicates the temperature of the polysilicon was very high and its resistance changes significantly. However, the photodetector signal remains constant due to the constant input power, which makes the CPS a suitable operation mode for pressure sensing using the micro-radiator.

#### **4.3.1 Test of constant power supply unit**

The CPS is the main part of the experiment control system. The CPS controls a Keithley 236 Source Measure Unit (SMU) using a computer program written in Instrument Basic and supplies constant power through the micro-radiator at a specified level regardless of the value of the resistance. The other part of the experiment control system is a data acquisition unit, which acquires output data of the photodiode from a digital multi-meter. Details about the experiment control system including the design flow chart, user interface and the Instrument Basic program are included in Appendix B.

The digital constant power supply unit was tested with different powers from the CPS applied to the micro-radiator operated at atmospheric pressure. Figure 4.9 (a) shows a typical result when the power supplied is a staircase function. The power applied to the micro-radiator increases 2 mW every 30 seconds from 16 mW up to 50 mW. The micro-radiator starts to glow from about 30 mW.

For a power level not high enough to cause failure of the polysilicon micro-radiator, the fluctuation of the digital constant power is less than 0.2% after the initial homing-in of the system onto the set power. Figure 4.9 (b) shows the details of the overshoot and

homing-in processes. This procedure takes a longer time at higher constant power when the temperature of the micro-radiator is higher, but it usually takes less than five seconds. The cause of the power over-shooting at the beginning of each power level is due to the continuous change of polysilicon resistance and the way the software calculates the current output. Details about the programming can be found in the Appendix. If the power supplied to the micro-radiator is too high, the resistance of the micro-radiator increases dramatically to infinity, which will cause the power shown in Figure 4.9 to increase, ultimately, to infinity.

Figure 4.10 shows the variation of the power dissipated by the micro-radiator under a series of power levels from 5 mW to 15 mW for 10 minutes respectively. The data were only recorded when the change in power is larger than 0.01%. The fluctuation of the power is less than 0.15% after the initial homing-in of the system. A power level about half the magnitude of the specified power is supplied to the micro-radiator at the beginning of each test to minimize the magnitude of power over-shooting.

The digital constant power supply unit is also been tested for long-term stability and yielded power fluctuations of  $\pm 0.4\%$  over an 80-hour period.

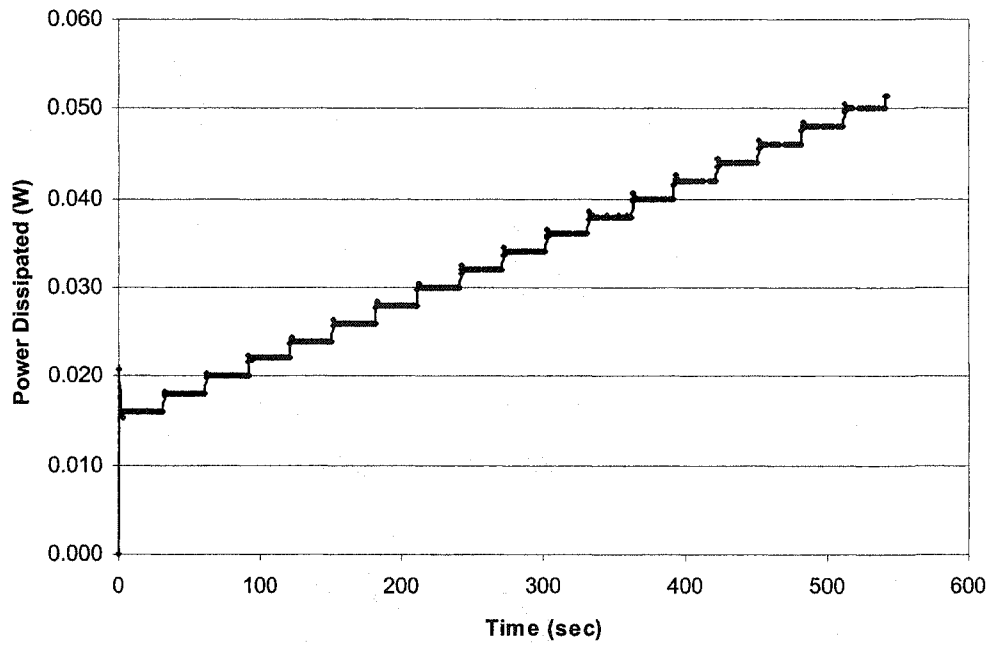


Figure 4.9 (a) Test of digital constant power supply unit with staircase function power output

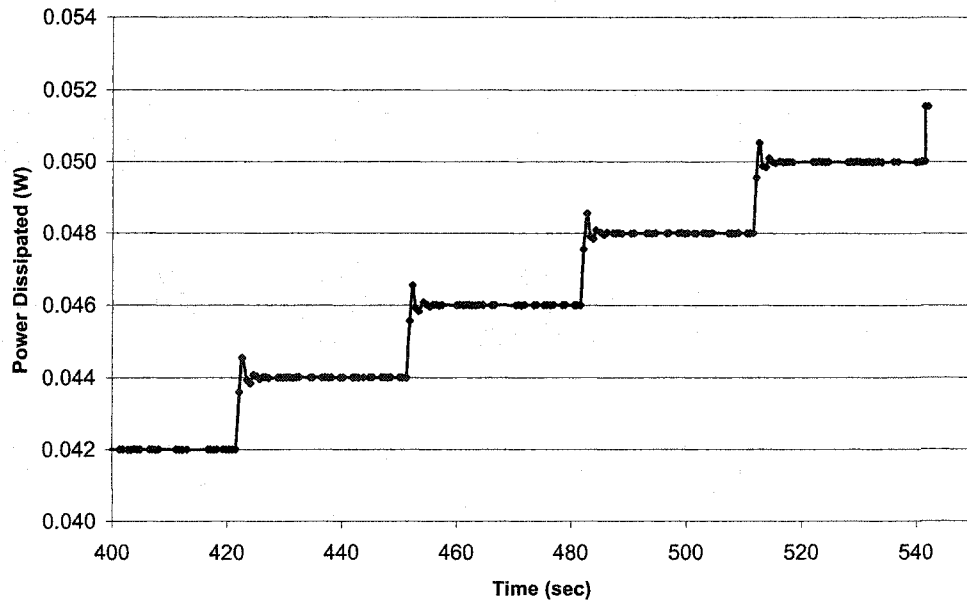


Figure 4.9 (b) Test of constant power supply unit showing the "homing-in" procedure of the system

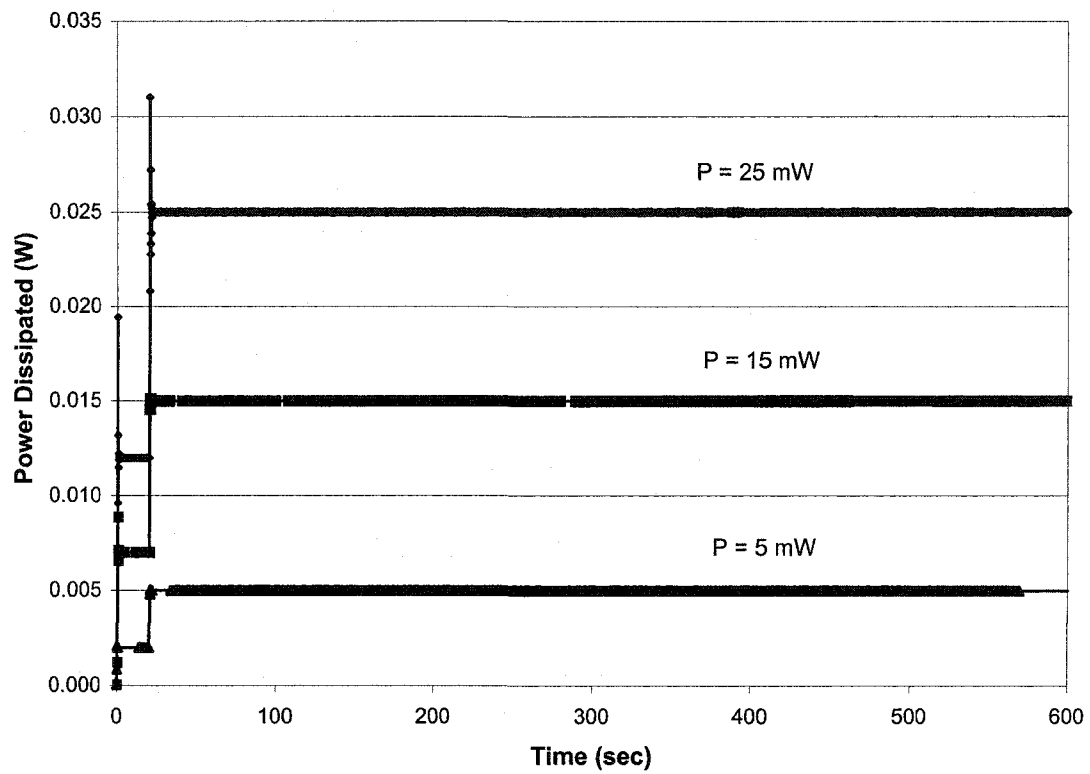


Figure 4.10 Test of constant power system operating at different powers

### 4.3.2 Test of experiment control unit

The Experiment Control System has been tested with the digital CPS supplying power to the micro-radiator and the data acquisition unit monitoring the output from the photodetector. Figure 4.8 shows the result under 40 mW operation power. Figure 4.11 magnifies the first 50 seconds of Figure 4.8 to show the details of the power and photodetector signals. When the electrical power is bigger than a threshold (about 25 mW in Figure 4.11), the micro-radiator starts to emit a detectable signal. The overshoot of the 15 mW power step briefly exceeds this threshold at about 3 seconds; the photodetector thus registers a short pulse signal. With the power overshoot and homing in to the 40 mW power level, starting at 22 seconds, the photodetector signal shows a similar but non-linear variation before the applied power becomes constant. The photodetector signal stays constant after the homing-in of the CPS. The process of power homing-in takes about six seconds at the 15 mW level and takes less than five seconds at the 40 mW level. The experiment control system has also been tested under other powers and pressures. The variation of the constant power is less than 0.2% after the homing-in while the variation of the photodetector signal is less than 3%.

From the various experiments described above, we can see the Melles Griot photodetector is reliable to measure the radiation from the micro-radiator and the output signal is linear to the intensity of incident light. A constant power supply is chosen instead of constant current or voltage power sources to keep the radiation from the micro-radiator constant at a fixed pressure. Therefore, the variation of the radiation from the micro-radiator is only due to the temperature change caused by the pressure change at a given constant power and will be used as the measurand of the surrounding gas pressure as described in the following chapter.

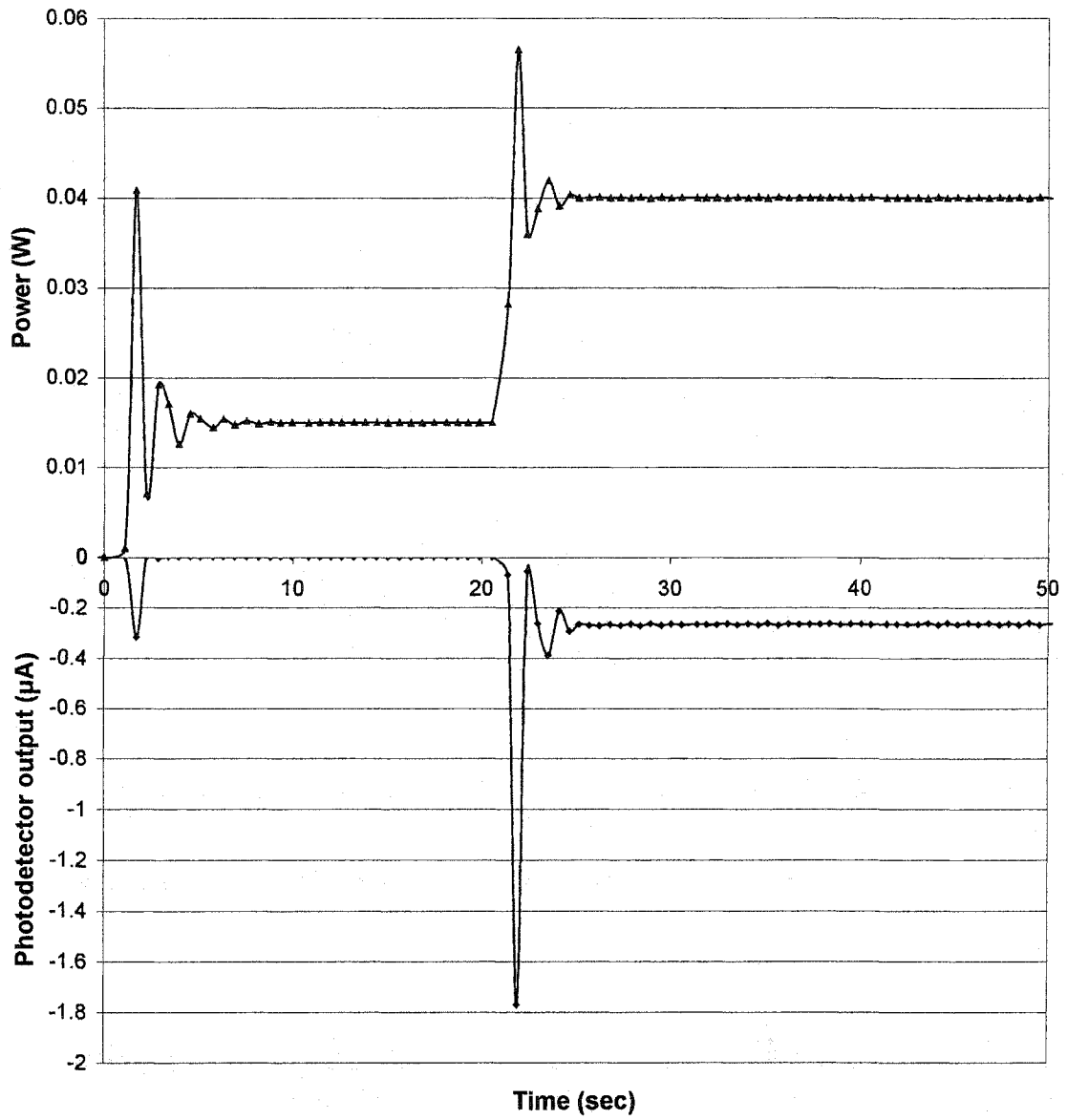


Figure 4.11 Magnified part of Figure 4.8 showing the details of photodetector and power signals

#### 4.4 Measurement sensitivity

The radiation power from the micro-radiator can be evaluated using the photodetector. The output current of the photodetector  $I_d$  can be expressed by:

$$I_d(T) = \kappa \int_0^{\infty} \varepsilon(\lambda, T) \cdot E_{\lambda, b}(\lambda, T) \cdot R(\lambda) d\lambda \quad (4.4.1)$$

in which  $\lambda$  is the radiation wavelength,  $T$  the temperature and  $\varepsilon$  the emissivity of the micro-radiator,  $E_{\lambda, b}$  is the emissive power of the micro-radiator and can be calculated by equation (1.4),  $R(\lambda)$  is the responsivity of the photodetector as shown in Figure 4.2 and  $\kappa$  is a proportionality constant to account for the detector - radiator geometry and configuration. We assume here that the emitter has a constant temperature  $T$  over its surface. The responsivity of the photodetector is the current output of the photodetector when the photodetector is illuminated with incident light of 1 W at various wavelength. Since the National Institute of Standards and Technology (NIST) only provided the responsivity data between 400 nm and 1100 nm, the responsivities below 400 nm and above 1100 nm are extrapolated from the slope of the last two numbers at each end, as shown in Figure 4.12.

The emissivity of the micro-radiator  $\varepsilon$  is a function of both wavelength  $\lambda$  and temperature  $T$ , but a value of 0.8 is used here for simplicity of calculation. The feasibility of this assumption will be addressed later in Chapter 5. A value of 8% is used for the proportionality constant  $\kappa$  to account for the detector - radiator geometry and configuration, as shown in Figure 4.1.

The emissivity of the micro-radiator  $\varepsilon$  is a function of both wavelength  $\lambda$  and temperature  $T$ , but a value of 0.8 is used here for simplicity of calculation. The feasibility of this assumption will be addressed later in Chapter 5. A value of 8% is used for the proportionality constant  $\kappa$  to account for the detector - radiator geometry and configuration, as shown in Figure 4.1.



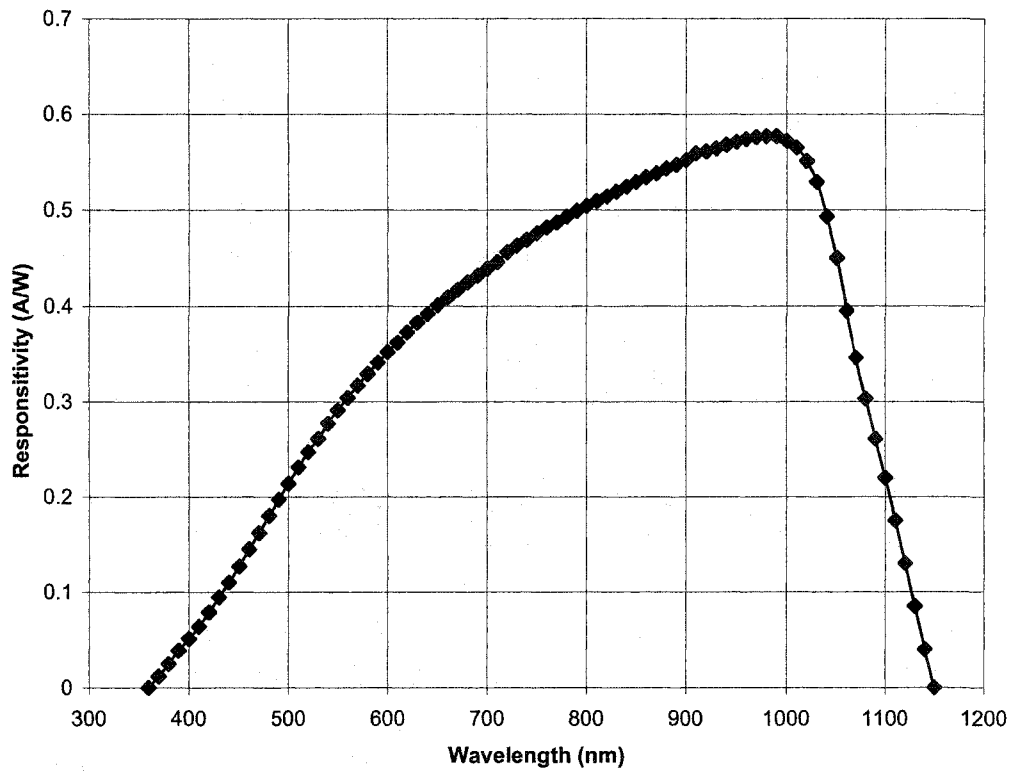


Figure 4.12 Extrapolated response of silicon photodetector 13 DAS 011/C

Figure 4.13 shows the integration results of equation (4.4.1) compared with the total emissive power, equation (1.5), and resistance variation, equation (1.3), of a typical micro-radiator at different temperatures. At a given temperature, the emissive power  $E_{\lambda,b}(\lambda, T)$  of the micro-radiator was calculated from 360 nm to 1150 nm in steps of  $d\lambda = 10$  nm using the Boltzmann distribution. Then the total signal detected by the photodetector was numerically integrated using rectangles, which calculates the sum of products  $E_{\lambda,b}(\lambda, T)$ ,  $R(\lambda)$  and  $d\lambda$ . We felt that other numerical integration methods such as Simpson's rule or the trapezoidal rule were not necessary, as we were interested in working a qualitative comparison of the resistance, radiation and photodetector output as shown in Figure 4.13.

From Figure 4.13, we can see the output of the photodetector increases much more sharply with the temperature than the variation of total emissive power, which varies as  $T^4$ , and the output of the traditional Pirani gauge, which measures the resistance variation

with temperature using equation (1.3). For a micro-radiator with  $0.01 \text{ mm}^2$  surface area and a temperature change of  $\Delta T = 1400 - 400 = 1000 \text{ K}$ , the magnitude of the photodetector output signal changes by about  $10^{10}$ , while the magnitude change of the total radiation changes by about  $10^3$  and the resistance change is less than 10. The dramatic increase of the photodetector output signal is due to the blackbody distribution not only increasing in absolute magnitude, but shifting more into the response region of the photodetector, which makes it the most sensitive detection method of the three compared in Figure 4.13.

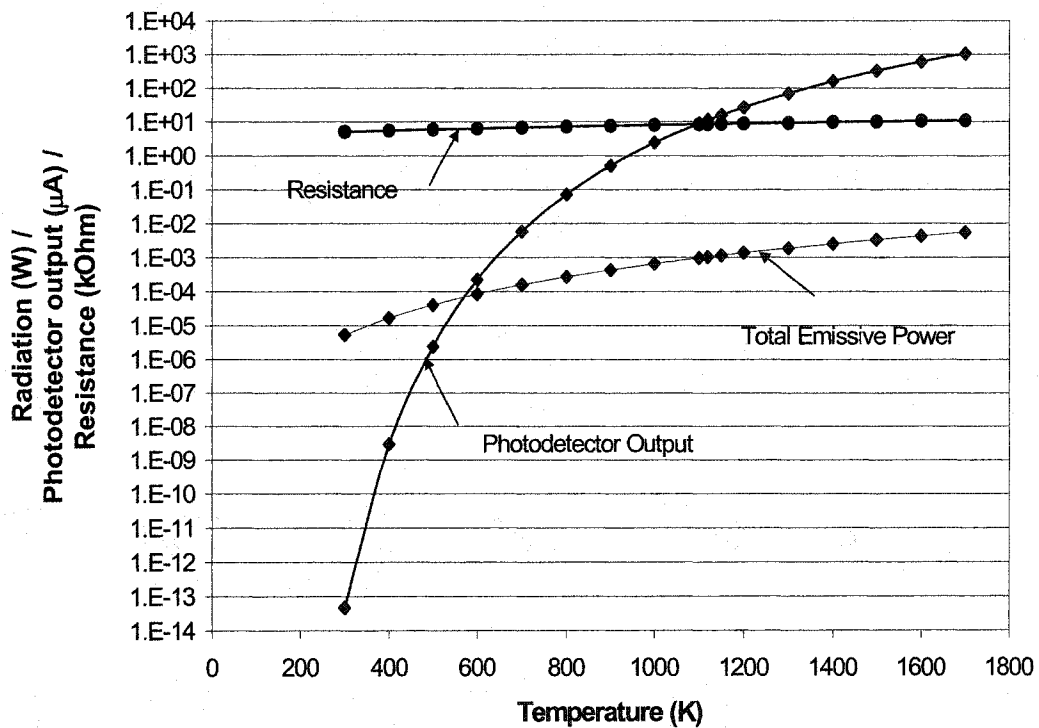


Figure 4.13 Comparison of the photodetector output with the total radiation and resistance of the micro-radiator as a function of temperature

From an analytic form of the photodetector output curve in Figure 4.13 and the curves in Figure 3.6, we can plot the photodetector output versus the gas pressure. Figure 4.14 shows the variation of photodetector output with the pressure of surrounding gas under two different input powers along with the temperature versus pressure curves as shown in Figure 3.6.

From Figure 4.14, we can see the sensitivity of the micro-radiator pressure sensor is different with different input powers. Higher input power leads to bigger sensitivity at the linear heat transfer region and it also shifts the pressure-sensitive region to higher values. A power-switching scheme based on this feature will be introduced in Chapter 6 to increase the sensitivity and measurement range of the micro-radiator. Photodetector output calculated in Figure 4.14 will also be compared with experimental results in Chapter 6.

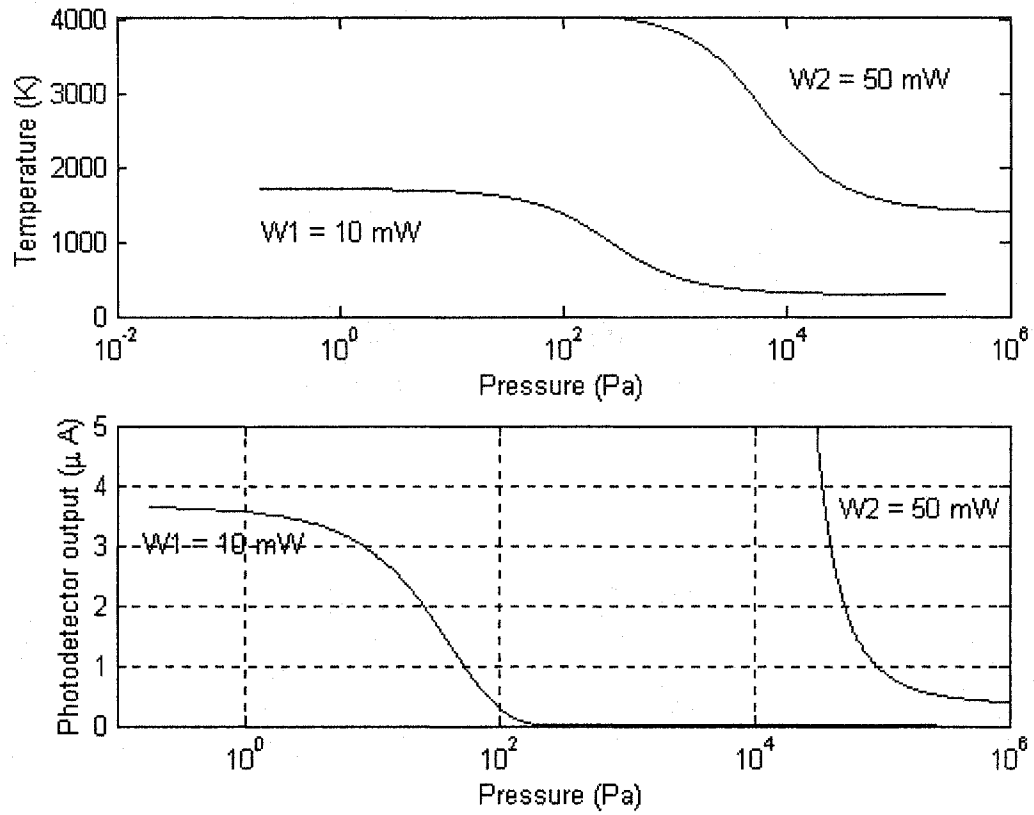


Figure 4.14 Micro-radiator temperature and photodetector output versus pressure operating at input powers of 10 and 50 mW

## References:

- [1] A. M. Robinson, "Mitel 1.5  $\mu\text{m}$  CMOS Process: Characterization Measurements of the Polysilicon Layers for Use in a Micro-sensor", *Canadian Microelectronics Corporation Report*, IC95-06, 1995.
- [2] J. A. Babcock, D. W. Feldbaumer and V. M. Mercier, "Polysilicon resistor trimming for packaged integrated circuits", *Tech. Dig., IEDM '93*, Washington, DC, 11 Dec. 1993, pp. 247-250.
- [3] P. Haswell and A. M. Robinson, "Constant power testing system for polysilicon microresistor characterization measurements", *Meas. Sci. Technol.*, vol. 4, 1993, pp. 957-961.
- [4] B. Hogg, P. Warkentin and R. Thurston, "Digital Constant Power System", CMPE 499 Project Report, Electrical Engineering Department, University of Alberta, April 1994.

## Chapter 5

### Device Characterization

The micro-radiator is characterized as an emitter in this chapter. Radiation from the micro-radiator, including radiation intensity, spectral and spatial distribution, is measured and the results are discussed.

A reliability study of polysilicon is also included in this chapter to find out the threshold operation power of the micro-radiator where the stability of the electrical characteristics starts to decay.

#### **5.1 Micro-radiator radiation measurements**

Figure 5.1 shows the experiment setup used to study the radiation from the micro-radiator. The micro-radiator is mounted on a ceramic 40-pin DIP (dual in-line package). The radiation is monitored with the photodetector. The incidence angle of the radiation to the photodetector is  $\theta$  and  $\phi$  is the azimuth angle of the photodetector. A large dynamic-range amplifier amplifies output from the photodetector and the Experiment Control System supplies a constant power to the micro-radiator and reads the amplified output of the photodetector.

##### **5.1.1 Micro-radiator radiation response with input power**

The radiation from the micro-radiator was measured at one atmosphere under different input powers, as shown in Figure 5.2. The photodetector was 2.5 cm away from

the micro-radiator and directly above it ( $\theta = 0^\circ$ ). Constant power input up to 60 mW was used to heat the micro-radiator; radiation was visible at about 30 mW input at atmospheric pressure.

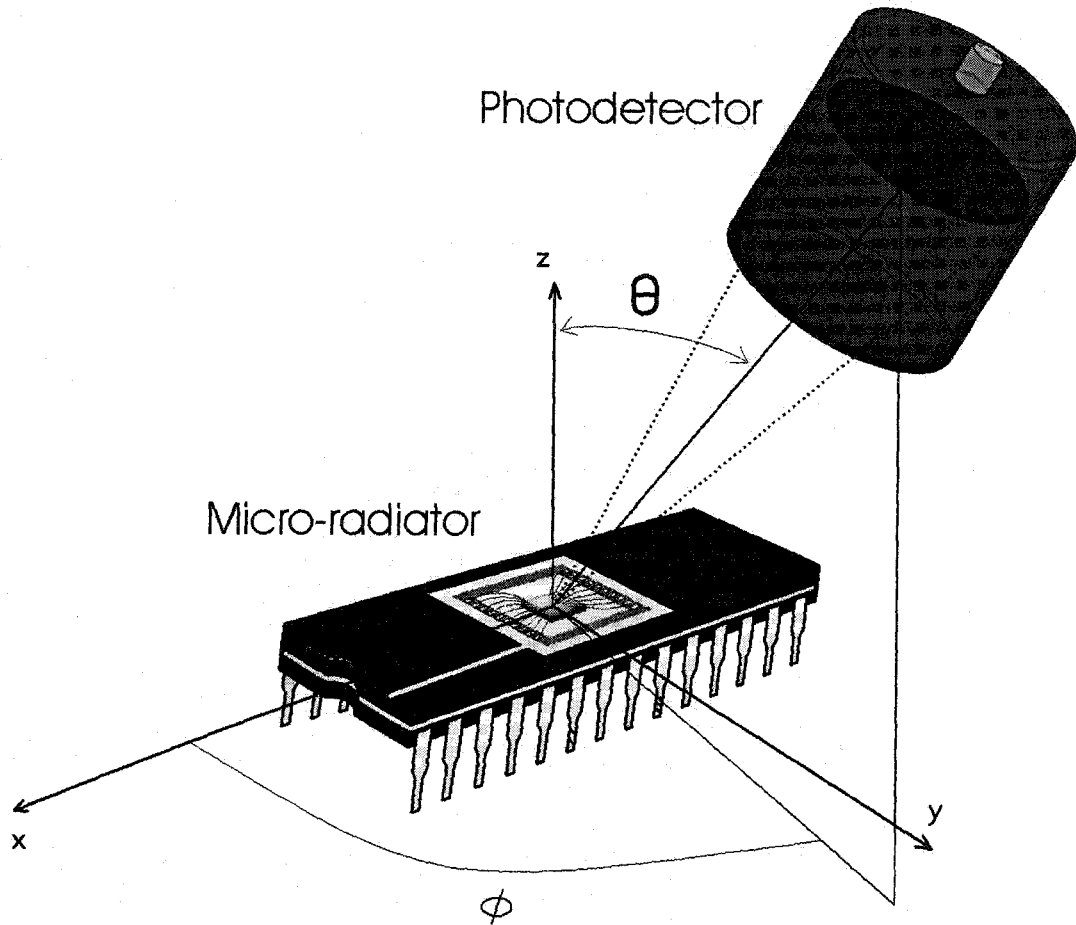


Figure 5.1 Experiment setup for radiation measurement

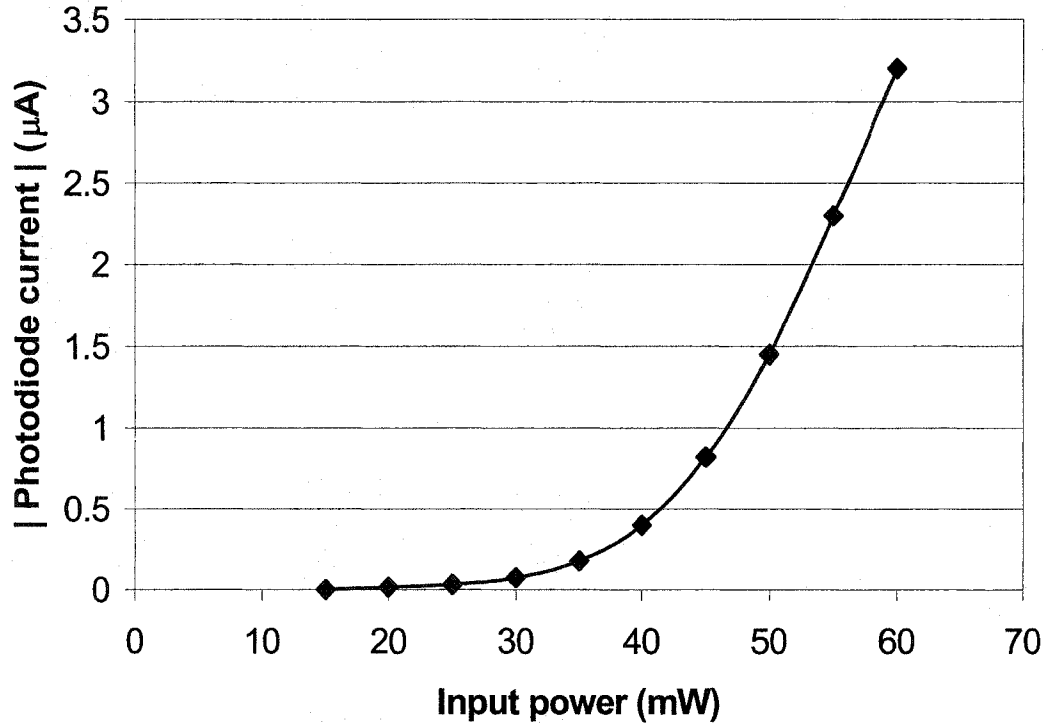


Figure 5.2 Photodetector signal versus the micro-radiator input power ( $\theta = 0$ )

From Figure 5.2 we can see the relationship between the radiation from the micro-radiator and the input constant power is a polynomial curve. After about 25 mW, the photodetector signal varies rapidly with the constant power input. Experiment data above 60 mW are not collected because the excessive heat will burn out the micro-radiator.

### 5.1.2 Micro-radiator radiation spectral analysis

The micro-radiator was treated as a gray body with an emissivity of 0.8 in Chapter 4 to calculate the photodetector output. In order to compare the radiation from the micro-radiator with the blackbody radiation, a spectral measurement is performed by inserting a set of filters between the micro-radiator and a HgCdTe infrared photodetector. The HgCdTe photodetector is fabricated by Electro-Optical Systems, Inc. (Model: MCT16),



with a sensitive range between 1  $\mu\text{m}$  and about 18  $\mu\text{m}$ . Figure 5.3 shows a schematic of the experiment setup. The input power of the micro-radiator was 50 mW. Radiation from it was collimated and focused using ellipsoidal reflectors and then detected by the HgCdTe photodetector after intensity modulation. A lock-in amplifier amplified the output of the photodetector. The filter characteristics are summarized in Table 5.1.

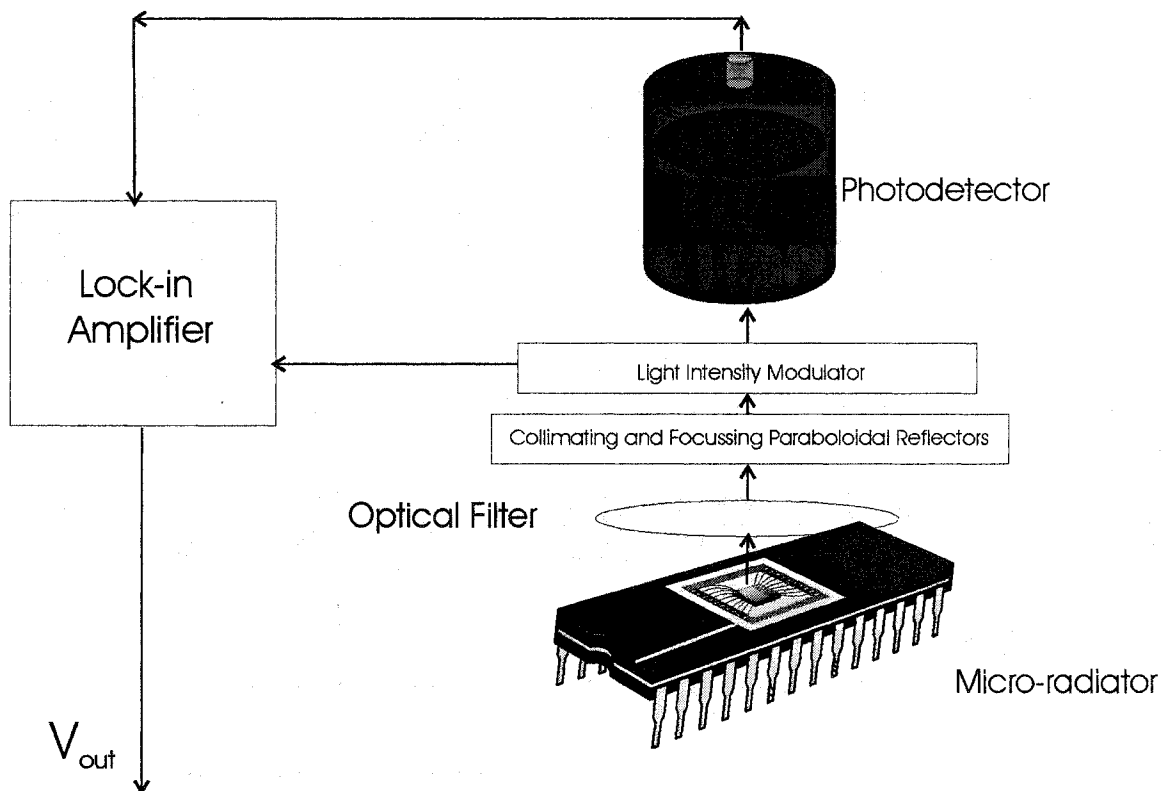


Figure 5.3 Apparatus used for radiation spectral analysis

Table 5.1 Optical filters and lock-in amplifier output

Filter Type	Center Wavelength ( $\mu\text{m}$ )	Bandwidth or Transmission range ( $\mu\text{m}$ )	Lock-in Amplifier Output (mV)	Relative spectral intensity
BP-1230-1580	1.40	0.35	0.7	0.18
LP-1000	1.47	0.94	10.7	0.90
LP-1600	2.07	0.94	13.5	1.00
LP-3000	3.72	1.44	10.5	0.33
BP-3900-110	3.95	0.11	1.4	0.55
SP-6000	4.97	2.06	8.4	0.17
SP-8750	7.55	2.4	7.2	0.07
LP-6000	7.99	3.98	9.2	0.035
BP-10500-385	10.69	0.385	0.3	0.12
LP-10800	14.67	7.74	4.2	0.01

- All filters are fabricated by Spectrogon Inc.

The relative spectral intensity at the center wavelength of each filter was calculated by dividing the photodetector output by the transmission of each filter and the response of the photodetector at that wavelength. The transmission of each filter is the product of the bandwidth of the filter and the average transmission rate. Please refer to Spectrogon Inc. homepage (<http://www.spectrogon.com>) for transmission curves of each filter for details. The resulting spectral radiation is normalized and plotted in Figure 5.4. Experimental data are least-squares fitted to a blackbody radiation curve.

The temperature of the least-squares-fitted curve is 1521 K and the corresponding peak of the emission can be calculated using Wien's Displacement Law [1]:

$$\lambda_{\max} = 2897.8(\mu\text{m} \cdot \text{K}) / T = 1.9 \mu\text{m} \quad (5.1.1)$$

Experimental data shows a good agreement with the blackbody radiation curve in Figure 5.4. Therefore, the assumption of a constant emissivity of micro-radiator surface used in Chapter 4 is feasible. The data divergence from the blackbody curve at 1.5  $\mu\text{m}$ , 4  $\mu\text{m}$  and 10.7  $\mu\text{m}$  is possibly due to an interference effect of the silicon nitride layer on the micro-radiator surface [2]. The temperature of the fitted blackbody curve is roughly in the same range as the temperature derived from measured resistance in Section 5.2.

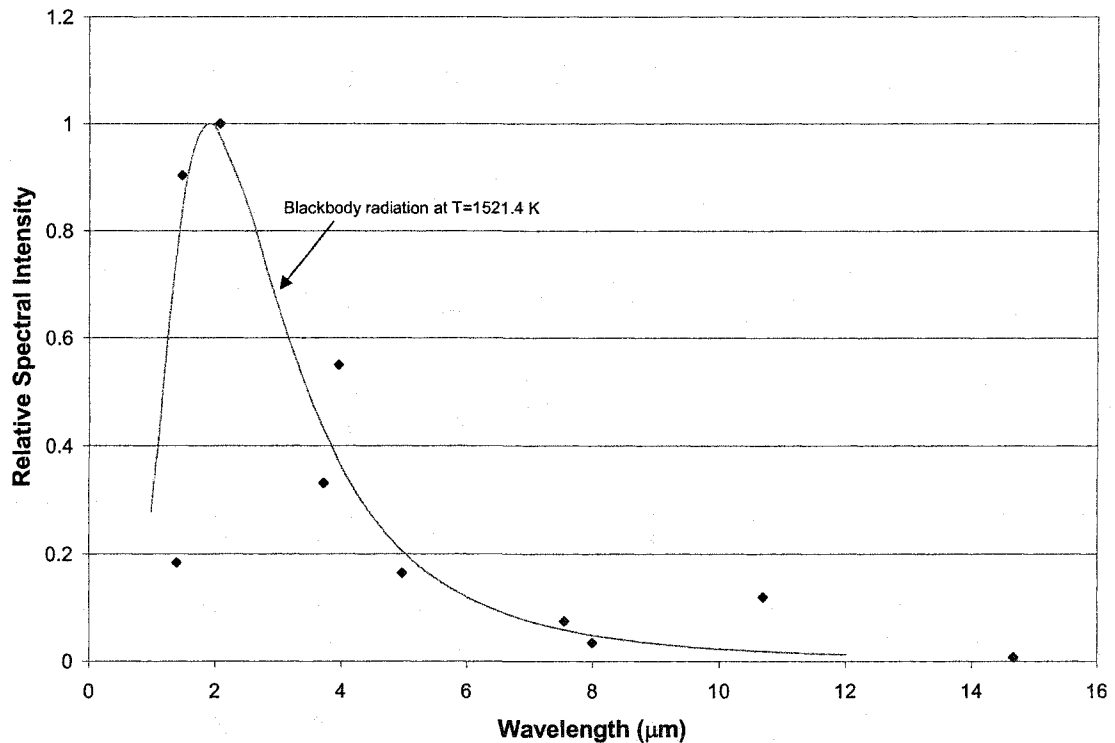


Figure 5.4 Normalized spectral distribution of a micro-radiator with 50 mW input power. The points are measured values.

Optical spectral radiation below 1.2  $\mu\text{m}$  was also measured with an Ocean Optics S2000 Miniature Fiber Optic Spectrometer calibrated with a tungsten filament lamp [3]. The sensitive range of the spectrometer is from 300 nm to 1200 nm. Figure 5.5 shows the experimental configuration. The micro-radiator was placed 2 mm away from the pinhole

(diameter: 200 micron) of the optical fiber. Light from the micro-radiator enters the optical fiber and is efficiently transmitted to the spectrometer, which is the middle of Figure 5.5. Once in the spectrometer, a spherical mirror collimates the divergent light emerging from the optical fiber. Then a plane grating diffracts the collimated light and a second spherical mirror focuses the resulting diffracted light. An image of the spectrum is projected onto a 1-dimensional linear CCD array, and the data is transferred to a computer through an A/D card.

Three different constant powers from 35 mW to 70 mW were used to successively heat the micro-radiator to incandescence. Typical results from 650 nm to 1200 nm are shown in Figure 5.6. The radiation below 600 nm is very small and barely detectable with the grating provided by the Ocean Optics S2000 spectrometer.

The spectral distribution measured by the Ocean Optic spectrometer is far from a gray body emission. This is mainly due to the wavelength range measured by the Ocean Optic spectrometer is only a small part of the micro-radiator emission. From Figure 5.4 we can see the radiation from micro-radiator is mainly in the infra-red region. Therefore, peaks around 930 nm and minimum radiance around 650 nm and at 1170 nm shown in Figure 5.6 is due to the interference effects of the silicon nitride film.

The refractive index of silicon nitride,  $n$ , is 1.98. Since the minimum radiance point around 650 nm is not accurate, the wavelength difference between minimum radiance was calculated by:

$$\Delta\lambda = 2 \times (1170 - 930) = 480nm \quad (5.1.1)$$

The film thickness of the interference layer can be calculated by:

$$d_{film} = \lambda_{max}^2 / 2n\Delta\lambda = 455nm \quad (5.1.2)$$

This result agrees well with the thickness of the silicon nitride layer on top of the micro-radiator surface.

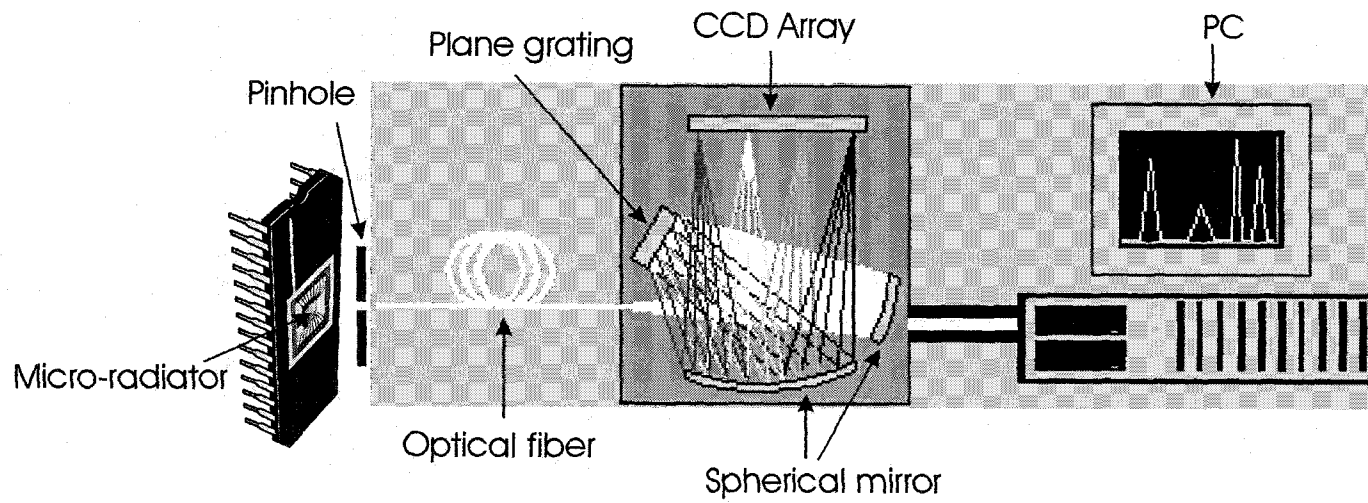


Figure 5.5 Spectral emissive power analysis experiment setup

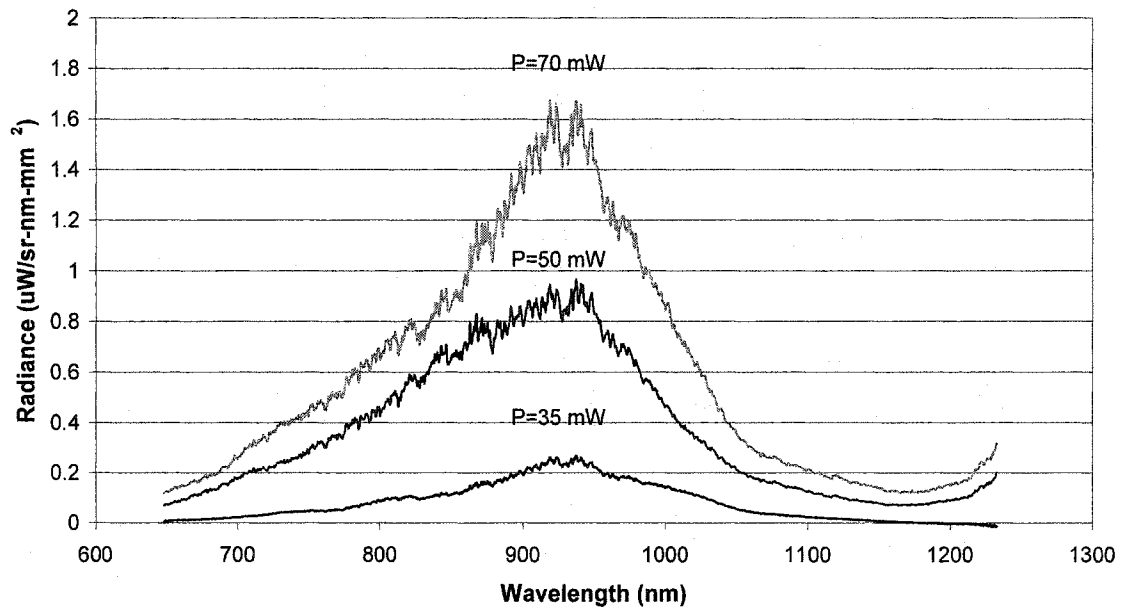


Figure 5.6 Spectral emissive power of the micro-radiator from 650 nm to 1200 nm

### 5.1.3 Micro-radiator radiation spatial distribution

Figure 5.7 shows the radiant intensity distribution as a function of the incidence angle  $\theta$ , measured from the perpendicular to the plane of the micro-radiator as shown in Figure 5.1. The measurement was done by varying the incident angle  $\theta$  between  $0^\circ$  and  $90^\circ$ . The distance between the photodetector and the micro-radiator is constant about 5 cm. The azimuth angle of the photodetector  $\phi$  was varied from  $0^\circ$  to  $360^\circ$ . The experimental results are independent of  $\phi$  and closely follows Lambert's cosine law.

Lambert's cosine law is a mathematical statement that the radiance of certain idealized optical sources is directly proportional to the cosine of the angle with respect to the direction of maximum radiance, from which the source is viewed [4]. Lambert's cosine law is plotted as a series of "+"s in Figure 5.7.

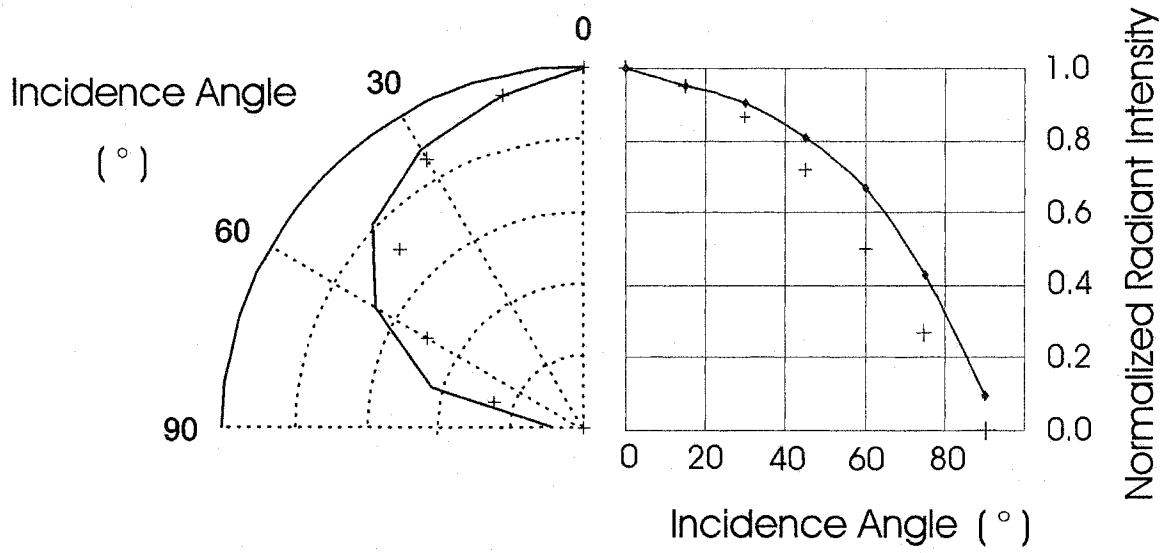


Figure 5.7 Normalized angular radiant intensity of a micro-radiator as a function of the polar angle  $\theta$

## 5.2 Reliability study of polysilicon

Reliability is one of the most important characteristics of a sensor, and the reliability of polysilicon film has been extensively studied in the past decade [5-9]. Research results proved that high thermal isolation with micromachining could result in high resistor temperature, leading to significant resistance drifts or even failure of the device. In this section, the reliability of the micro-radiator is studied using the Keithley Source Measure Unit.

Figure 5.8 (a) shows typical voltage current characteristics of the micro-radiator at atmospheric pressure. The data were obtained with a series of current steps from 0 to 2 mA applied to the micro-radiator and measuring the voltage at the same time. The step of the input current is 0.1 mA. Experimental data from the first sweep (curve marked “Sweep 1”) was slightly above the traces obtained with the following sweeps (curves marked with “Sweep 2-6”). The repeatability of the voltage-current curves after the initial sweep is very good and the data were least square fitted to a polynomial equation shown in the figure.

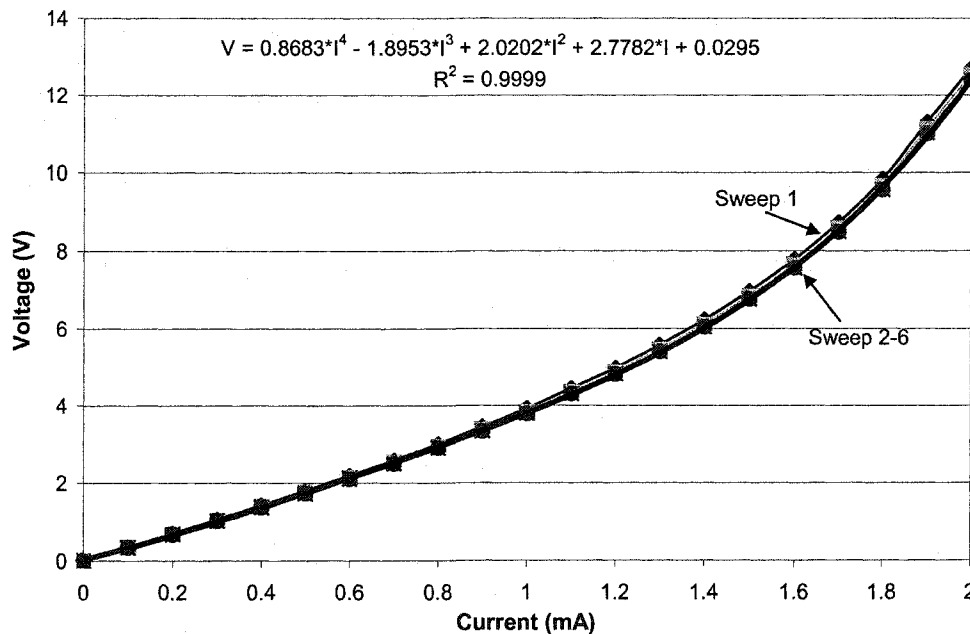


Figure 5.8 (a) Voltage-current characteristics of micro-radiator for a current from 0 to 2 mA



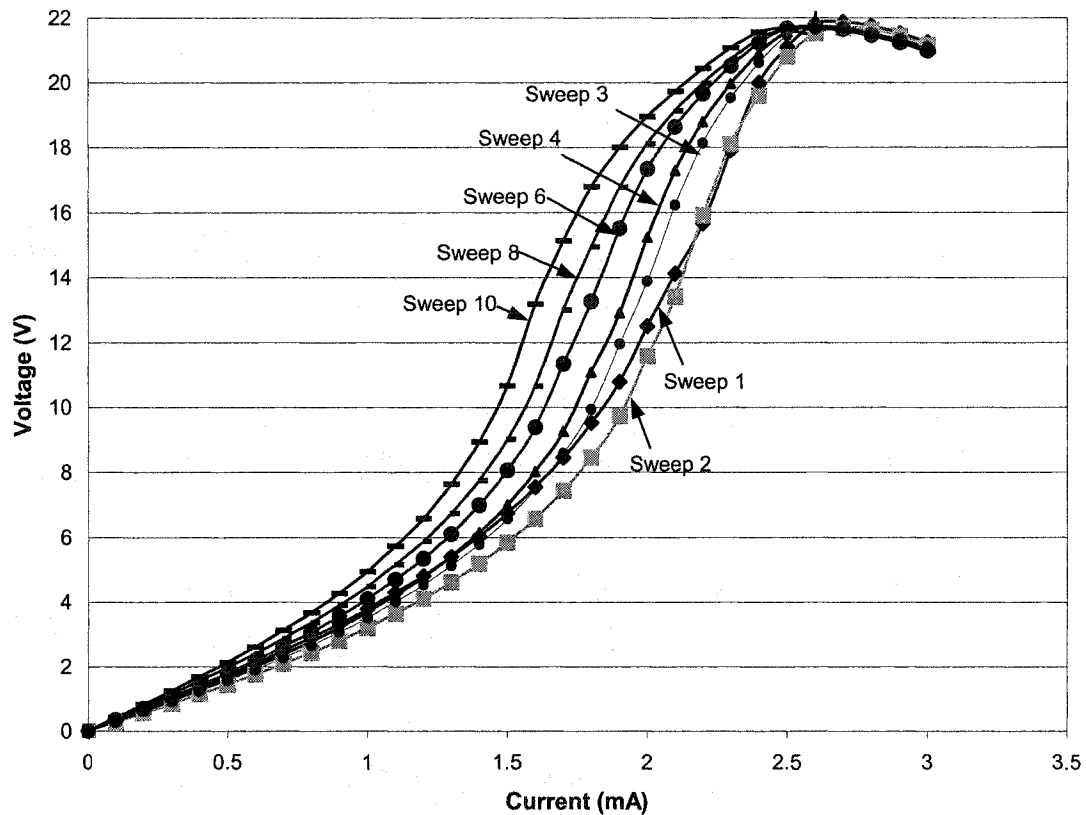


Figure 5.8 (b) Voltage-Current characteristics of micro-radiator for a current from 0 to 3 mA

If we increase the maximum current to 3 mA on the same resistor, the shape of the voltage-current characteristic curves change, and are shown in Figure 5.8 (b). The input current is started from 0 to 3 mA in steps of 0.1 mA. At relatively low current, the voltage across the micro-radiator increases with increasing current due to the positive temperature coefficient of the polysilicon. After the current reaches 2.6 mA, which corresponds to a power about 56 mW, the voltage starts to decrease, similar to what was observed by others [5,9,10,11].

After the first sweep up to 3 mA, the voltage-current characteristic curves start to drift from their original trace. For currents below 2.2 mA on the second sweep, the measured voltages are smaller than the ones obtained from the first sweep and are approximately the same as the first sweep after 2.2 mA. This is a general behavior observed on several

micro-radiators, although the point where two traces cross may be different than 2.2 mA. The voltage-current characteristic curves drift to the left from the third sweep and keep drifting in the same direction on the following traces. Sweeps 5, 7, and 9 are not shown in Figure 5.8 (b).

The resistance of the micro-radiator as a function of input current is plotted in Figure 5.9 (a). The data are taken from sweeps 1, 4, 6, and 10 shown in Figure 5.8 (b). A maximum in each curve occurs, after which the resistance decreases. The point where the resistance is maximum moves to the left with sweep number, similar to what was observed in Figure 5.8 (b).

The resistance of polysilicon starts to decrease after a threshold of 2.6 mA in air, which corresponds to a threshold power of 56 mW and a threshold current density of  $1.7 \times 10^5 \text{ A/cm}^2$ .

Resistance of the micro-radiator was also plotted as a function of input power in Figure 5.9 (b). The input power was calculated by  $W = I^2R$  and the average temperature of the micro-radiator can be estimated with the relationship between resistance  $R$  and temperature  $T$ :

$$R(T) = R_0[1 + \alpha_T(T - T_0) + \beta_T(T - T_0)^2 + \dots] \quad (5.2.1)$$

where  $\alpha_T$  is the temperature coefficient of resistance and equal to  $1.09 \times 10^{-3}$ ,  $\beta_T = 7.4 \times 10^{-7}$  [9],  $R_0$  is the room temperature resistance, and  $T_0$  is room temperature (20°C). The room temperature resistance  $R_0$  changes after each sweep, as shown in Figure 5.9 (a), changing from about 3.5 kΩ before the first sweep to about 4.2 kΩ after sweep 10. This is only a crude calculation because values of  $\alpha$  and  $\beta$  were obtained in [9] experimentally in the temperature range from 20 °C to 400 °C, and we are using them well beyond this range. The temperature of the micro-radiator at different input powers can be calculated by solving equation (5.2.1). The calculated temperature versus input powers for the first and last sweep is shown in Figure 5.9 (c), where we used the appropriate value of  $R_0$  for each sweep. The maximum temperatures for sweep 1 and sweep 10 are about 1100 K and 1200 K. The fact that temperature is not the same for a given input power except at low

power ( $< 5$  mW) on each sweep means that  $\alpha$  and  $\beta$  have changed after each sweep. The temperature calculated after these maximum points are not valid, because equation (5.2.1) is no longer valid at high temperatures. Other effects and processes are occurring which equation (5.2.1) is incapable of describing.

This resistance decrease occurs because the increase in temperature at increasing currents leads to significant reduction in the grain boundary barrier potential and possibly leads to formation of narrow filaments of molten silicon creating low resistivity paths for current flow [5]. Movement of grain boundaries leading to grain growth or recrystallization, which subsequently lead to lower resistivity of thin polycrystalline film, is also possible [6]. Electro-migration has also been observed with high gain Optical Beam Induced Current imaging at high temperature as reported in [8]. Catastrophic failure has been observed if the polysilicon micro-radiator is heated under excessively high power for very long time or after many pulses of heating cycle. In this project, the working condition of polysilicon micro-radiator is controlled below the threshold power of 56 mW in air to avoid the resistance drifts, and to extend the lifetime of the devices.

The above experiments have also been performed at a pressure of 50 mTorr. The general behavior and the shape of the resistance versus the input current curves remain the same, but the threshold current decreases to 1.1 mA and the threshold power decreases to about 10 mW.

In conclusion, the polysilicon micro-radiator is not electrically stable at high temperature. Many complicated processes occur under high input power which we cannot describe or understand well. The best we can do is to operate the micro-radiator at as low a power as will give us a reasonable signal and keep the power constant.

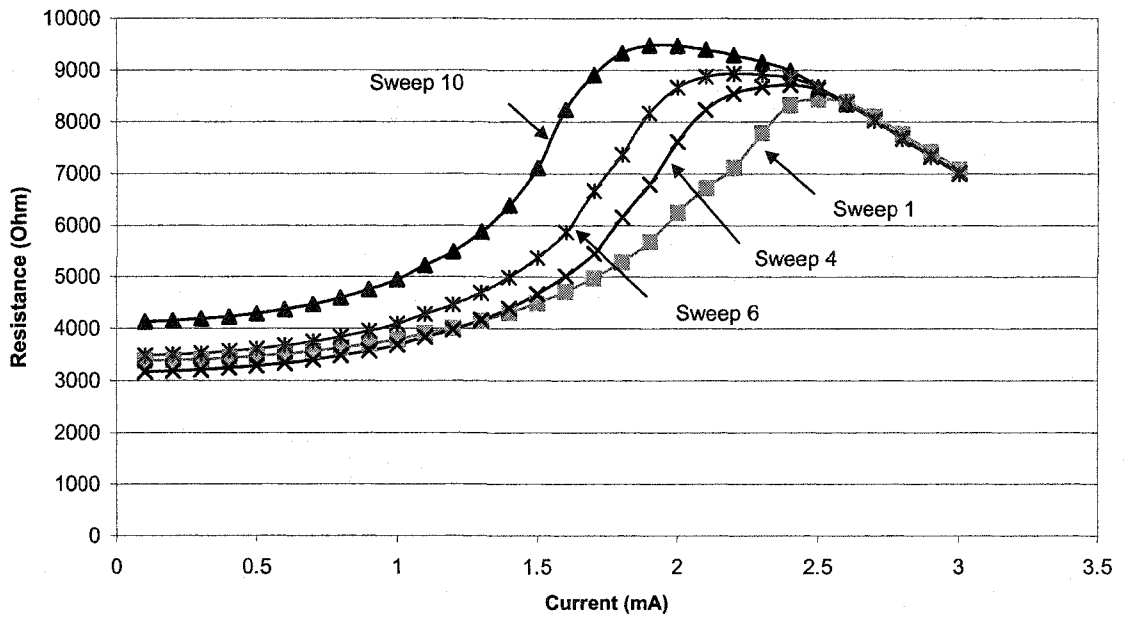


Figure 5.9 (a) Resistance of micro-radiator as a function of input current-from sweep 1,4,6 and 10 of Figure 5.8 (b)

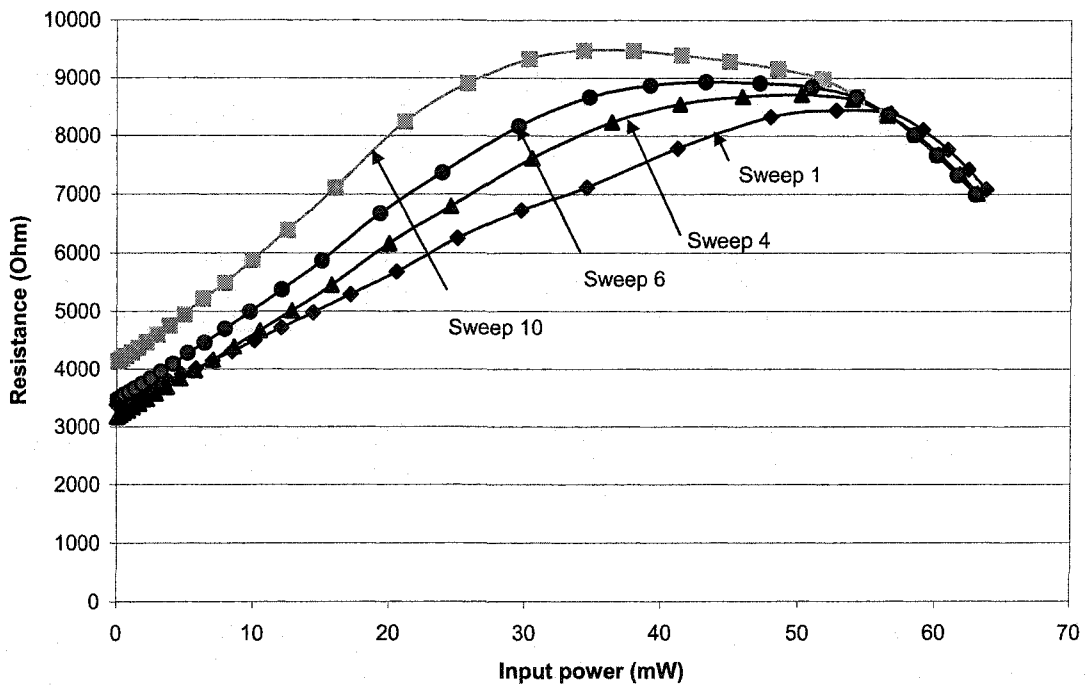


Figure 5.9 (b) Resistance of micro-radiator as a function of input power

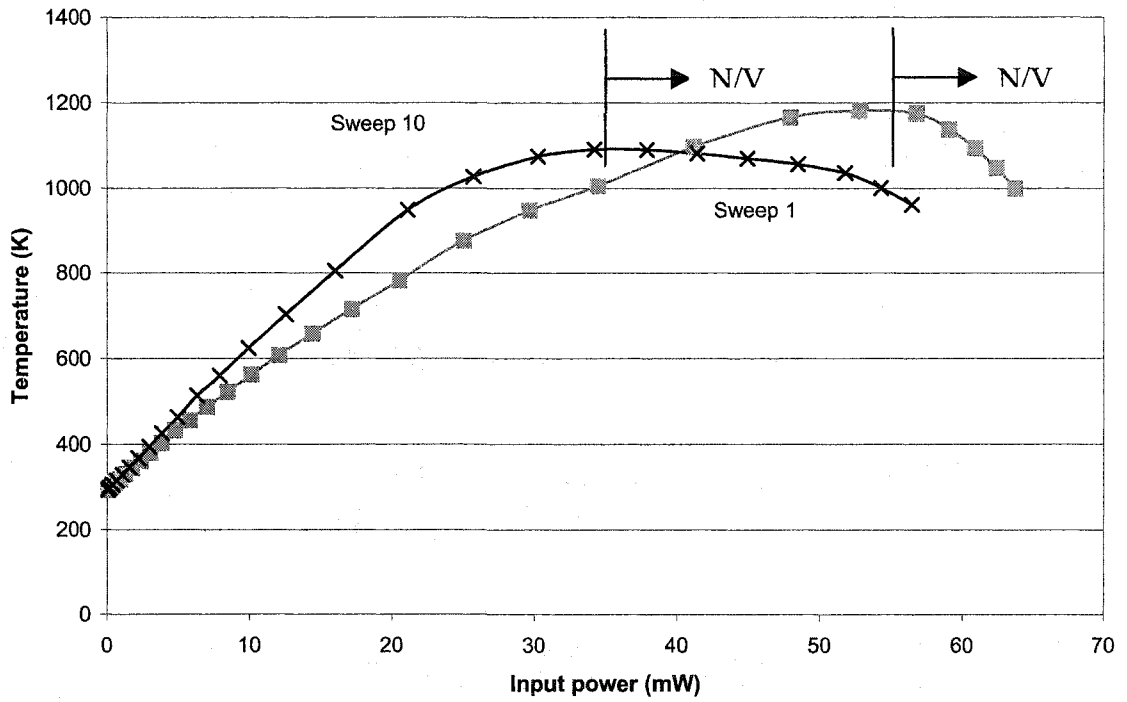


Figure 5.9 (c) Temperature versus input power curves for the first and last sweep  
(N/V: Not Valid)

## References:

- [1] Frank P. Incropera, David P. DeWitt, Introduction to Heat Transfer, John Wiley & Sons, Inc., New York, 1985, p. 610.
- [2] C. H. Mastrangelo, J. H. Yeh, and R. S. Muller, "Electrical and optical characteristics of vacuum-sealed polysilicon microlamps", *IEEE Trans. Electron Devices*, vol. 39, 1992, pp. 1363-1375.
- [3] <http://www.oceanoptics.com/specanim.asp>
- [4] H. O. McMahon, "Thermal radiation from partially transparent reflecting bodies", *Journal of the Optical Society of America*, Vol. 40, No. 6, June 1950, pp. 376-380.
- [5] N. R. Swart and A. Nathan, "Reliability study of polysilicon for microhotplates", *Solid-State Sensor and Actuator Workshop*, Hilton Head, South Carolina, June 13-16, 1994, pp. 119-122.
- [6] H. Akimori, N. Owada, T. Taneoka, and H. Uda, "Reliability study of polycrystalline silicon thin film resistors used in LSI under thermal and electrical stress", *Proc. IEEE Int. Reliability Phys. Symp.*, 1990, pp. 276-280.
- [7] M. Parameswaran, A. M. Robinson, D. L. Blackburn, M. Gaitan, and J. Geist, "Micromachined thermal radiation emitter from a commercial CMOS process", *IEEE Electron Device Letts.*, vol. 12, 1991, pp. 57-59.
- [8] E. I. Cole, Jr., J. S. Suehle, K. A. Peterson, P. Chaparala, A. N. Campbell, E. S. Snyder, and D. G. Pierce, "OBIC analysis of stressed, thermally-isolated polysilicon resistors", *Proc. IEEE Int. Reliability Phys. Symp.*, 1995, pp. 234-243.
- [9] A. M. Robinson, "Mitel 1.5  $\mu\text{m}$  CMOS Process: Characterization Measurements of the Polysilicon Layers for Use in a Micro-sensor", *Canadian Microelectronics Corporation Report*, IC95-06, Kingston, ON, 1995.
- [10] D. W. Greve, "Programming mechanism of polysilicon resistor fuses", *IEEE Trans. Electron Devices*, vol. 29, 1982, pp. 719-724.
- [11] K. Ramkumar and M. Satyam, "Negative-resistance characteristics of polycrystalline silicon resistors", *J. Appl. Phys.*, vol. 62, 1987, p. 174-176.

## Chapter 6

### Vacuum Pressure Sensing and Power-Switching Scheme

The micro-radiator is tested under different pressures in this chapter and a power-switching scheme is introduced to increase the sensitivity of the measurement and lifetime of the device.

#### *6.1 Micro-radiator radiation response with pressure*

Radiation from the micro-radiator has been monitored with a photodetector under different pressures. Figure 6.1 shows the variation of the photodetector signal versus the pressure operating the micro-radiator at a constant power of 10 mW. A piecewise-fitted curve from Excel indicates the first measurement cycle and the data from the following seven cycles are indicated by the corresponding symbols. Each experimental data was taken after the pressure inside the experiment chamber has been stabilized and each pressure measurement cycle took about an hour. The repeatability of the experimental data is good. Figure 6.2 compares the experimental results with the theoretical simulations obtained in Chapter 4 (see Figure 4.14). Experiment and simulation are in reasonable agreement.

The curves shown in Figure 6.1 and Figure 6.2 demonstrate the typical shape for a conventional thermal conductivity pressure gauge [1], but with a much more sensitive output. Above 1000 Pa, the thermal conductivity of the gas is independent of the pressure, and the element temperature and therefore the radiation is almost constant. Below 1 Pa, the radiation is again less dependent on the pressure because heat loss by

conduction through the gas becomes significantly less than the radiation heat loss and conduction heat loss through the support arms, both of which are approximately pressure-independent. In the region between 1 Pa and 1000 Pa, the gas conduction heat loss tends to dominate and the temperature, hence the photodetector signal, is a strong function of the gas pressure. The dynamic range of the output signal in Figure 6.1 varies from 0.2  $\mu\text{A}$  to about 3.4  $\mu\text{A}$  in the pressure range from 1 Pa to about 300 Pa, which corresponds to a change of 16 times the output at 1 Pa, while a standard Pirani gauge and a CMOS Pirani gauge both change only about 3 % in this range [1].

As discussed in Chapter 4, higher input power shifts the micro-radiator emission more into the sensitive range of the photodetector. The response curve shown in Figure 6.1 and 6.2 shifts to a different pressure range in Figure 6.3 when the constant power input is increased to 20 mW.

It should be noted that the constant power delivered to the polysilicon micro-radiator necessary to produce a particular detectable photodetector signal increases as the pressure increases. A power of 5 mW at  $10^{-3}$  Pa increases to about 25 mW at one atmosphere due to the increase of cooling by the surrounding gas. Figure 6.3 shows the photodetector signal versus gas pressure at two different constant powers. The 10 mW curve has a sensitive pressure range from 1 Pa to about  $10^3$  Pa. The 20 mW curve has a sensitive range from one atmosphere ( $\sim 10^5$  Pa) down to about  $10^3$  Pa. Operating the micro-radiator at 20 mW below  $10^3$  Pa reduces the lifetime of the device due to excessive heating. The difference between the experimental data and the analytical simulation is probably due to such factors as the simplification of the thermal model, constant emissivity used and instability of polysilicon under high temperature.



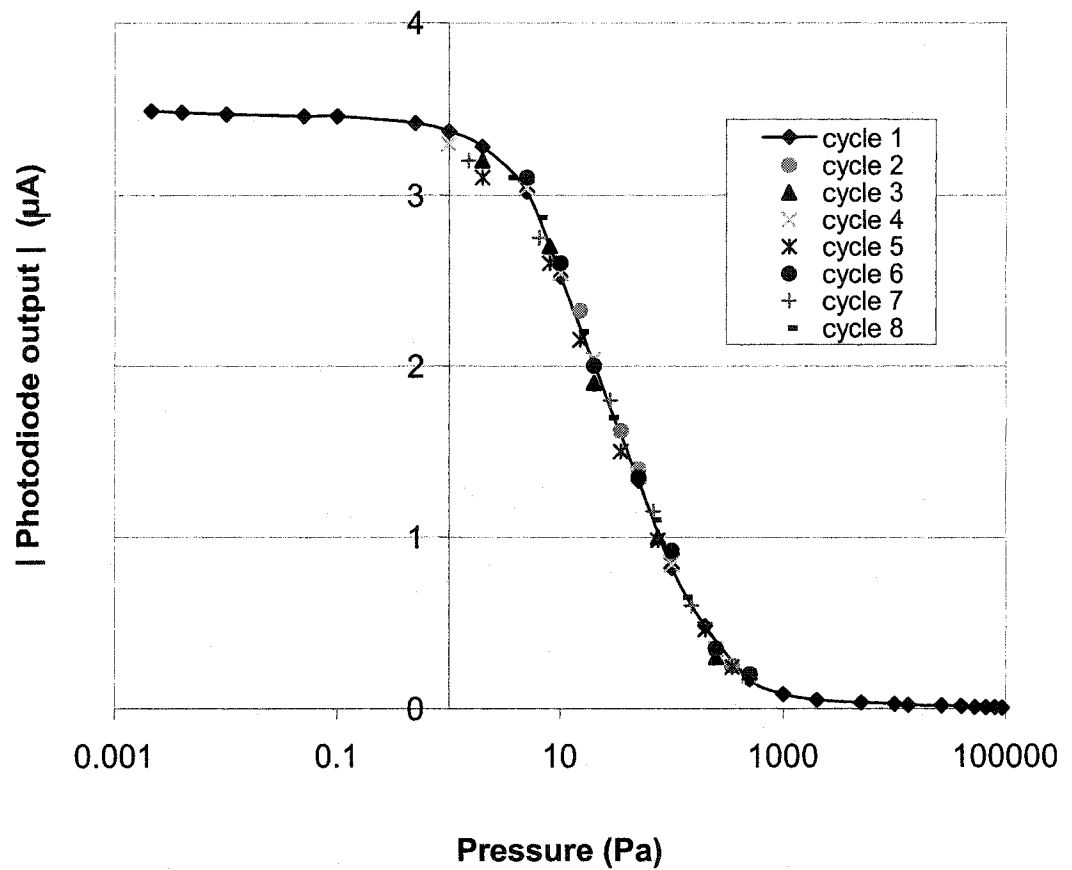


Figure 6.1 Photodetector signal versus pressure operating at a constant power of 10 mW

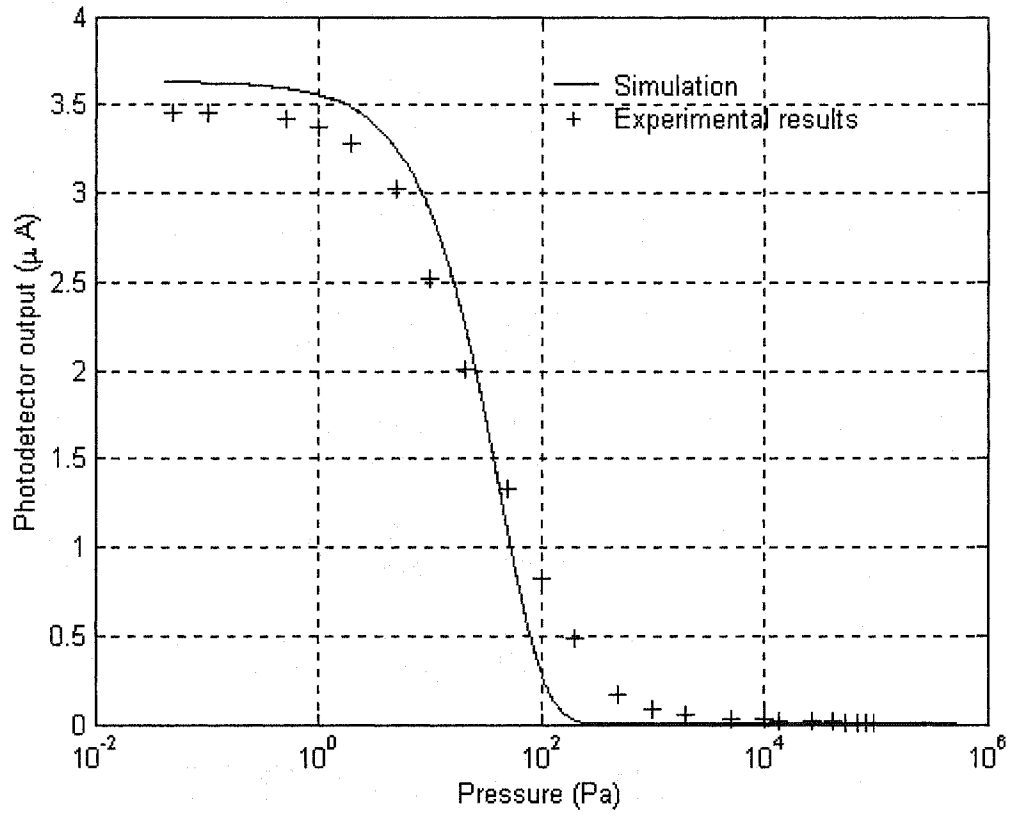


Figure 6.2 Analytical simulation compared with experimental results

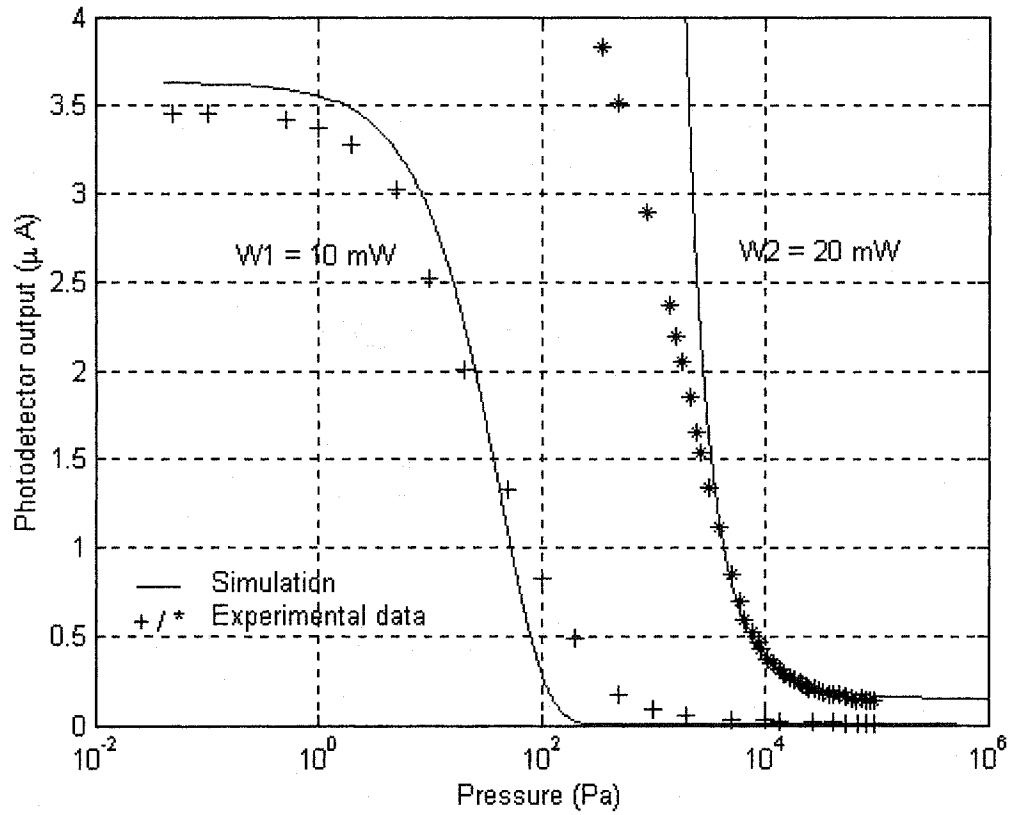


Figure 6.3 Analytical simulation and experimental results showing photodetector signal versus pressure operating at constant powers of 10 and 20 mW

## 6.2 Power-switching scheme

Because polysilicon is electrically unstable at high temperature, as discussed in Chapter 5, and the sensitivity of the photodetector signal varies rapidly with emitter temperature, it is advisable to constrain the photodetector output to a small range at the most sensitive response region and where the temperature is not too high. From Figure 6.3, we can see the sensitivity of the measurement can be increased over a larger pressure range by manipulating the constant power applied to the polysilicon micro-radiator.

The sensitive pressure range can be extended to  $10^{-3}$  Pa by the same mechanism with a different photodetector signal sensitive range. Large numbers of experimental data were not collected in the pressure range around  $10^{-3}$  Pa due to the fact that the overshooting of the constant power system can damage the micro-radiator at that pressure, while it might not be a problem at a higher pressure. An input power of 2 mW at  $10^{-3}$  Pa is enough to provide a sensitive photodetector signal (not included in Figure 6.4). Calibration of the micro-radiator was mainly focused in the pressure range from 0.1 Pa to one atmosphere.

Figure 6.4 shows such a power-switching scheme in the pressure range from about 0.1 Pa to one atmosphere. Seven different levels of constant power of 7 mW, 10 mW, 14 mW, 20 mW, 27 mW, 36 mW and 46 mW were used to achieve a larger dynamic range if the output of the photodetector signal is constrained to vary between  $1 \mu\text{A}$  to  $3 \mu\text{A}$ . The darker vertical straight lines in Figure 6.4 indicate the automatic power switching process.

The conceptual diagram of a possible such power manipulation circuit is shown in Figure 6.5. The photodetector signal is compared to two thresholds *High Threshold* and *Low Threshold* by two comparators *C1* and *C2*. The results from these two comparators are inputs to a JK flip-flop. Table 6.1 shows the truth table of the J-K flip-flop. When the photodetector signal is higher than the *High Threshold*, the output from comparator *C1* sets the JK flip-flop and the output from the flip-flop is sent back to the experimental control system to switch the power input to a lower level. When the photodetector signal is lower than the *Low Threshold*, the output from comparator *C2* resets the JK flip-flop and the output from the flip-flop is sent back to the control system to switch the power

input to a higher level. On each different power level, a different calibration equation is used to output the measured pressure according to the detected photodetector signal.

Table 6.1 J-K flip-flop truth table

J	K	Output Q
0	1	0
1	0	1
0	0	No change
1	1	Toggle

For any point (e.g.  $I_d$  on the 7 mW curve) on the straight-lines plotted in Figure 6.4, we have:

$$y = y_0 + k(x - x_0) \quad (6.2.1)$$

in which  $k$  is the slope of the straight line,  $x_0$ ,  $y_0$ ,  $x$  and  $y$  are as shown in Figure 6.4. Therefore, the photodetector output on the straight-line plots can be represented by:

$$I_d = A + k(\log_{10} p - \log_{10} B) \quad (6.2.2)$$

where  $A$  is the photodetector output at the lower end of the linear output range (ie. 1  $\mu$ A for Figure 6.4),  $B$  is the corresponding pressure at that point and  $p$  is the pressure to be measured. The slope of each curve,  $k$ , can be determined from the pressures at 1  $\mu$ A and 3  $\mu$ A. Table 6.2 lists the values of  $A$ ,  $k$  and  $B$  at each input power level obtained from Figure 6.4.

The relationships between parameters  $k$ ,  $B$  and the power supplied to the micro-radiator are plotted in Figure 6.6 and 6.7 and data are least-square fitted to polynomial curves. Therefore, the parameters  $k$  and  $B$  under an arbitrary power can be obtained and the pressure can be calculated from the photodetector output using equation (6.2.2).

Table 6.2 Parameter table for Figure 6.4

Power (mW)	$A$ ( $\mu\text{A}$ )	$K$	$B$ (Pa)
7	1	-1.45	5
10	1	-1.66	80
14	1	-2.00	800
20	1	-2.74	4300
27	1	-2.95	20000
36	1	-5.03	50000
46	1	-7.83	90000

However, the implementation of the above power-switching scheme can be very time consuming and is not included in this thesis. For each device, a series of calibration measurements operating at different input powers must be performed and the calibrated results have to be pre-programmed into the measurement system.

A simpler approach also based on the power-switching scheme has been designed and implemented. It measures the variation of the power consumption to the micro-radiator, keeping the photodetector signal constant at all pressures. Equation (6.2.2) can be rewritten as:

$$p = B10^{\frac{I_d - A}{k}} \quad (6.2.3)$$

If we keep the photodetector output constant, the pressure versus power consumption curves can be plotted using equation (6.2.3) along with the curve fitting equations of Figure 6.6 and Figure 6.7. The resulted pressure versus power consumption curves are plotted in Figure 6.8. Experiment data directly taken from Figure 6.4 are also plotted in Figure 6.8. The difference between the experimental data and curves plotted using equation (6.2.3) is caused by the curve fitting in Figure 6.6 and 6.7. The least-squares fitting polynomial equations for the experimental data are shown in the figure, but not the curves, for simplicity.

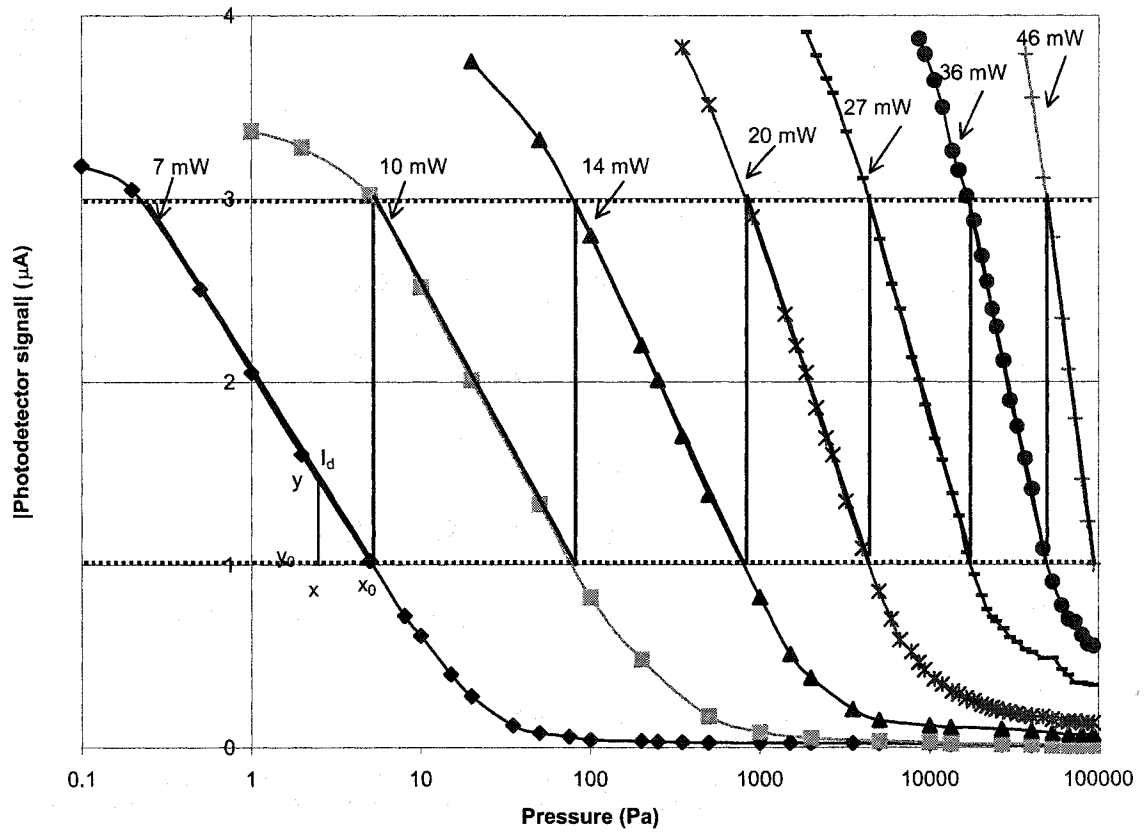


Figure 6.4 Photodetector signal versus pressure operating at different constant powers showing power-switching scheme

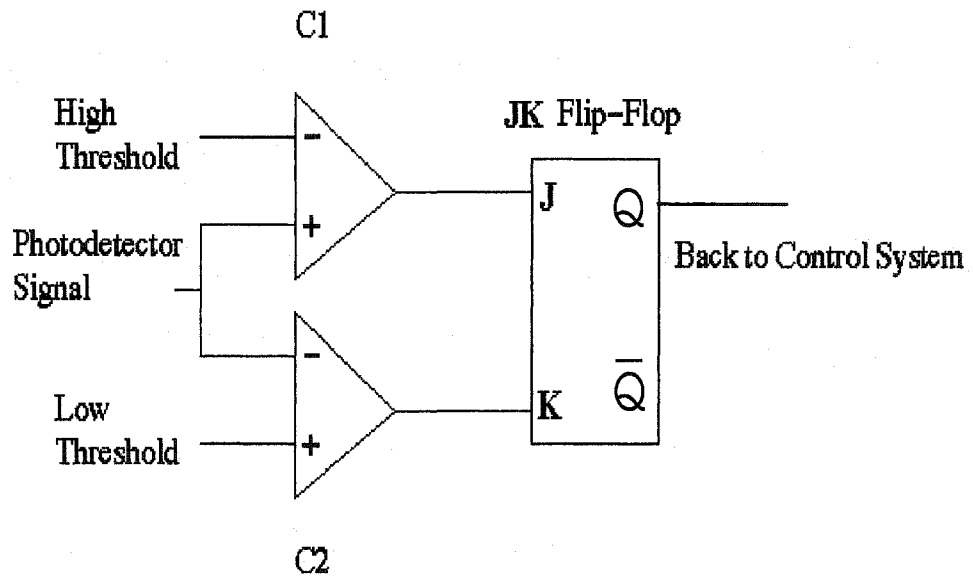


Figure 6.5 Conceptual diagram of power-switching scheme

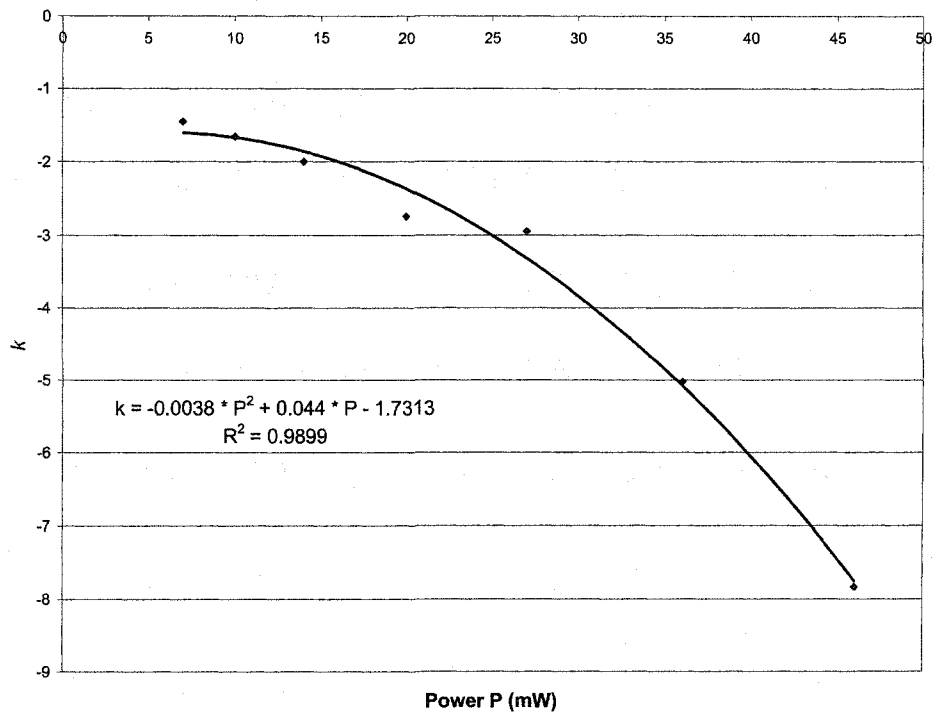


Figure 6.6 Relationship between parameter  $k$  and the applied power



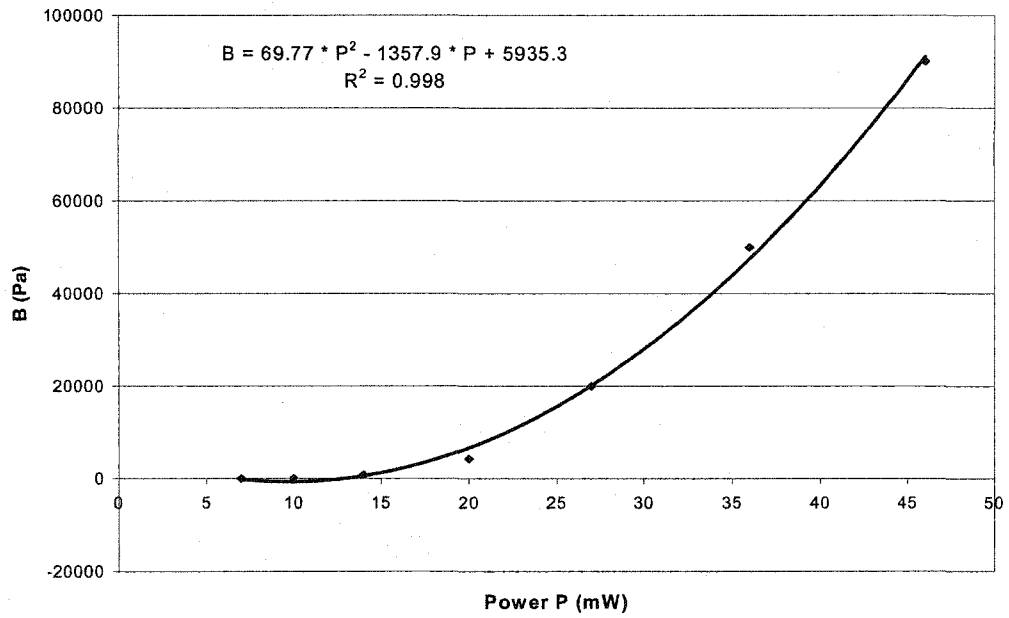


Figure 6.7 Relationship between parameter B and the applied power

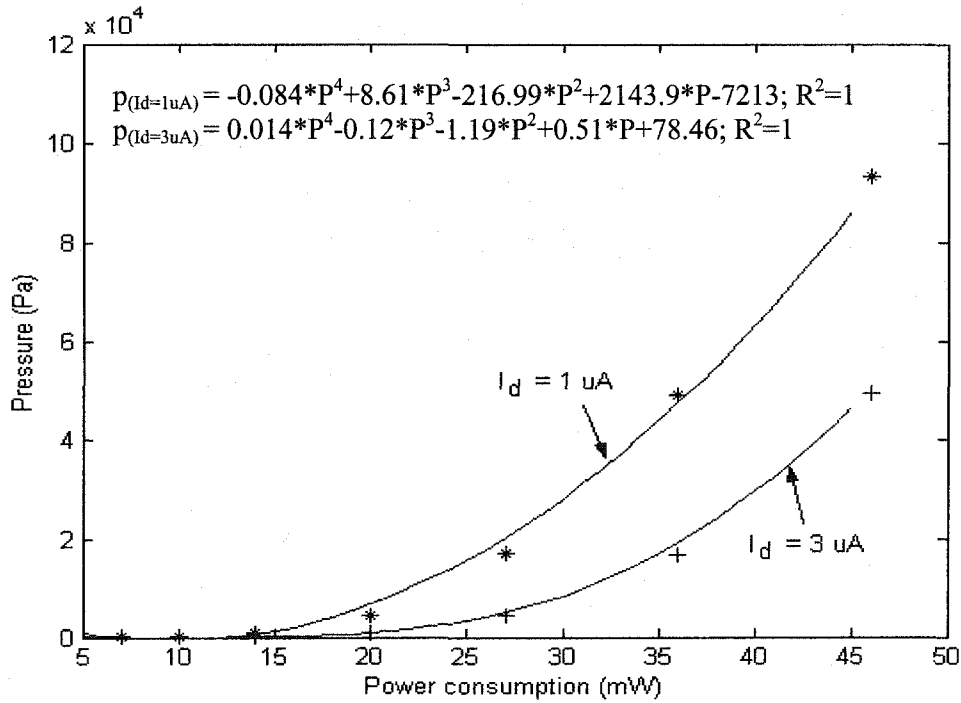


Figure 6.8 Power consumption of the micro-radiator versus the pressure with constant photodetector output of  $1 \mu A$  or  $3 \mu A$ . The plotted curves are derived from equation (6.2.3); the least-squares polynomial equations fitted to the experimental data are not plotted.

Compared with the power-switching measurement shown in Figure 6.4, this approach has the advantage of ease of implementation, but the minimum pressure variation it can measure is limited by the output of the constant power supply. Since the minimum output of the constant power supply is about  $10^{-3}$  mW and  $dp/dP$  of the curves in Figure 6.8 varies from 10 to  $10^5$ , the minimum pressure variation that can be measured is about  $10^{-2}$  Pa at low pressure and about  $10^2$  Pa at high pressure. The minimum pressure variation that can be measured in Figure 6.4 is about  $10^{-5}$  Pa at low pressure and  $10^{-1}$  Pa at high pressure due to the high sensitivity of the photodetector.

### **6.3 Calibration by comparison**

If the vacuum gauge is calibrated by comparing its reading to the pressure indicated by a so-called reference gauge (secondary standard), it is called *calibration by comparison* [3]. In this section, the micro-radiator pressure sensor is calibrated and tested using this method.

#### **6.3.1 Calibration curves**

For a micro-radiator fabricated with a different process run, slightly different characteristics have been observed. The calibration curve is shown in Figure 6.9 (a) and (b). A smaller vacuum chamber originally designed for XeF<sub>2</sub> etching is used as the experimental chamber. Details of the etching vacuum system can be found in reference [2].

It is difficult to find a close polynomial to fit all experiment data, so the curve was divided into two parts and separately fitted into polynomial curves as shown in Figure 6.9 (a) and (b).

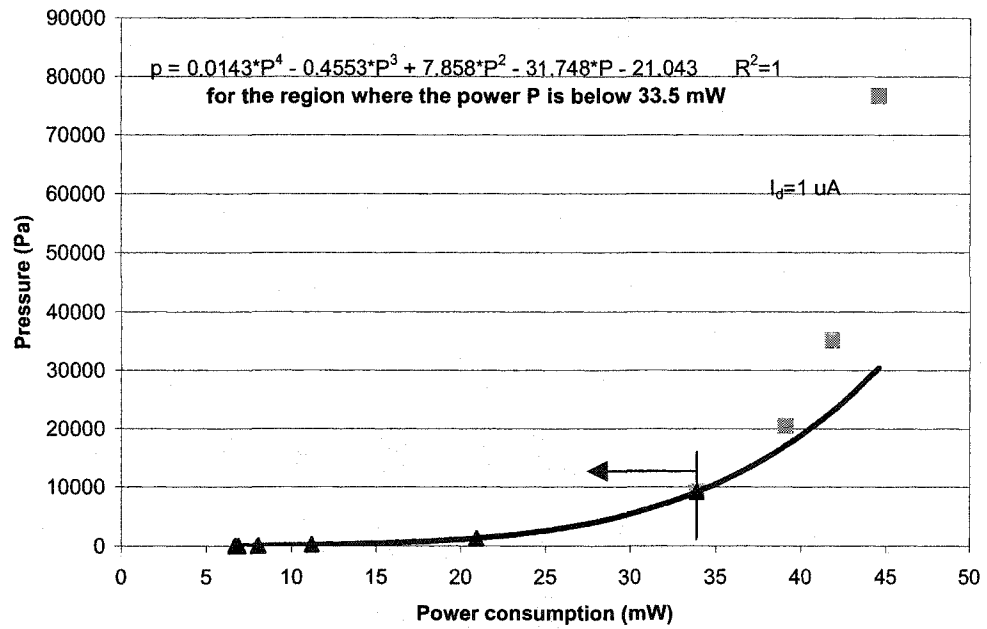


Figure 6.9 (a) A typical calibration curve with data below 33.5 mW being fitted onto a polynomial curve

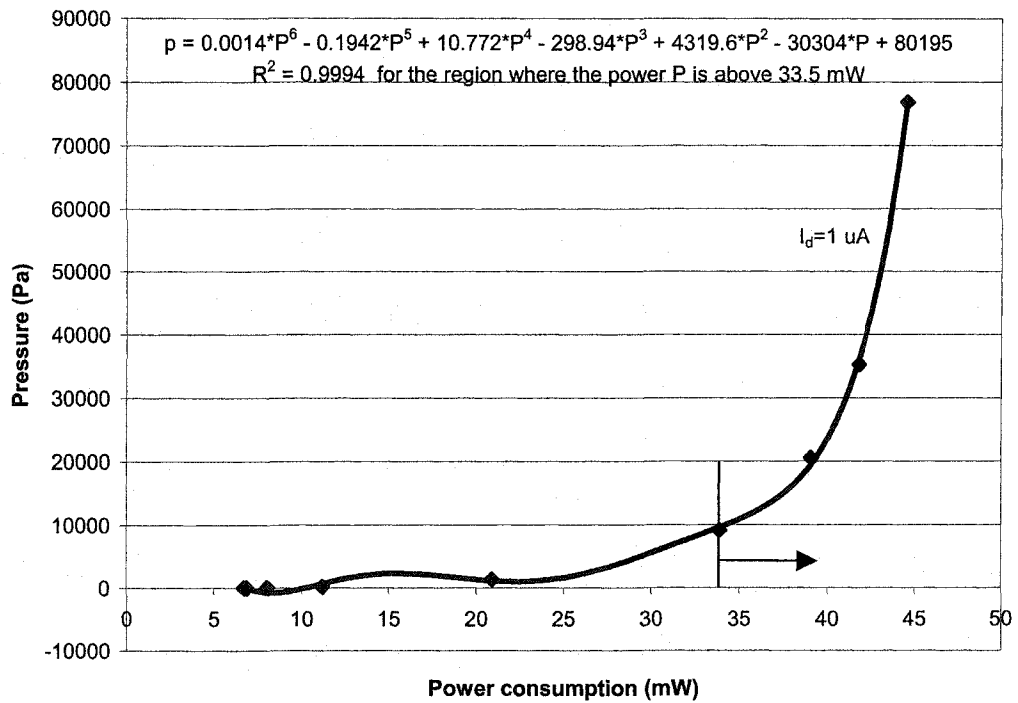


Figure 6.9 (b) A typical calibration curve with data above 33.5 mW being fitted onto a polynomial curve

### 6.3.2 System automation

The pressure measurement system using the power variation method above is automated using a program written in Instrument Basic. The flow chart of the program is shown in Figure 6.10.

At the beginning of the program, the user can choose a constant photodetector signal to perform the pressure measurement if multiple calibration curves are available. The program first sets up the Source Measure Unit (SMU) and Digital Multi-Meter (DMM) and measures the room temperature resistance of the micro-radiator by outputting a 0.1 mA current into the micro-radiator and measuring the corresponding voltage across it. A small initial input power is then used to determine an initial current to the micro-radiator; the corresponding radiation is measured and compared to the predefined constant value. If the absolute value of the difference between the measured signal and the predefined constant value is larger than  $\Delta I_d$ , the input current to the micro-radiator is increased or decreased correspondingly by a small step value  $\Delta I$  and the updated radiation signal is measured again and compared with the predefined constant value again. The loop continues until the difference between the measured photodetector signal and the predefined constant value is smaller than a tolerance value  $\Delta I_d$  (e.g. 0.05  $\mu\text{A}$ ), the power consumed by the micro-radiator is calculated and the corresponding pressure is then calculated by the pressure ( $p$ ) - power ( $P$ ) calibration curve.

The time each measurement takes depends on the pressure, predefined initial power and the tolerance value  $\Delta I_d$ . Optimization has been made in the program to vary the current step value according to the difference between the photodetector signal and predefined value. When the difference is big, a larger step current  $\Delta I$  is used to increase or decrease the radiation. Otherwise a smaller step current is used.

A sample code can be found in Appendix C.

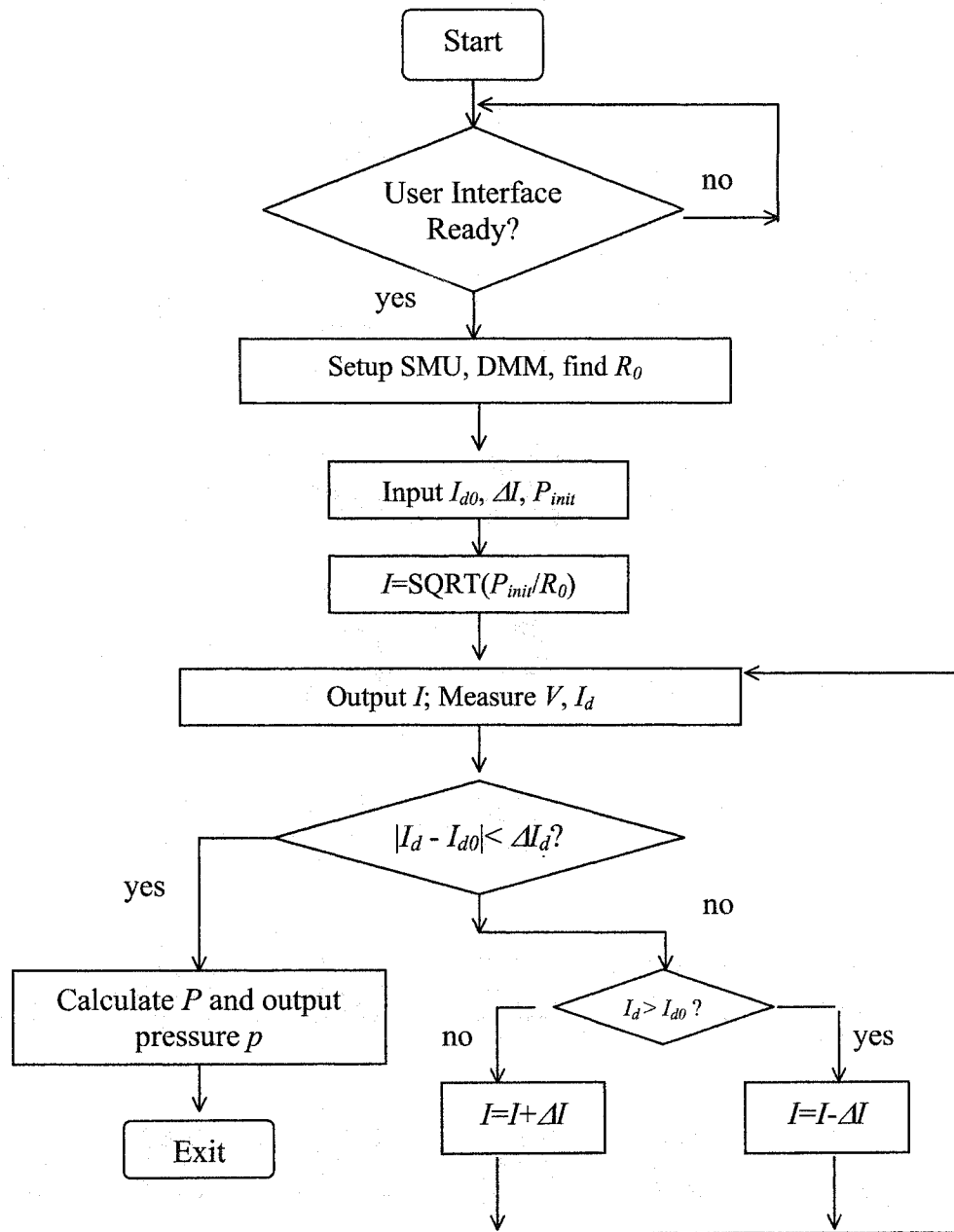


Figure 6.10 Flow-chart of the pressure measurement system

### 6.3.3 Test results

The automated measurement system has been tested for a series of devices at a constant photodetector output of 1  $\mu$ A. Table 6.3 shows the typical results for a pressure measurement using a calibration curve obtained from the same device. The reference gauges are two Wallace & Tiernan diaphragm manometers (2667 - 9333 Pa, 67 - 2667 Pa).

Table 6.3 Typical measurement results using calibration curve obtained from same device

Reference gauge (Pa)	Micro-radiator output (Pa)	Difference (%)
146.65	151.98	3.5
182.65	182.65	0
399.96	414.63	3.5
6532.68	6132.72	6.5
21997.80	23331.00	5.7
49595.04	50261.64	1.3
74125.92	80525.28	7.9
93057.36	85991.40	8.2

From Table 6.3, we can see the difference between the micro-radiator measurement and the reference gauge is 8.2 % or less. Differences are caused by the curve fitting equations, and tolerance value defined in the program. It will be improved if a smaller tolerance value is used, but the computation time will be longer.

If a typical calibration curve is used, test results on different devices generate a difference as high as 35%. Therefore, for each micro-radiator vacuum sensor, a calibration test before using it as pressure sensor is necessary. The calibration curve may change over time; therefore, a calibration test should be done periodically.

### 6.3.4 Factors that affect the calibration

There are many factors that affect the calibration of the micro-radiator pressure sensor. Here we discuss several important factors that should be taken into account for the device calibration.

1. Distance between micro-radiator and photodetector:

The distance between the micro-radiator and photodetector will affect the magnitude of photodetector output. All of the experimental data in the previous sections were obtained using a default distance of 2.5 cm. Figure 6.11 shows the photodetector output versus pressure for two different distances, 1 cm and 3 cm. Input power to the micro-radiator is 20 mW. From Figure 6.11 we can see the shorter the distance, the stronger the photodetector signal because the proportionality constant  $k$  in equation (4.4.1) is bigger for a shorter distance. Both the intensity of the radiation from the micro-radiator and the solid angle from the micro-radiator to the photodetector are bigger with a shorter distance.

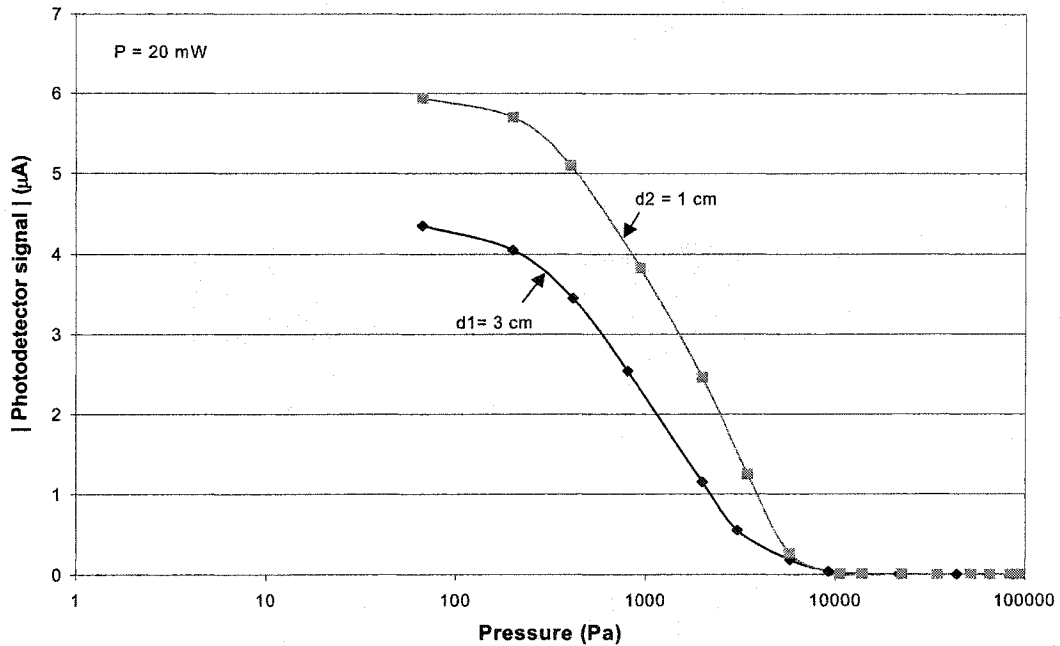


Figure 6.11 Photodetector signal versus pressure with different distance between micro-radiator and photodetector

## 2. Ambient temperature:

From the theoretical calculation in Chapter 4, we can see the temperature of the ambient gas and substrate is an important factor in calculating the micro-radiator equilibrium temperature. The conventional Pirani gauge shows a degree change in gauge-wall temperature can cause up to 20% change in gauge readings [3]. The effect of the ambient temperature on the micro-radiator sensing results was not investigated in this project. Due to the high operating temperature of the micro-radiator, the effect of the ambient temperature is minimized.

## 3. Accommodation coefficient $\alpha$

The accommodation coefficient introduced in Chapter 3 depends on the surface condition of the micro-radiator. There may be an increase of  $\alpha$  by as much as a factor of 10 when a 'clean' surface becomes contaminated with an adsorbed layer of gas molecules [4]. Therefore, the micro-radiator should be recalibrated periodically to increase the accuracy of measurement. The recalibration can be done easily with a reference gauge and the automated pressure measurement system program listed in Appendix C.

## 4. Ambient gas

Different gases have different thermal conductivities at different pressures. Thus the calibration of the micro-radiator is gas dependent. The micro-radiator needs recalibration if a gas other than air is measured. An example of the radiation signal from the incandescent micro-resistor is shown in Fig. 6.12, for two different gases, He and air. The photodetector output versus the pressure curve shifts to the left when the ambient gas is changed from air to He. This feature may be used to analyze the ambient gas change. It should be noted that the reference gauge is also gas dependent. Thus the pressure indicated in Figure 6.12 is not accurate for He.



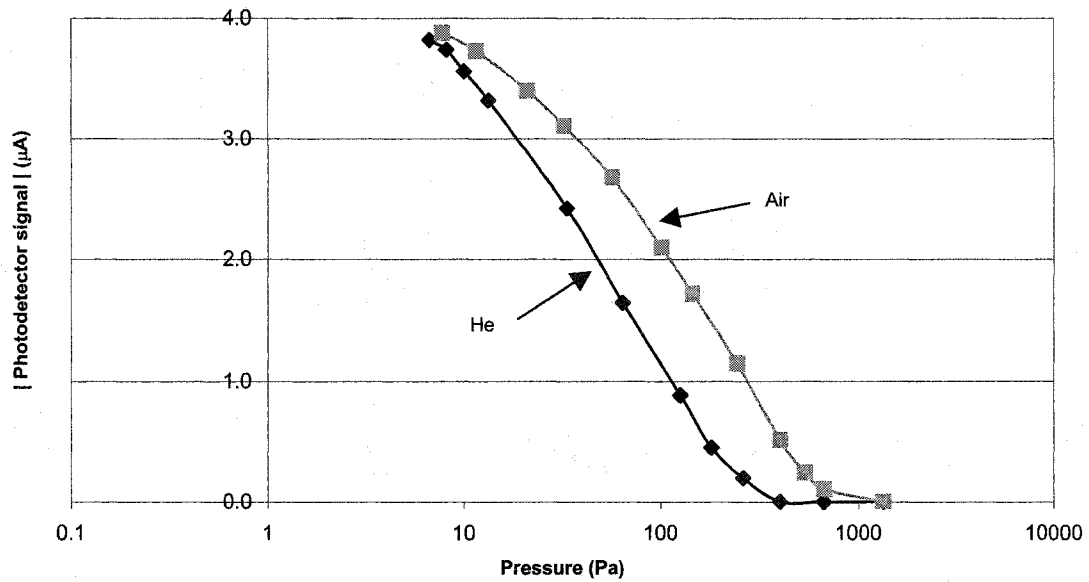


Figure 6.12. Photodetector outputs for air and He

### References:

- [1] W. Allegretto, B. Shen, P. Haswell, Z. Lai, and A. M. Robinson, "Numerical Modeling of a Micromachined Thermal Conductivity Gas Pressure Sensor", IEEE Transactions on Computer-aided Design of Integrated Circuits and Systems, Vol. 13, No. 10, October, 1994, pp. 1247-1256.
- [2] K. Brown, EE 641 Project report, Department of Electrical and Computer Engineering, University of Alberta, 1999.
- [3] J. M. Lafferty, Foundations of Vacuum Science and Technology, John Wiley & Sons, Inc., New York, 1998, p. 673.
- [4] J. H. Leck, Pressure Measurement in Vacuum Systems, Chapman and Hall Ltd., London, 1957, p. 76.

## Chapter 7

### CMOS Photodetector Design

We have demonstrated in the previous chapters that measuring the radiation from a micro-radiator is an effective way of measuring gas pressure. In terms of packaging such a device, integrating the photodiode with the emitter chip would be an advantage. First, it integrates the emitter and the detector into a single unit. Second, the distance between the emitter and the photodetector can be reduced to about 100 micron or less. Therefore, the photodetector output signal will increase. In addition, the decreased distance between the emitter and the photodetector will shift the sensitive range to a higher pressure.

A P-N junction diode and a bipolar transistor are two of the most commonly used photodetector configurations and they are natural elements in a standard CMOS process. We have designed and tested a three-mode CMOS photodetector for this purpose. Integration of the photodetector with the micro-radiator is achieved using an assembly approach and a flip-chip integration approach is discussed as future work of the project.

#### ***7.1 P-N junction and photodiode***

The P-N junction is one of the most important junctions in solid-state electronics. It refers to the change from N-type material, which means the majority charge carriers are electrons, to P-type material, which has holes as the majority charge carriers, within a single crystal.

Adding impurities can change the majority charge carriers of the material. The added impurity is called dopant. For example, when an atom containing five outer-shell electrons, such as arsenic, is added to a semiconductor, four of them participate in the

covalent bonds and one electron is left over. This extra electron is nearly free and has an energy level that lies within the energy gap, just below the conduction band. Such a pentavalent atom in effect donates an electron to the structure and, hence, is referred as donor. If the semiconductor is doped with atoms containing three outer-shell electrons, such as indium and aluminum, the three form covalent bonds with neighboring atoms, leaving an electron deficiency, or hole, in the fourth bond. The energy levels of such impurities also lie within the energy gap, this time just above the valence band. Electrons from the valence band have enough thermal energy at room temperature to fill these impurity levels, leaving behind a hole in valence band. Because a trivalent atom in effect accepts an electron from the valence band, such impurities are referred to as acceptors.

The P-N junction can be realized by either changing the dopant from donors to acceptors during the growth of the crystal or by introducing impurities of one type into regions of a crystal that was grown with lighter doping of the opposite type [1]. The fabrication techniques used to form P- and N-type regions involve i) epitaxial procedures where the dopant species are simply switched at a particular instant in time; ii) ion-implantation in which the dopant ions are implanted at high energies into semiconductor; iii) diffusion of dopants into an oppositely doped semiconductor.

Figure 7.1 gives the schematic view of a P-N junction and various current and particle flow components in the P-N diode at equilibrium. The P-type region at the far left and the N-type region at the far right in Figure 7.1 (a) are neutral. The density of the acceptors at the P-type region and the density of the donors at the n-type region exactly balance the densities of holes and electrons correspondingly. In the middle region, where P-type and N-type materials meet, an electric field exists. This region is called the depletion region and extends a distance  $X_p$  in the p-region and a distance  $X_n$  in the N-region. Any electrons or holes in the depletion region are swept away by the electric field present. Thus a drift current exists which counterbalances the diffusion current that arises because of the difference in electron and hole densities across the junction. The directions of the four components of particle flow within the transition region and the resulting current directions are shown in Figure 7.1 (b).

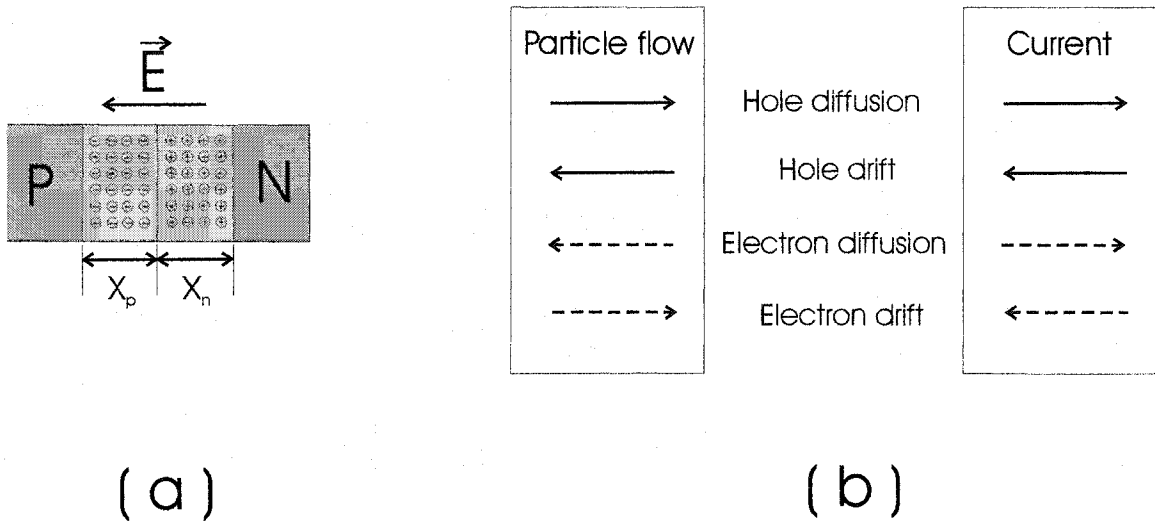


Figure 7.1 (a) An idealized model of the P-N junction without bias showing the neutral and the depletion areas. (b) A schematic showing various current and particle flow components in the P-N diode at equilibrium

A P-N junction is also called a diode and the junction device designed to respond to photon absorption is called a photodiode. When a voltage is applied to the P-N junction as shown in Figure 7.2 (a), the excess carriers generated by the incident photons are collected to form a photocurrent  $I_{op}$ . If the junction is uniformly illuminated by photons with energy  $h\nu$  larger than the energy band gap of the material  $E_g$  and assuming the excess carriers are generated at a rate  $g_{op}$  (electron-hole pair/cm<sup>3</sup>-s), the resulting current due to collection of the optically generated carriers by the junction can be calculated by

$$I_{op} = qAg_{op}(L_p + L_n + W) \quad (7.1)$$

in which  $q$  is the electrical charge;  $A$  is the diode cross-sectional area and we assume a uniform generation rate in the diode;  $L_p$  and  $L_n$  are the diffusion length of hole and electron respectively; and  $W$  is the width of the depletion region. Diffusion length is the average distance where the hole or electron can be found from the point where they were generated.

Figure 7.2 (b) shows the symbol of a diode and Figure 7.2 (c) the I-V characteristics of an illuminated junction. The current due to optical generation is negative and proportional to  $g_{op}$  when the junction is reverse biased. Since  $g_{op}$  is linearly proportional to the intensity of incident light at a given wavelength in the low intensity regime, the optically generated current is linearly proportional to the intensity of incident light. When the intensity of incident light is extremely high, the optically generated current becomes saturated. The saturation point of the linear response depends on the reverse voltage applied to the P-N junction. The saturation points are not indicated in Figure 7.2 (c).

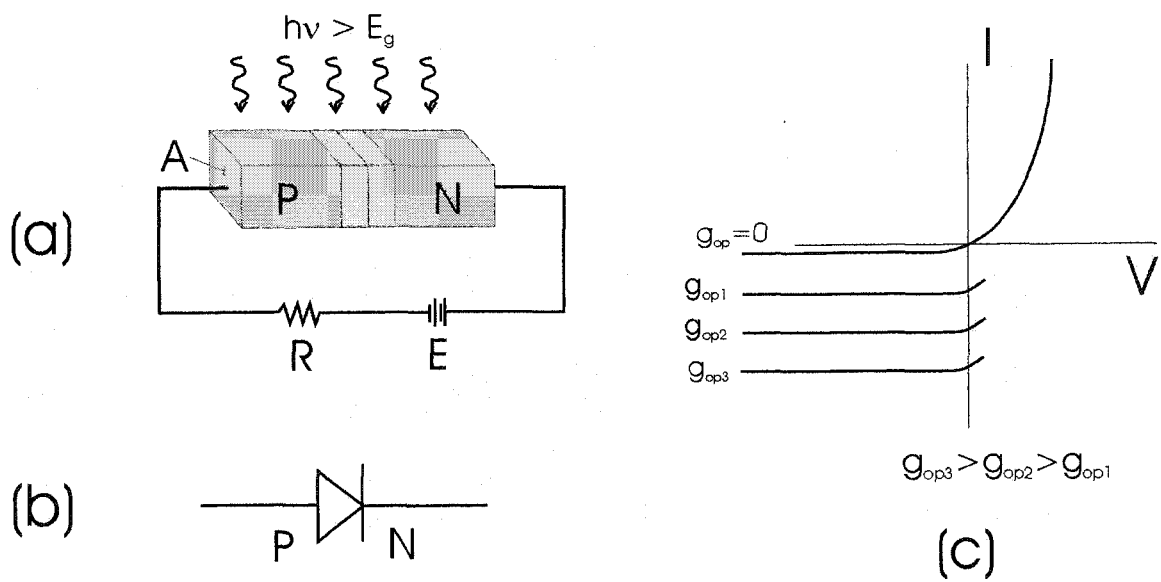


Figure 7.2 (a) Optical generation of carriers in a P-N junction; (b) P-N junction symbol; (c) I-V characteristics of an illuminated junction

## 7.2 Phototransistor

A bipolar device refers to a device where the action of both electrons and holes is important. When two back-to-back P-N diodes are connected together, a bipolar junction transistor (BJT, either N-P-N or P-N-P) is formed. Figure 7.3 shows an N-P-N transistor, which has an emitter, a base and a collector. The  $n^+$  region, which serves as the source of injected electrons, is called the emitter, and the N region into which the electrons are swept by the reverse-biased junction is called the collector. The center P region is called the base. When the emitter base junction (EBJ) is forward biased and the base-collector junction (BCJ) is reversed biased, the BJT produces a high current gain.

A number of currents can be identified in the BJT, as shown in Figure 7.3. The first one is from the injected electrons lost to recombination in the base, and the second one is due to the electrons reaching the reverse-biased collector junction. The third one is produced by the thermally generated electrons and holes making up the reverse saturation current of the collector junction and the fourth one is from the holes supplied by the base contact for recombination with electrons. The last one is due to holes injected across the forward biased emitter junction.

The phototransistor is a bipolar transistor used for optical detection. The base current of a phototransistor is not provided by an external supply (often there is no base contact on the phototransistor), but through optical generation. Light shining on the device creates electron-hole pairs. These pairs are generated throughout the device. The phototransistor provides higher gain than the photodiode due to the transistor action.

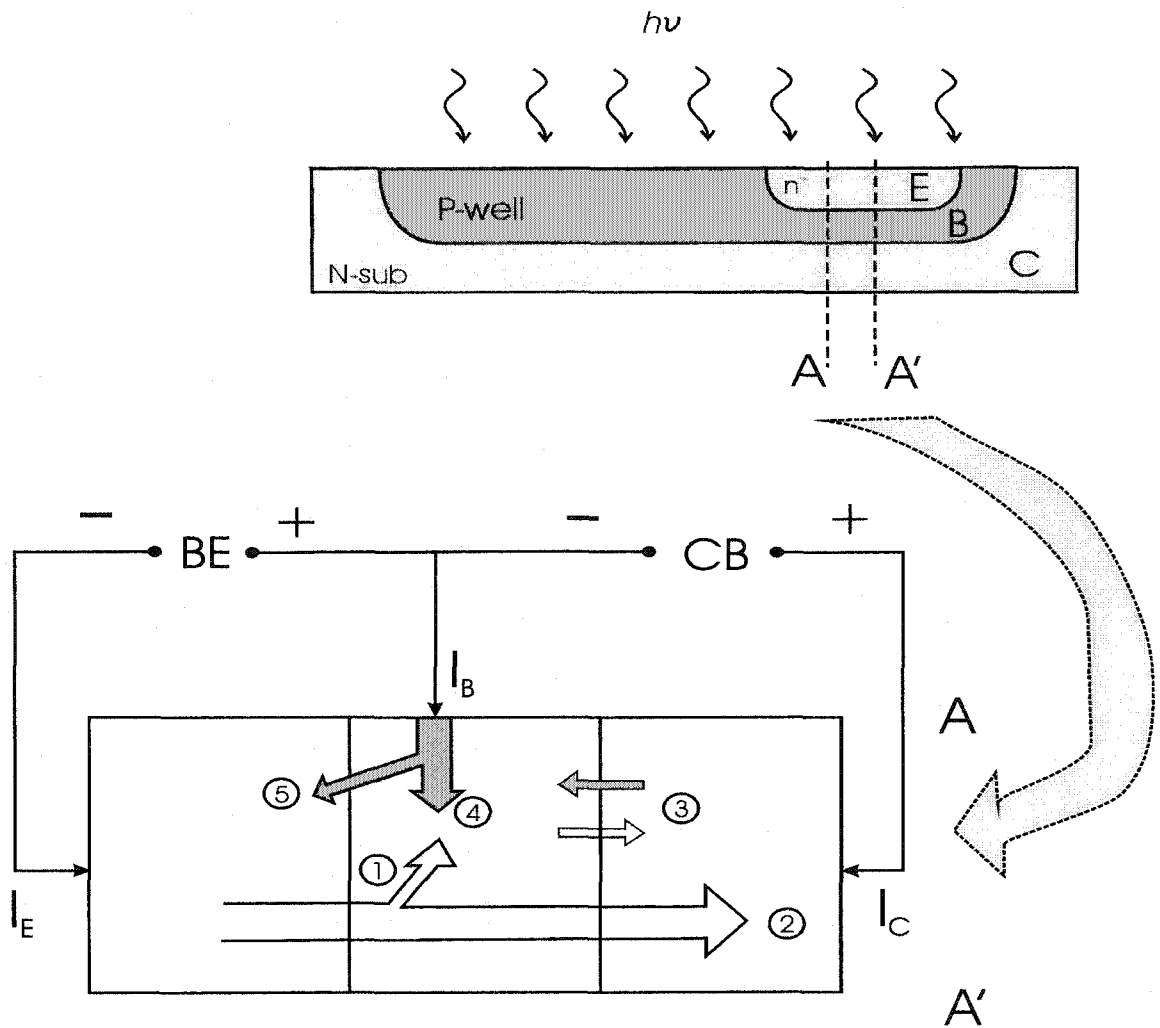


Figure 7.3 Schematic of an N-P-N transistor showing hole and electron flow:  
 (1) injected electrons lost to recombination in the base; (2) electrons reaching the reverse biased collector junction; (3) thermally generated electron-hole pairs making up the reverse saturation current of the collector junction; (4) holes supplied by the base contact for recombination with electrons; (5) holes injected across the forward biased emitter junction.



### 7.3 Three-mode CMOS photodetector design

The sensitivity of a photodiode as introduced in section 7.1 can only be changed by the applied voltage across the diode and the photodiode output can be saturated when the intensity of incident light is high enough [2]. Therefore, this amount of controllability is not enough for practical applications. Ward-Syrzycki's multi-sensitivity photodetector [3] is designed here and fabricated with the CMOS IC process for integration of the micro-radiator pressure sensing system.

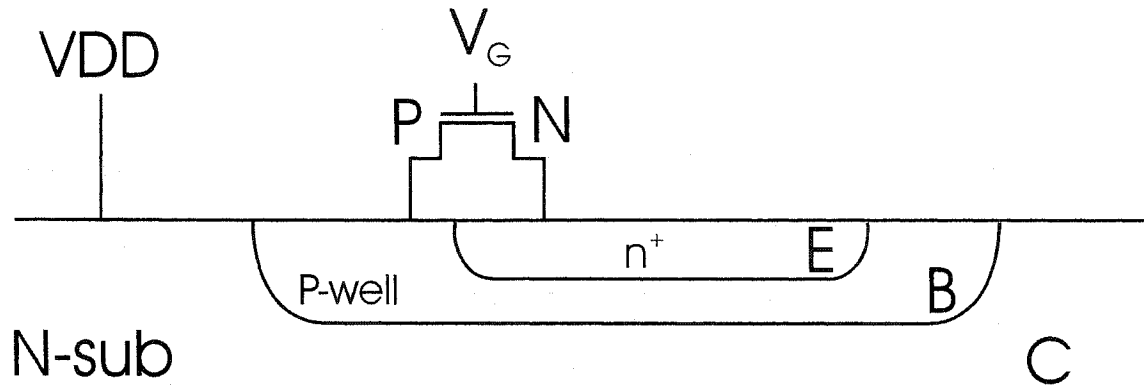
The detector features three modes of operation corresponding to different light intensities. Figure 7.4 (a) shows the design of a vertical N-P-N transistor that can be used in two different operating modes with a Metal Oxide Semiconductor Field Effect Transistor (MOSFET) attached.

The MOSFET is placed across the base-emitter junction of the vertical n-p-n phototransistor; it is used to force the device into one of two modes. The equivalent circuits of two operating modes are shown in Figure 7.4 (b). In the diode mode, the MOSFET is turned on and permits the substrate-to-p-well photocurrent to flow directly to the  $n^+$  emitter, and no transistor action occurs. The resulting structure is like a reverse biased substrate-to-p-well junction as introduced in Section 7.1. When the MOSFET is turned off, electrons generated by photons in the p-well add to the base current of the vertical transistor and is then amplified by the forward current gain of the device. The resulting structure is like the one shown in Figure 7.3.

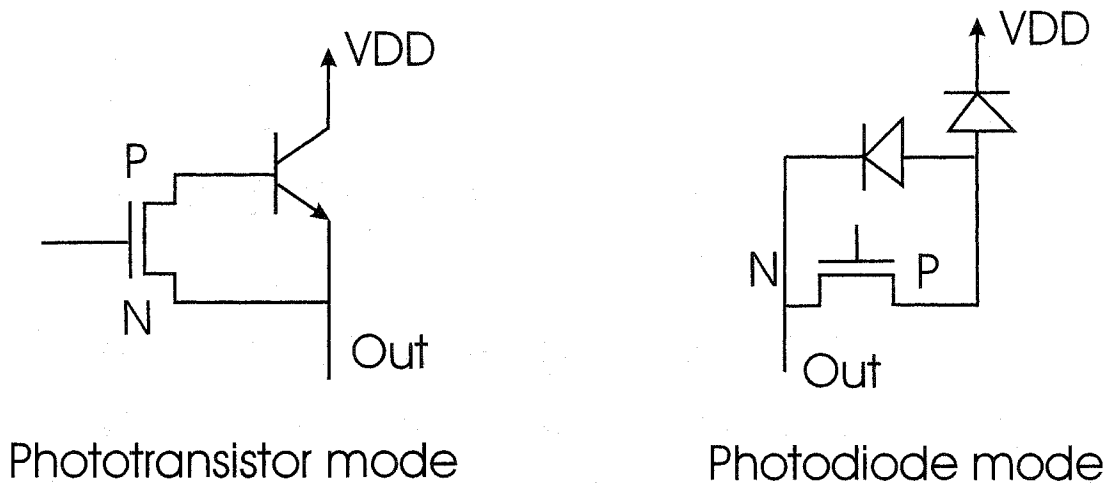
The third mode of the photodetector can be obtained by connecting two vertical transistors in a Darlington connection. A second transistor then amplifies the output current from the first phototransistor.

A photodetector with all of three operational modes can be implemented using two MOSFETs as shown in Figure 7.5. Figure 7.5 (a) shows the structure and Figure 7.5 (b) shows the equivalent circuit of the three-mode photodetector design. The two gate inputs *Sel 1* and *Sel 2* can be set in any of four combinations, each resulting in a different mode of operation. Table 7.1 shows the function table of the designed photodetector. When *Sel 1* is high and *Sel 2* is low, the circuit is equivalent to a reverse-biased photodiode with the

output signal amplified by a transistor, and it is not defined as a separate operating mode here.



(a)



(b)

Figure 7.4 Structure and equivalent circuits of the CMOS multi-mode photodetector

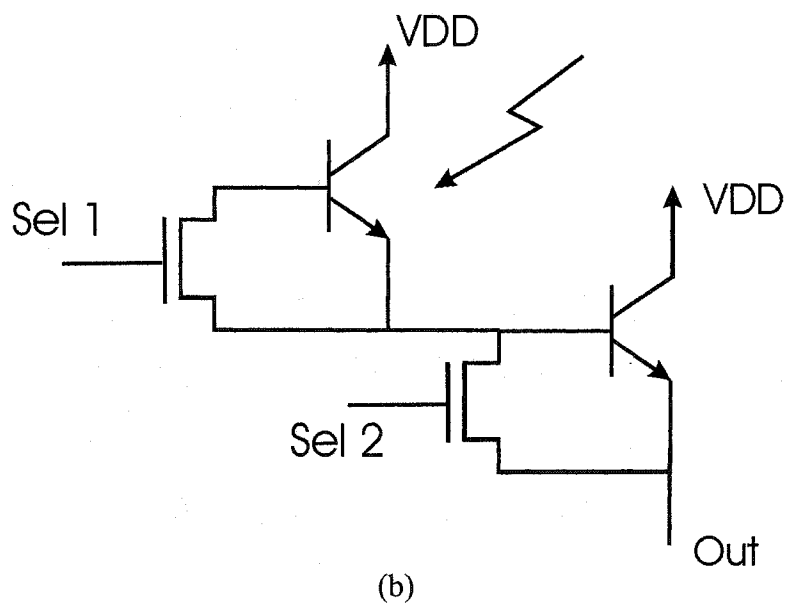
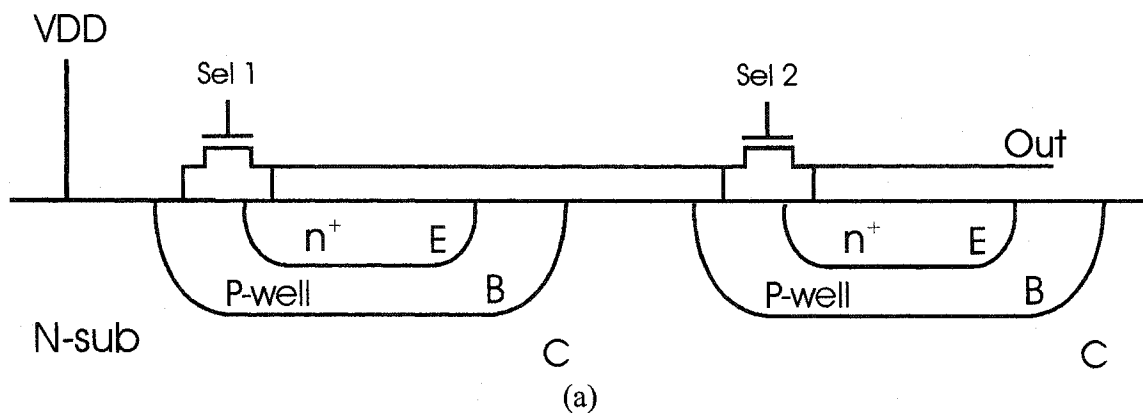
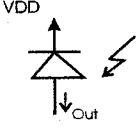
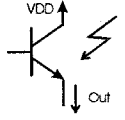
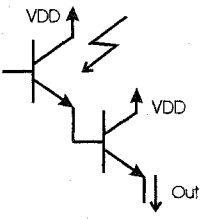
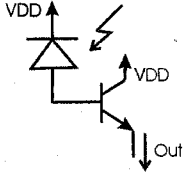


Figure 7.5 Structure and equivalent circuit of the three-mode photodetector

Table 7.1 Function table of three-mode photodetector

Sel 1	Sel 2	Equivalent Circuit	Working Mode
1	1		Photodiode
0	1		Phototransistor
0	0		Darlington connection
1	0		Photodiode with transistor amplifier

## **7.4 Test of three-mode CMOS photodetector**

The three-mode CMOS photodetector was tested using a point source, a 4.2 mW adjustable focus laser diode (Thorlabs Model S1021), and a micro-radiator. The results of the tests are described in this section.

### **7.4.1 Test with a point light source**

The light source introduced in Chapter 4 has been shown to behave as a point source of light. It is now used to test the photodetector working in the photodiode mode and phototransistor mode. Figure 7.6 (a) and (b) show the output of the photodetector versus the inverse distance squared between the photodetector and light point source. Experiment data were least-squares fitted into straight lines, which means the photodetector output is linear to the intensity of incidence light and is a reliable detector to measure the radiation from the micro-radiator in the signal range covered by this test. The output of the photodetector working in the phototransistor mode is about two orders of magnitude higher than the one working at photodiode mode. This is due to the light falling on the photodiode changing the base current of the transistor, causing the collector current to be amplified.

### **7.4.2 Test with a laser diode**

The wavelength of the laser diode is 670 nm. A series of plastic films with identical thickness were used as the intensity attenuator. Different attenuation was achieved by using a different number of films between the laser diode and the photodetector. A Newport 840 optical power meter was used to measure the light intensity. Output signal from the photodetector was amplified by a large dynamic range current amplifier fabricated by Melles Griot (model 13 AMP 003) and the amplified signal was measured with a digital multi-meter.

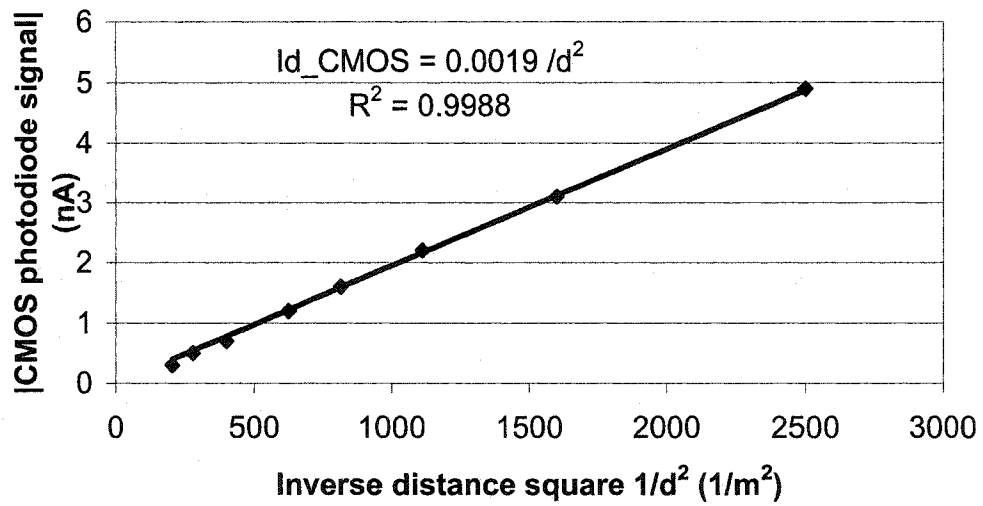


Figure 7.6 (a) Output of photodetector working in photodiode mode versus inverse distance squared of the light source

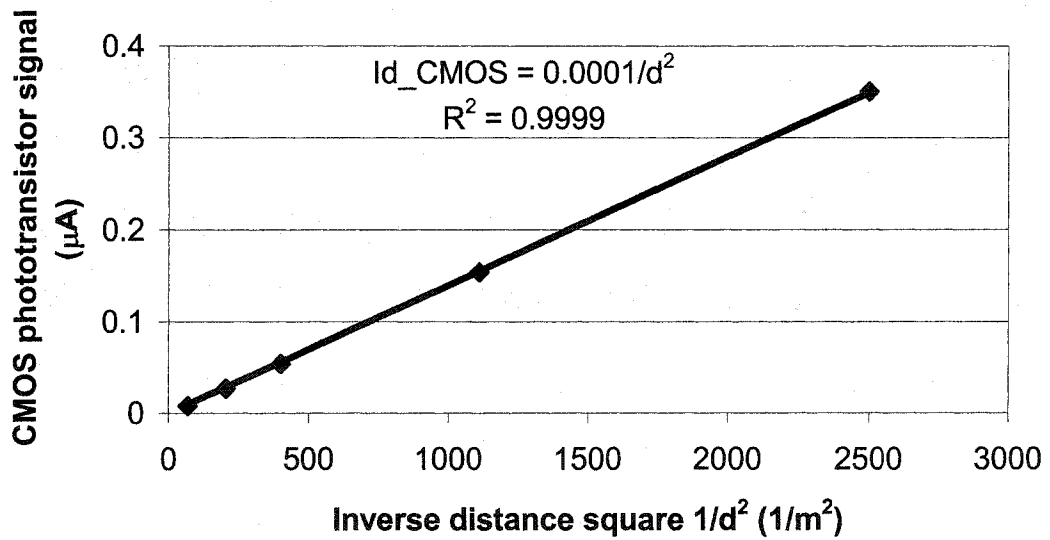


Figure 7.6 (b) Output of photodetector working in phototransistor mode versus inverse distance squared of the light source

Figure 7.7 shows the measured response of the three-mode photodetector operating in different modes. The photodetector signal is linear to the power of incident light in the range from 0.01 mW to 10 mW when it is operated in the photodiode mode and phototransistor mode. The output of the photodetector operating in phototransistor mode yields a current approximately two decades greater than that resulting from the photodiode operation mode as expected from the linearity results. The output of the photodetector operating in the Darlington connection mode is not linearly proportional to the intensity of incident light. The amplitude of the output signal increases more than two decades when the incident power is around 1 mW. This non-linearity is because the second transistor is not covered from the incident light. The output signal is a combination of the amplified signal from the first phototransistor and the photocurrent generated in the second phototransistor. In order to get the linear response from the third mode, the second phototransistor should be covered with a metal layer in the fabrication process to prevent the photocurrent from being generated. This has been improved in our next design, but no chip has been tested by the time of writing this thesis. A linear response is expected and the second transistor will amplify the magnitude of the signal by about two decades.

The output of CMOS photodetector was also tested as a function of sensitive area of the design. Figure 7.8 shows the result from two designs with two different sensitive areas working in the phototransistor mode. The ratio of the sensitive areas (the P-well region in Figure 7.4 (a)) is 8.7:1, which is the same as the average ratio of the corresponding outputs. This indicates that the output of CMOS photodetector is proportional to the area of sensitive surface.

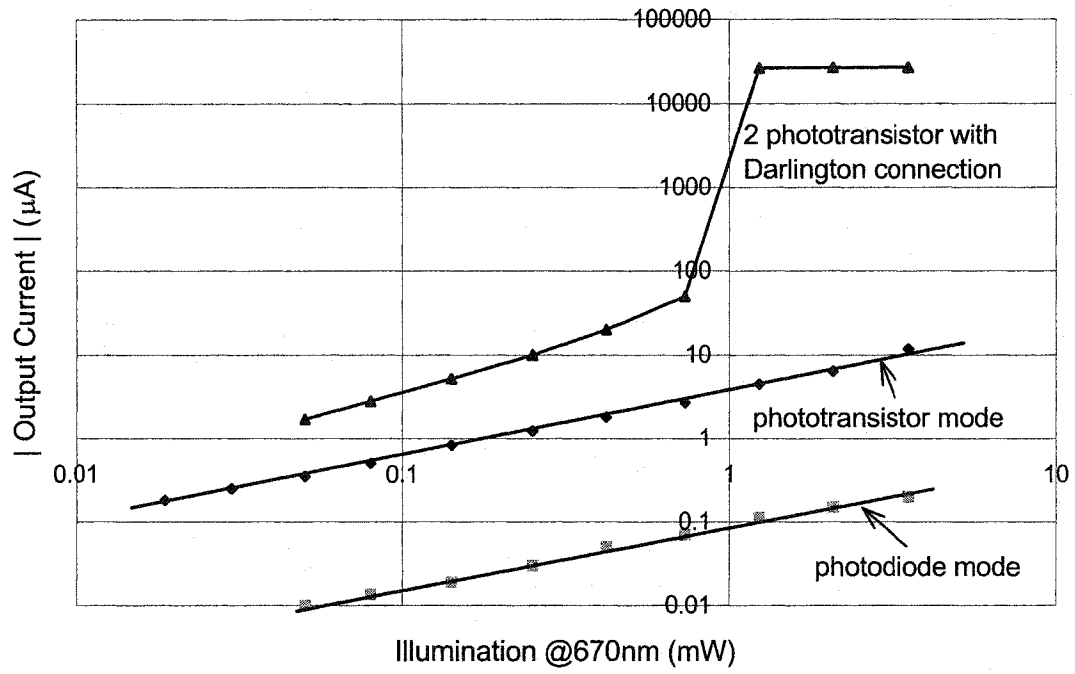


Figure 7.7 Measured response of the CMOS photodetector operating in different modes

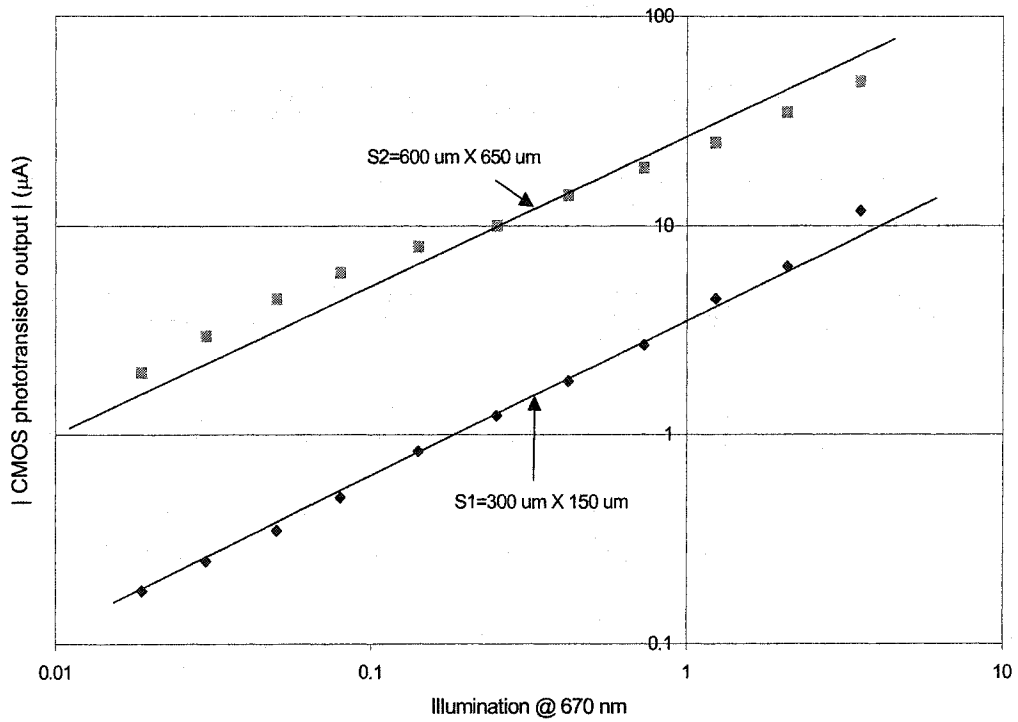


Figure 7.8 Comparison of CMOS photodetector output with two different sensitive areas in the ratio of 8.7:1



### 7.4.3 Test with a micro-radiator

The CMOS photodetector working in the phototransistor mode was used to measure the radiation from a micro-radiator. Both micro-radiator and photodetector were mounted on 40-pin DIPs and the two chips were put face-to-face with each other at a separation of 1 mm. Alignment was optimized by manually moving one device to approximately achieve maximum output signal.

Figure 7.9 shows the photodetector output versus the input power of the micro-radiator. From 7.9 we can see the output of photodetector starts to increase rapidly from about 20 mW at one atmosphere. Comparing Figure 7.9 and Figure 5.2, we can see the magnitude of the CMOS phototransistor output is much smaller than the output from the commercial photodiode. The output of the commercial photodiode is about three times bigger than the output of the CMOS phototransistor when the micro-radiator is heated with 30 mW power. The output of the CMOS photodetector operating in the photodiode mode is about 50 times even smaller than the output operating in the phototransistor mode as shown in Figure 7.7. This is due to the sensitive area of the CMOS phototransistor is about four orders of magnitude smaller than that of the commercial photodiode although the distance between the micro-radiator and the photodetector is about 25 times shorter.

The micro-radiator input power only went up to 35 mW in Figure 7.9, while the commercial photodiode was tested with a micro-radiator input power up to 60 mW. In the common range of the two figures, the photodetector response curves demonstrated a similar shape.

Figure 7.10 shows a typical response from the CMOS phototransistor used to detect the radiation from a micro-radiator with a 15 mW input in a pressure range from 100 Pa to one atmosphere. Compared with the experimental results obtained using the commercial photodiode and a power input of 14 mW in Figure 6.4, the shape of the curves is similar, but the pressure sensitive ranges are not exactly same. This may be due to the difference of the micro-radiators fabricated with two different process batches, the change of micro-radiator to photodetector distance and the different spectral response of two photodetectors.

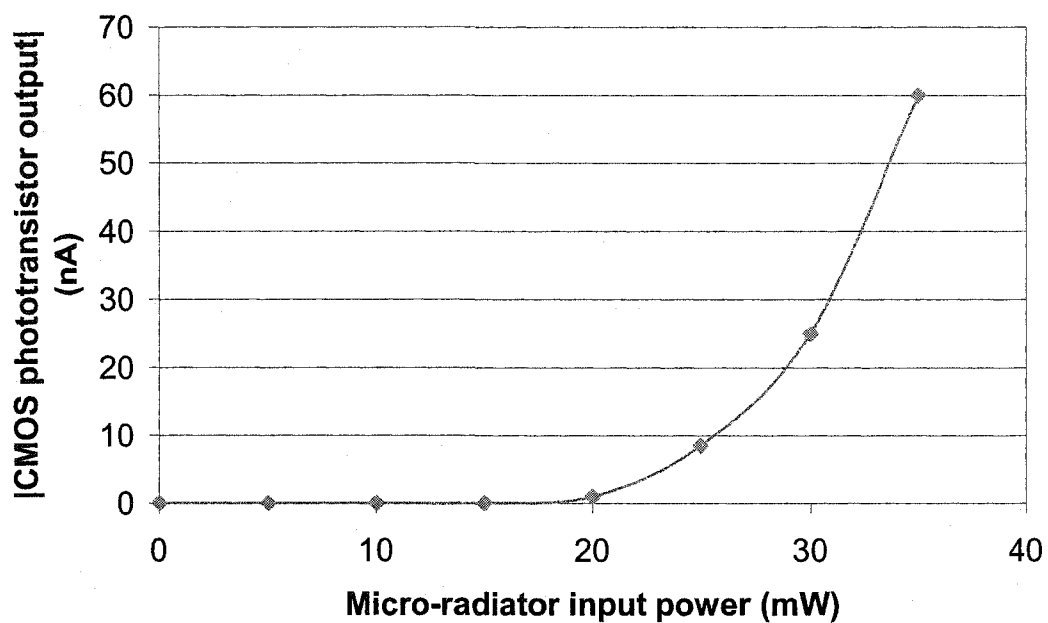


Figure 7.9 Output of CMOS photodetector working in the phototransistor mode versus power input of micro-radiator

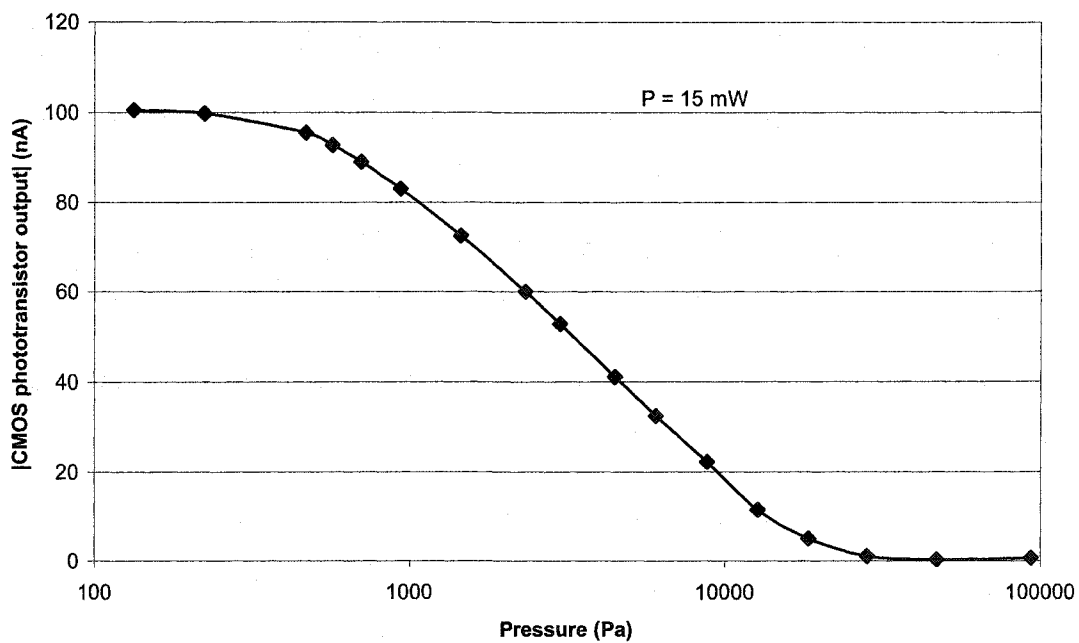


Figure 7.10 Output of CMOS photodetector working in phototransistor mode versus pressure

## **7.5 Noise in CMOS photodetector**

Noise is a rather profound subject. A complete list of all types of noise is beyond the scope of this thesis. The following types of noise are those most likely to be found in the CMOS photodetector [4]:

1. Johnson Noise: Johnson noise is sometimes call thermal noise. It occurs in all conducting materials. It is a consequence of the random motion of electrons through a conductor.
2. Shot Noise: Shot noise is often called "photon noise". It occurs in all photon detectors due to the random arrival rate of photons from the source of radiant energy under measurement and background radiation. In semiconductor diodes, the shot noise associated with the random generation of carriers is the major noise source.
3. Excess Noise: At low frequencies, there are many types of noise for which the noise power varies inversely with frequency. A common term for this type of noise is  $1/f$  noise. It is called excess noise since it exceeds shot noise at low frequencies.

Major noise in the CMOS photodetector can be any one or a combination of the above types of noise. The amplifier used with the photodetector is also made of semiconductor devices; there is also noise in the amplifier. However, all the measurement done in this project are not very sensitive to the noise. Noises were minimized in the experiment by making a number of measurements at each pressure and averaging all the experimental data and pre-offsetting the current amplifier.

## **7.6 Integration of the micro-radiator and photodetector**

We have demonstrated in this chapter that the CMOS photodetector can be used to measure the radiation from the micro-radiator. The integration of the micro-radiator and the CMOS photodetector into a whole system will provide advantages such as better performance and controllability.

Several different approaches can be used in the integration of the CMOS photodetector with the micro-radiator. A monolithic approach, in which the photodetector is fabricated on the same substrate side by side with the micro-radiator, is the simplest approach. However, because the photodetector can only collect a small portion of the radiation from the micro-radiator, a more sensitive photodetector or a micro-radiator that emits more power is necessary. The second approach is an assembly approach such as the one we used for the testing of the CMOS photodetector. Both the micro-radiator and the photodetector are individually packaged and then two chips are aligned and assembled face-to-face with each other. This allows the performance optimization of each device, but requires accurate alignment and the distance between the micro-radiator and the photodetector is limited by the package.

Flip chip MEMS has emerged as an excellent alternative to the above methods. This method involves fabricating the photodetector and the micro-radiator as separate parts and then attaching them, face-to-face, with solder bumps [5]. Figure 7.11 shows an example of the process.

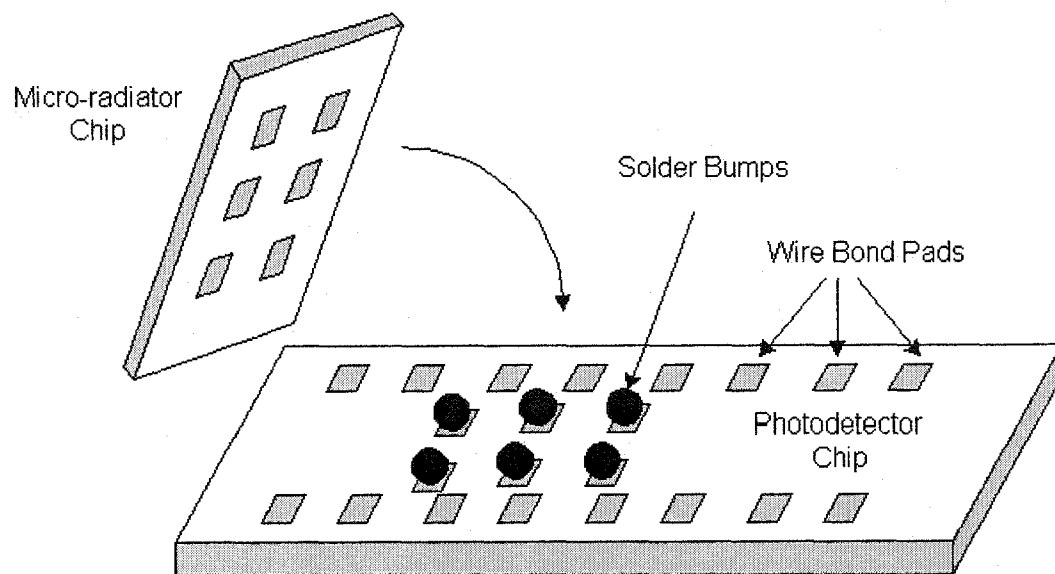


Figure 7. 11 Integration of the photodetector and micro-radiator with flip-chip technique

After the fabrication of both the micro-radiator and photodetector chips, electroplated solder bumps are created for attachment. One chip (e.g. micro-radiator chip in Figure 7.11) is then placed face down (flip chipped) on to the other chip (i.e. photodetector chip in Figure 7.11) and chips are aligned, contacted and heated to reflow the solder bumps. After solder reflow, the joined pair can be placed in a traditional package (e.g. DIP) and wire bonded as shown in Figure 7.12. The solder bumps provide both mechanical and electrical connection for two chips. The height of the solder bumps provides a distance of about 100  $\mu\text{m}$  between the micro-radiator and the photodetector, which will greatly increase the magnitude of the photodetector signal.

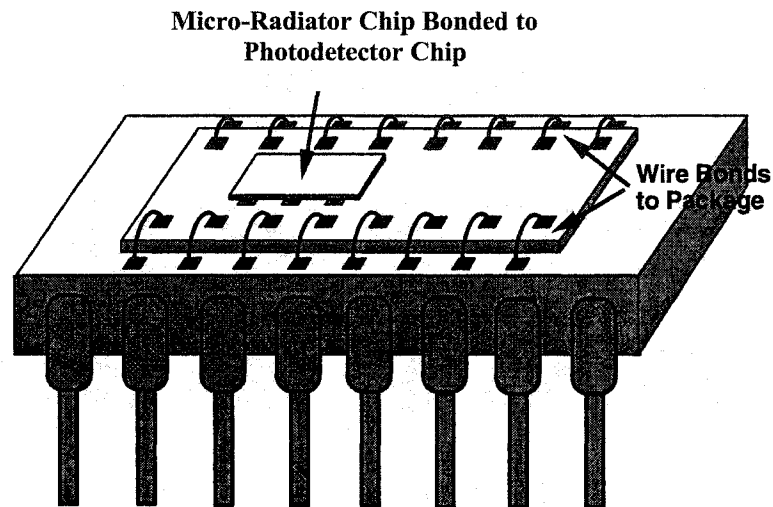


Figure 7.12 The joined micro-radiator / photodetector pair is die-attached and wire-bonded to a DIP

However, to develop a flip-chip process that is compatible with the CMOS process is time consuming and the process can be very expensive. The integration of the micro-radiator pressure sensing system is achieved using the assembling approach as shown in Figure 7.13 in this project and the flip-chip integration is included as future work.

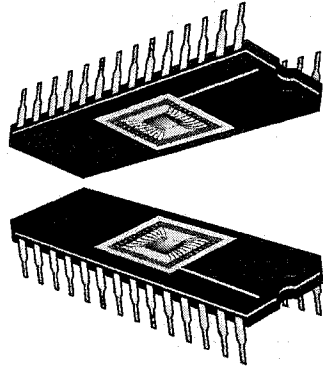


Figure 7.13 Assembling of the photodetector and micro-radiator with two DIPs

### References:

- [1] B. G. Streetman, Solid State Electronic Devices (fourth Edition), Prentice Hall Inc., London, 1995, p. 140.
- [2] R. G. Hunsperger (Ed.), Photonic devices and systems, Marcel Dekker, Inc., New York, 1994, p. 183.
- [3] V. Ward, M. Syrzycki and G. Chapman, "CMOS photodetector with built-in light adaptation mechanism", Microelectronics Journal, vol. 24, 1993, pp. 547-553.
- [4] W. Budde, Optical Radiation Measurements, Vol.4, "Physical Detectors of Optical Radiation", Academic Press, New York, 1983.
- [5] "SmartMUMPs Design Handbook - Draft 7/15/96", JDS Uniphase Inc.- MEMS Business Unit, Research Triangle Park, NC, USA, p. 37 (available through CMC and JDSU WebPages)

## Chapter 8

### Numerical Modeling

The finite element method is a powerful approach for analyzing physical problems for which no closed-form analytical solutions exist. In the finite element method, a structure is broken down into many small simple blocks or elements. The behavior of an individual element can be described with a relatively simple set of equations. Just as the set of elements would be joined together to build the whole structure, the equations describing the behaviors of the individual elements are joined into an extremely large set of equations that describe the behavior of the whole structure. The computer can solve this large set of simultaneous equations. From the solution, the computer extracts the behavior of the individual elements.

Dr. Allegretto in the Department of Mathematics of the University of Alberta developed a software package that numerically models the operation of the micro-radiator pressure sensor based on a thermal-electrical model similar to the one introduced in Chapter 3 [1]. This package is referred to as Allegretto's Package in the following text. ANSYS, a commercial finite element software available from Swanson Software, also allows us to simulate the operation of the micro-radiator under given operating conditions. Both packages are used to simulate the operation of the micro-radiator and there is no significant difference observed between the results from each package. Although results from both packages are presented in this chapter, only the procedure used to simulate the micro-radiator in ANSYS is introduced in the following section. Please refer to reference [1] for the details of the Allegretto's Package. It should be noted that the Allegretto's Package used in this project is an updated version from what is presented in reference [1], with a radiation term included.

## 8.1 Model building

The first part of any numerical simulation is building the model. This includes defining the geometry of the device, choosing a suitable element, and defining the material properties. The ANSYS element library has more than 100 different element formulations or types. Different elements have a different number of nodes, degrees of freedom. A suitable element needs to be chosen based on the analysis type and the structure of the device.

Data from the L-Edit layout are extracted for building the geometry of the device [2]. Figure 8.1 shows the 3-D model built with ANSYS 5.6. The input file for the simulation is listed in Appendix D. Two-dimensional data extracted from L-Edit is used as the base to build the 3-D model in ANSYS.

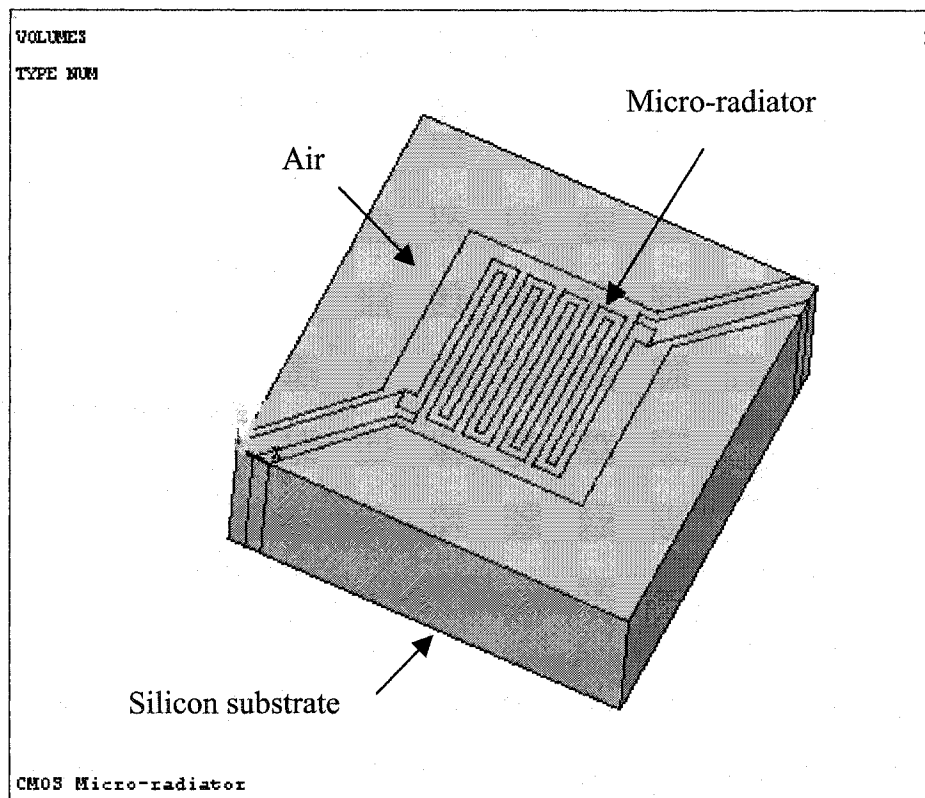


Figure 8.1 Micro-radiator model built in ANSYS



The micro-radiator is built with the air surrounding it and beneath it. The isotropic etching pit is approximated by a rectangular cavity for the simulation. The four sides and the bottom of the rectangular cavity indicate the boundary with the silicon substrate and are simulated in ANSYS by constraining the temperature of this boundary to be 293 K. The top surface of the 3-D model shown in Figure 8.1 is defined as a boundary with the air above it.

A thermal solid element (SOLID 87) is chosen for the simulation and the material properties for different parts of the model are listed in Table 8.1. SOLID 87 has ten nodes, and one degree of freedom, temperature, at each node. It is well suited to model shapes produced from various computer aided design software, e.g. L-Edit.

Table 8.1 Table of thermo-physical properties

Material	Thermal Conductivity (W/m °C)	Specific Heat (J/kg °C)	Density (kg/m <sup>3</sup> )
Polysilicon	34.0	700	2320
SiO <sub>2</sub>	1.4	1400	2190
Al	237	896	2700
Air	0.025	1010	1.21

## 8.2 Temperature distribution analysis

Temperature distribution on the platform of the micro-radiator operating at a power of 15 mW at  $10^{-5}$  Torr ( $\sim 10^{-3}$  Pa) and 740 Torr ( $\sim 10^5$  Pa) is simulated with both packages. Figure 8.2 shows the result for the temperature distribution on the micro-radiator surface at  $10^{-3}$  Pa simulated with Allegretto's package. Figure 8.3 shows the result simulated with ANSYS. Both results have similar temperature contours. The hottest points on the platform are at the two corners that are furthest away from two supporting arms and are about 1300 K from Allegretto's package and about 1400 K from ANSYS. The difference between two results is less than 10%, which is considered acceptable.

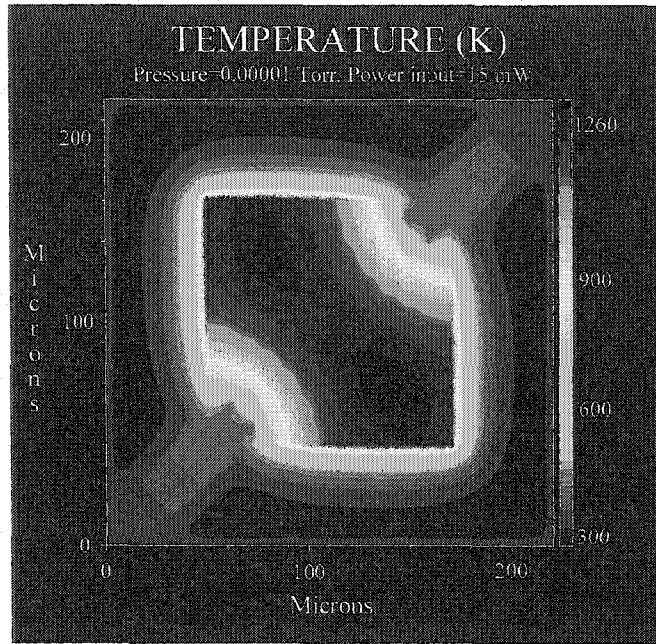


Figure 8.2 Temperature distributions operating at a power of 15 mW at  $10^{-3}$  Pa simulated with Allegretto's package

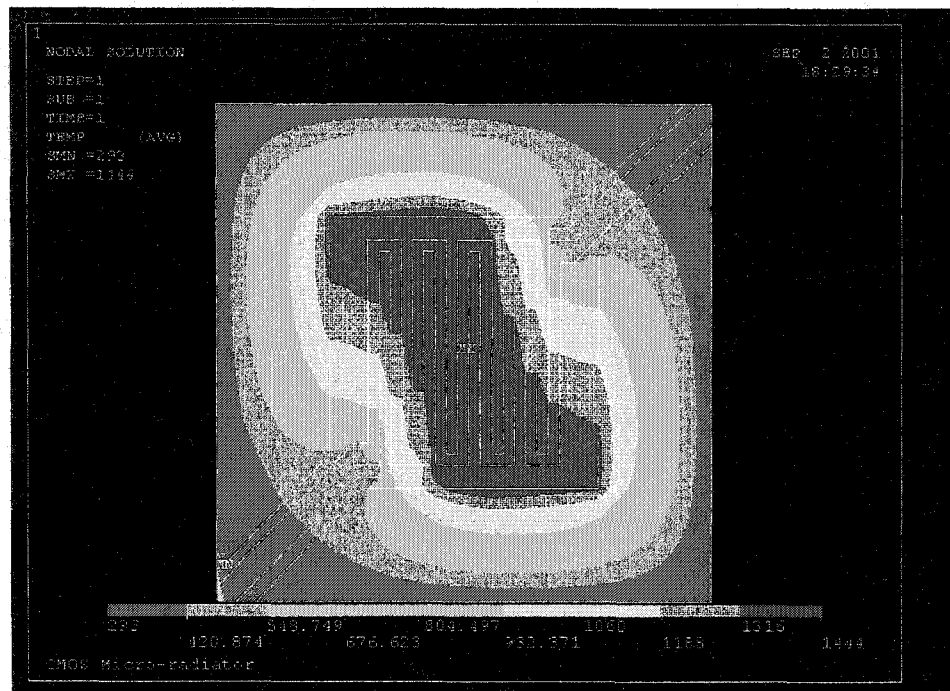


Figure 8.3 Temperature distributions operating at a power of 15 mW at  $10^{-3}$  Pa simulated with ANSYS

Figure 8.4 shows the result for the temperature distribution at  $10^5$  Pa obtained with Allegretto's package. Figure 8.5 shows the result obtained from ANSYS. The device is cooler due to increased heat transfer from the micro-radiator to the surrounding gas. The hottest point on the platform is at the center of the platform and is about 900 K with an input power of 15 mW. The average temperature of the structure is approximately 700 K, which is the same order of magnitude of the temperature calculated using resistance change in Figure 5.9 (c). Simulations from ANSYS gave similar distribution contours but the orientation of the temperature contour is slightly different to the one obtained with Dr. Allegretto's Package. This is due to the structure mesh used in the ANSYS simulation was not as dense as the mesh used in Dr. Allegretto's package.

Experimental results confirmed the simulation results qualitatively. Figure 8.6 show a picture taken after a micro-radiator had been burnt out with an excessive high power at one atmosphere. The black dot at the center of the platform shows the destruction of the structure material due to heating, indicating the location of the hottest point on the structure.

Figure 8.7 shows the photo taken after a micro-radiator was heated at 10 mW, with pressure decreases from one atmosphere down to  $10^{-3}$  Pa. From the picture we can see the hottest point moves from the center of the platform to the two corners without supporting arms and the glass at these two corners starts to deform. The device did not burn out during experiment, but the room temperature resistance of the device changed permanently after the experiment from 3.9 k $\Omega$  to 2.8 k $\Omega$ . This is due to the overheating of polysilicon particularly near the two corners without supporting arms.

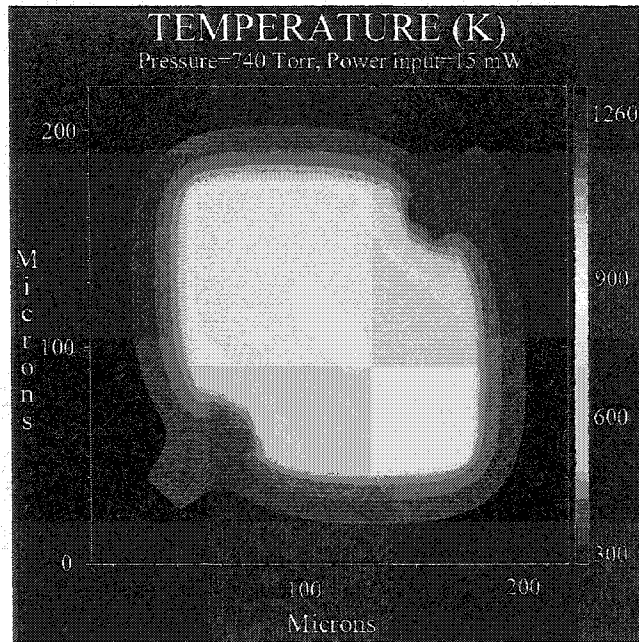


Figure 8.4 Temperature distributions operating at a power of 15 mW at  $10^5$  Pa simulated with Allegretto's package

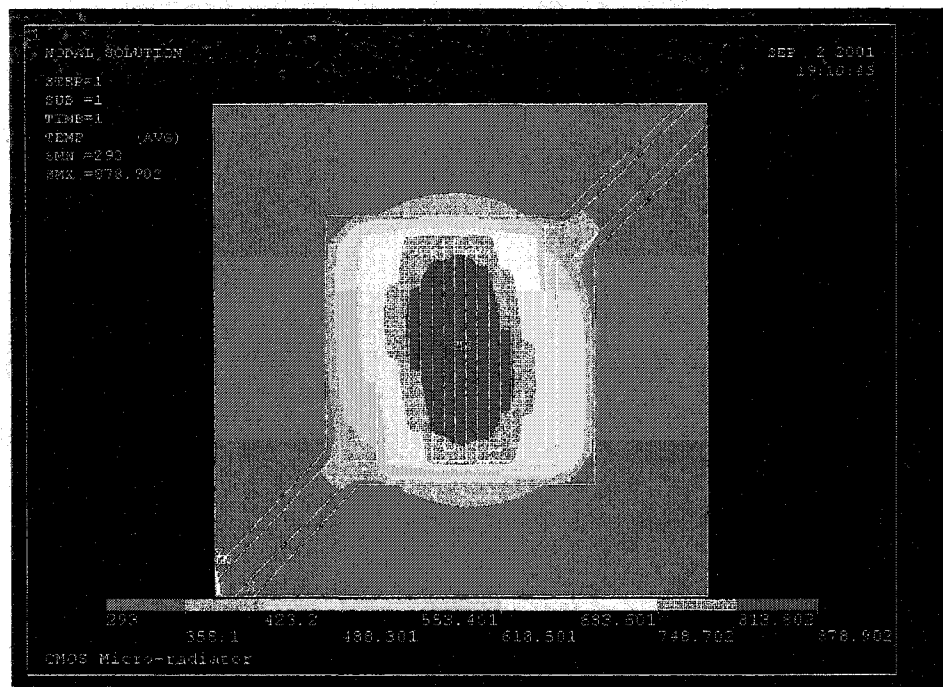


Figure 8.5 Temperature distributions operating at a power of 15 mW at  $10^5$  Pa simulated with ANSYS

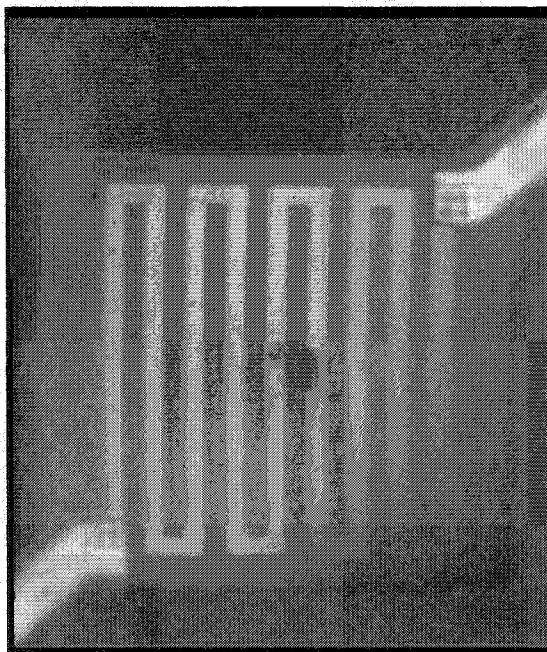


Figure 8.6 Picture of burnt out micro-radiator showing the hottest point at the center of the platform at  $10^5$  Pa

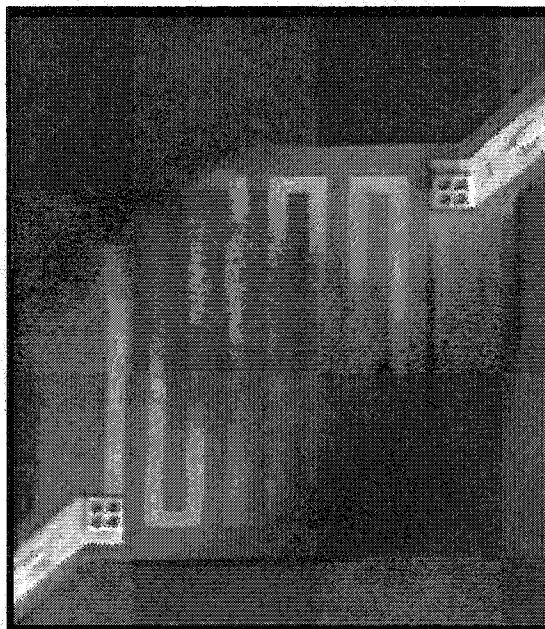


Figure 8.7 Picture of micro-radiator at  $10^{-3}$  Pa showing the hottest point at two corners of the platform without supporting arms

### 8.3 Radiation calculation

Temperature profile data from the numerical simulation are averaged to calculate the radiation from the micro-radiator using the micro-radiator radiation curve and photodetector response. Output of the photodetector is derived from the response curve of the photodetector output curve in Figure 4.14 and compared with experimental results. Figure 8.8 shows the result from Allegretto's package compared with experimental data operating at a power of 10 mW and pressure range from 0.005 Pa to 10000 Pa. The simulated photodetector output shows a good agreement with experimental data except simulated results are a little smaller than the experimental ones in the middle part of the curve.

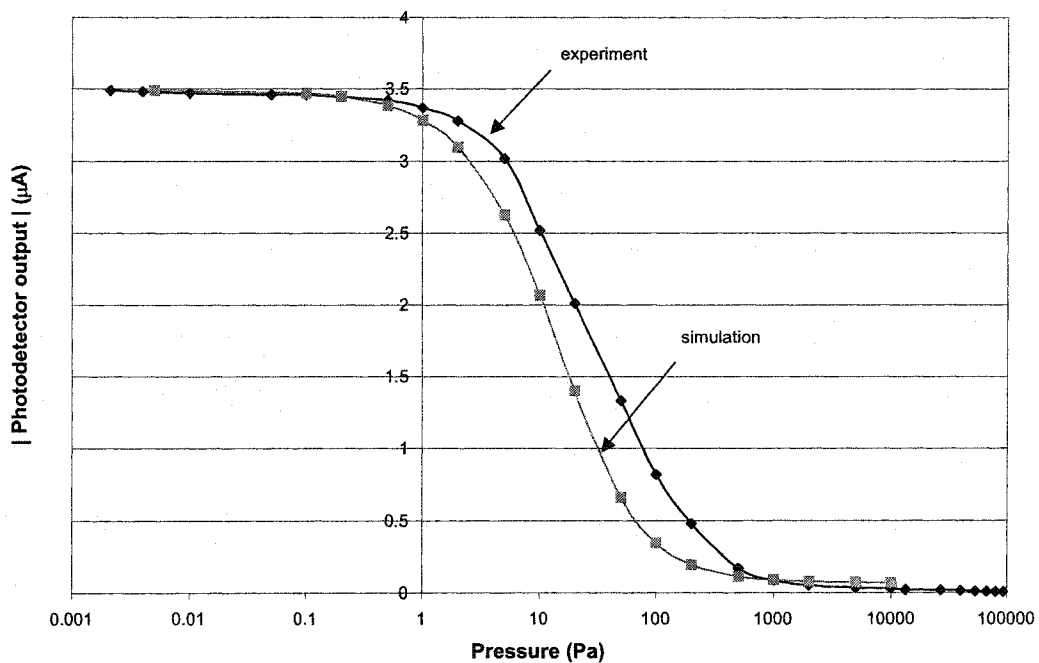


Figure 8.8 Allegretto's simulated photodetector output compared with the experimental data

Although there are limits to the numerical modeling, such as the accuracy of the simulation is dependent on the material parameters; it provided a good way to estimate the temperature distribution of the micro-radiator and guidance for future design optimization.

### **References:**

- [1] W. Allegretto, B. Shen, T. Kleckner, and A. M. Robinson, "Micromachined Polysilicon Power Dissipation: Simulation and Experiment", IEEE Transactions on Computer-Aided Design of Integrated Circuits and Systems, Vol. 16, No. 6, June 1997, pp. 627-637.
- [2] R. Yeh, "A CIF Conversion Program", Summer Report, Department of Electrical and Computer Engineering, University of Alberta, August 2000.

## Chapter 9

### Conclusions and Future Work

Conclusions on main achievements and future work of this project are included in this chapter.

#### 9.1 Conclusions

A micro-machined radiator has been designed, tested and calibrated as a thermal conductivity pressure sensor in this project. Test results demonstrate that the polysilicon micro-radiator embedded in a silicon dioxide platform is a good radiation source and measuring the variation of the radiation signal provides a sensitivity at least several orders of magnitude higher than conventional conductivity pressure sensor.

Micromachining technology helps to lower the power consumption of the device. The small size of the micro-radiator effectively minimizes the characteristic dimension of the system and therefore increases the upper limit of the sensitive range. A power-switching scheme has been introduced to operate the micro-radiator with constant radiation output to increase the pressure measurement range and extend the lifetime of the device. The pressure measurement range of the micro-radiator with the power-switching scheme is from  $10^{-3}$  –  $10^5$  Pa.

The optical radiation from the micro-radiator is measured with both commercial photodetector and a three-mode CMOS photodetector. The CMOS photodetector is tested with a point light source and the output is linear to the intensity of incidence light and proportional to the sensitive area of the device. A preliminary integration approach by



flip-assembling DIPs of micro-radiator and CMOS photodetector indicates that the CMOS photodetector and micro-radiator can be fully integrated in the future.

A micro-radiator electro-thermal model is built and the photodetector response with the pressure variation is analytically simulated. Two numerical modeling packages are used to simulate the temperature profile of the device. Both analytical and numerical simulation results give a good agreement to the experimental results.

## **9.2 Future work**

There are a few things can be done for the further study of this project.

### **9.2.1 Micro-radiator matrix design**

A micro-radiator matrix has potential application in optical image generation and thermal resolution test targets. Thermal resolution test targets are a matrix of point sources of thermal radiation used for calibrating infrared and thermal sensors [1]. Design of a  $2^n \times 2^m$  micro-radiator matrix will be discussed in this section.

For a chip containing a large number of devices, such as a MEMS chip with a 2-D matrix of micro-radiators, efficiently using the limited number of I/O pads is essential. CMOS micromachining technology provides the opportunity of on-chip circuitry, which enables multi-device addressing via standard digital decoders and analog switches and greatly reduces the requirement for I/O pads and simplifies the packaging process.

For a  $2^n \times 2^m$  micro-radiator matrix, individual control of the micro-radiators can be achieved by using two decoders and  $(2^n + 2^m)$  n-type Field Effect Transistors (nFET) with CMOS technology as shown in Figure 9.1. The nFETs are operated as electrical switches. The ON/OFF selection of the nFET is controlled by the gate voltage, which is connected to one of the outputs of the decoder. The inputs of the decoders are connected to power VDD. Only one horizontal nFET and one vertical nFET will be switched ON at each time, thus applying electrical power to the corresponding micro-radiator.

However, the MOS transistor is very susceptible to electric static discharge damage (ESD) [2]. Several hundreds volts of ESD is enough to destroy the CMOS decoder and

analog switches. Previous 2-D matrix design in the lab failed due to the ESD problem. Proper precautions should be taken in the future on both design and device handling. In design, I/O pads should include ESD protection circuits, such as diodes to sink the excessive currents and diffusion resistor to buffer the shock. A properly designed ESD protection circuit should take up to 10,000 volts of static voltage discharge. In handling, the operator should be properly grounded by wearing a wrist strap and following proper procedures.

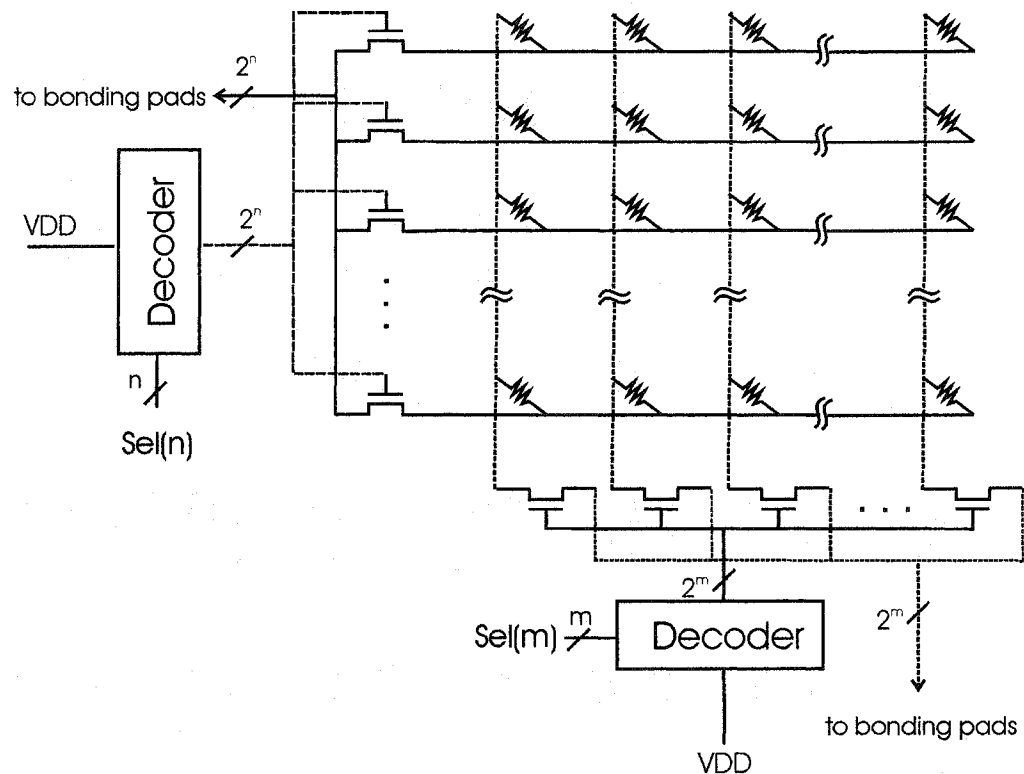


Figure 9.1 Micro-radiator matrix ( $2^n \times 2^m$ ) design

### 9.2.2 Variation of the characteristic dimension of the system

The characteristic dimension of the system will affect the upper limit of the pressure-sensitive range. The distance between the micro-radiator platform and the bottom of the etched pit in the substrate dominate the characteristic dimension in this project. Only one

distance of 85  $\mu\text{m}$  has been used and tested in this project. Future work can be done to increase the upper pressure sensitive limit by introducing a CMOS photodetector as a heat sink above the micro-radiator or reduce the depth of the etched cavity beneath the micro-radiator. However, overheating of the CMOS photodetector will change the response of the photodetector and should be avoided.

### **9.2.3 Integration of the system**

As discussed in Chapter 7, integration of the photodetector with the micro-radiator using a flip-chip process will reduce the distance between the photodetector and the micro-radiator to about 100  $\mu\text{m}$  and the photodetector signal will be increased significantly. A digital amplifier can also be designed on chip with the CMOS photodetector to increase the photodetector output.

### **9.2.4 Gas analysis using micro-radiator pressure sensing system**

The calibration curve of the system depends on the gas in the system as shown in Figure 6.12. Thus the micro-radiator pressure sensing system could possibly be used for gas analysis.

### **References:**

- [1] A. P. Pritchard, "Dynamic IR Scene Generation: Basic Requirements and Comparative Display Device Design", Proc. SPIE-940, 1988, pp. 144-149.
- [2] G. Bertrand, C. Delage, M. Bafleur et al., "Analysis and compact modeling of a vertical grounded base NPN bipolar transistor used as an ESD protection in a smart power technology", 2000 Bipolar/BiCMOS Circuits and Technology Meeting (BCTM'2000), Minneapolis, USA, 24-26 September 2000, pp.28-31.

## Appendix A

### Micro-radiator electro-thermal model analysis

This program written in Matlab was used for the electro-thermal model analysis of the micro-radiator. The program plots the temperature versus pressure curve at a certain input power based on the heat balance equation (3.2.17) introduced in Chapter 3.

```
%*****  
%Micro-radiator electro-thermal model analysis  
%*****  
% temperature range  
t = 0:0.1:5000;  
% input power in W  
w = 0.01;  
% room temperature in K  
tg = 293;  
% micro-radiator surface dimension  
x = 120*10^-6;  
y = x;  
% supporting arm length  
e = 85*10^-6;  
% distance from micro-radiator to the substrate  
s = 85*10^-6;  
%  
% radiation heat loss  
% emissivity  
eps = 0.8;  
% Stefan-Boltzmann constant  
ste = 5.67*10^-8;  
% equation (3.2.16)  
Kr = 2*eps*ste*x*y;  
%  
% conduction through arms  
% coefficient accounting for 2 supporting arms  
eta = 2;  
% poly area in the cross-section of the arm (thickness * width)  
As1 = 0.32*10^-6*10^-5;  
% thermal conductivity of poly  
ks1 = 34;  
% oxide area in the cross-section of the arm (thickness * width)  
As2 = 3.2*10^-6*10^-5;  
% thermal conductivity of oxide  
ks2 = 1.4;  
% equation (3.2.15)  
Kcs = eta*(ks1*As1+ks2*As2)/e;
```

```

% conduction through air
% accommodation coefficient
alpha = 0.9;
% ratio of specific heat of air
gama = 7/5;
% Boltzmann constant
k0 = 1.38*10^-23;
% mass of air molecule
m = 28.98/6.022*10^-23;
% equation (3.2.5)
K = 0.25*(gama+1)/(gama-1)*sqrt(2*k0/3.14159/m/tg)/100;
% coefficient accounting for first order approximation
eda = 1.5*x*y/85*10^6;
% equation (3.2.14)
Kcm = K*eda*x*y/s
%
% equation (3.2.19)
p=(w-Kcs*(t-tg)-Kr*(t.^4-tg^4))./Kcm./(t-tg);
%
% plot the results
semilogx(p,t),
hold on;
%
xlabel('Pressure (Pa)'),
ylabel('Temperature (K)'),
axis([0.01,10^4,0,2500]),

```

## Appendix B

### Experiment control system

#### B.1 User interface

Figure B.1 shows the user interface of the experimental control system.

The power level is specified by the user in the *Pulse Definition* part and can be either constant or can be a custom waveform. *Level* parameter specifies the magnitude of the power  $P$  in watts. Two columns correspond to two pulses. The length of each pulse is specified with *Duration*. *MFactor* and *AFactor* are two factors to define the growth of the new pulses. For example, after the first two pulses defined by *Level* and *Duration*, the magnitude of the new pulses  $P'$  will be  $P' = P * (MFactor) + (AFactor)$ . *Total Duration time* defines how long you wish to run the analysis. The present resistance of the micro-radiator being tested can be viewed at anytime in the top graph window so that the user can monitor the progress of the experiment while it is being run, and stop and restart the experiment at any time.

The system is also designed to have a data compression function to reduce data file sizes. The *Sensitivity* specifies which changes in power, resistance or photodiode signal will merit the data being written to file. If these quantities change by less than that specified by *Sensitivity*, data is not stored. The *Max. Power* threshold is used as a safety precaution to protect the polysilicon resistor being damaged by excessive heating. The *Alpha* value is the TCR of polysilicon; it is used to approximately calculate the temperature of the polysilicon as a reference. *Notes or Comments* will be written to the first line of the data file. The button *Data File* is used to open or create a new data file for an analysis. The button *Start Analysis* is used to start an analysis. The check boxes *Stop Analysis* and *Freeze Display* are designed for the user to stop analysis or freeze display at any stage of the experiment.

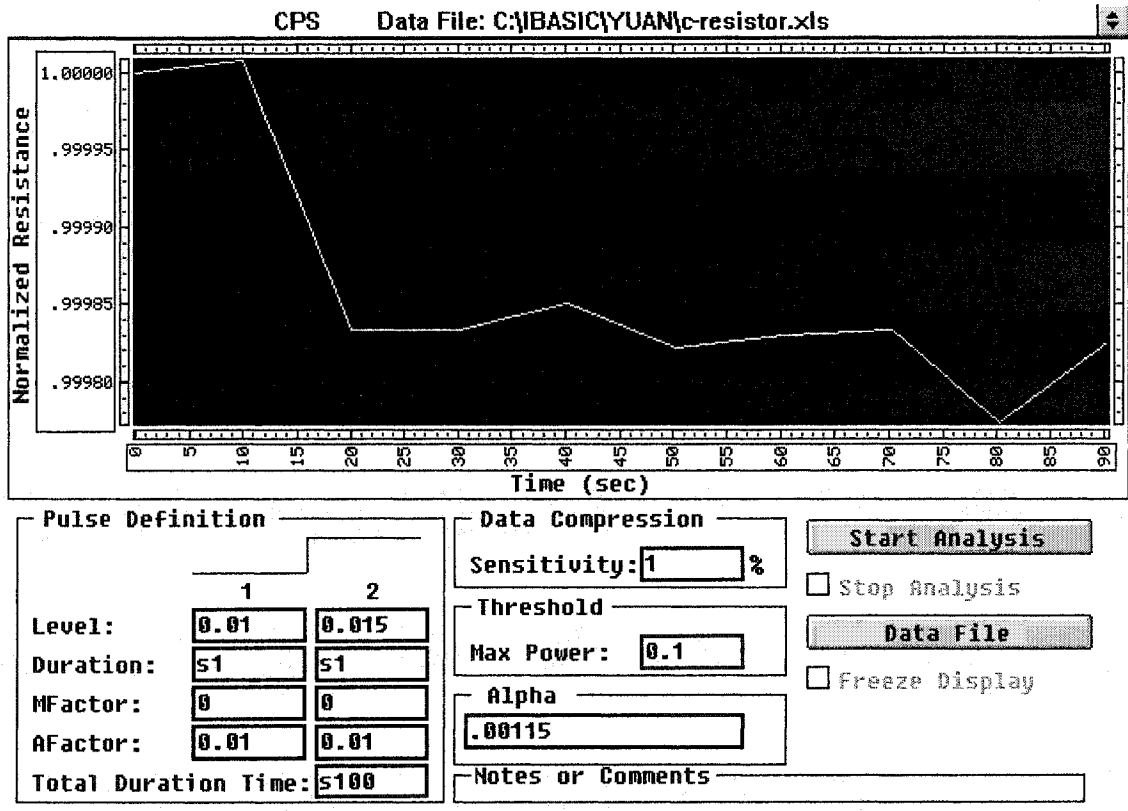


Figure B.1 Constant power supply unit user interface

## B.2 Experiment control system flow chart

The experimental control system is built with a convergent loop algorithm. A simplified flow chart of the program is shown in Figure B.2. The Source Measure Unit (SMU) supplies current ( $I$ ) and simultaneously measures voltage ( $V$ ). The Digital Multi-meter (DMM) measures the output of the photodiode ( $I_p$ ). The program sets up the SMU and DMM at the beginning of the program and a small current  $I_0$  is sent by the SMU to the micro-radiator and the voltage across the micro-radiator is measured to calculate the room temperature resistance of the micro-radiator  $R_0$ . Then the current ( $I$ ) required to heat the micro-radiator to the specified power ( $P_{set}$ ) is then calculated and sent to the micro-radiator with the voltage ( $V$ ) being measured at the same time:

$$I = \sqrt{P_{set} / R_0} \quad (\text{B.1})$$

The updated power ( $P$ ) and resistance ( $R$ ) are calculated by:

$$P = I \cdot V \quad \text{and} \quad R = V / I \quad (\text{B.2})$$

Then some judgment needs to be made to see if the total duration time has expired or if the power is too high. Then the changes of power, resistance and photodetector signal are calculated and if the change of any parameter is bigger than the sensitivity, the data are recorded in the data file. If the power doesn't exceed the maximum power, the new current  $I'$  will be calculated according to the updated resistance and sent to the micro-radiator, starting the loop again:

$$I' = \sqrt{P_{set} / R} \quad (\text{B.3})$$



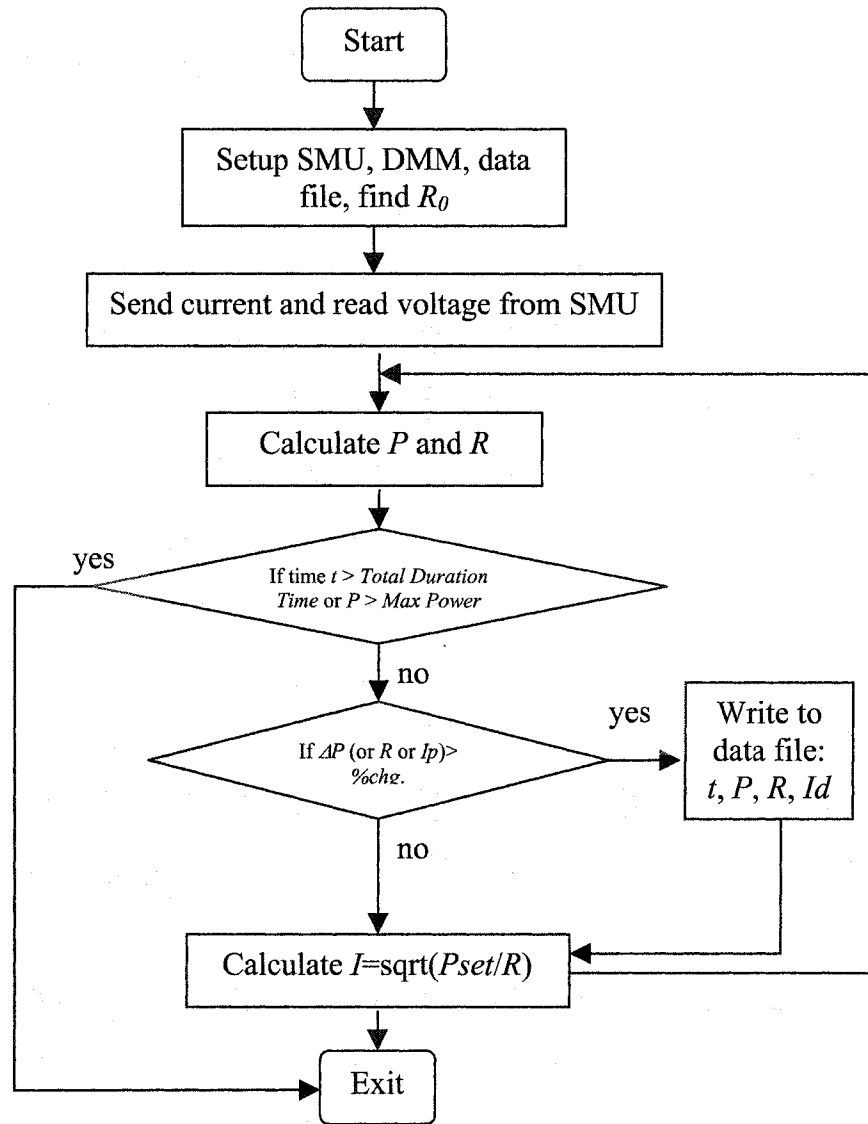


Figure B.2 Simplified flow-chart of the digital constant power supply unit and data acquisition unit

### B.3 Experimental control system program

```
10 !-----!
20 !-----!
30     REAL Vpoly, Ipoly, Rpoly, Pset, Psetold, Rpolyold, Vpolyold, Ipolyold, Rinit, Plotmax
40     REAL Inittime, Oldtime, Newtime, Savetime, Pulsestart, Pulsetime, Plottime
50     REAL Tim1, Tim2, Tim3, Fac1, Fac2, Plu1, Plu2, Seni, Sen, Thre, Rtem, Alph, Idold, Id
60     REAL Rpolyroom, Atem, Atemold, Runningave
61     REAL Psetsign, Psetoldsign
70     DIM Temp$(50)
80     DIM File$(50)
90     DIM Notes$(256)
100    REAL Rplot(1:8640), Timevalue(1:8640)
110    INTEGER Account, Accountupper, Rsetflag, Stopflag, Stopdis, Errnum, Thresflag
120    File$=""
130    Errnum=0
140    Thresflag=0
150    Stopflag=0
160    GOSUB Makepanel
170    ON EVENT @Astart, "ACTIVATED" GOSUB Mainstart
180    ON EVENT @Dfile, "ACTIVATED" GOSUB Datafile
190    ON ERROR GOTO Errorhandler
200    LOOP
210    END LOOP
220 !-----!
230 ! If specified file does not exist, it is created
240 !-----!
250 Errorhandler:
260     IF ERRN=56 THEN
270         CREATE File$,1
280         ASSIGN @File TO File$;FORMAT ON
290     END IF
300     IF ERRN=32 AND Errnum=0 THEN
310         Errnum=1
320         DIALOG "WARNING", "Error in numerical data"
330     END IF
340     RETURN
350 !-----!
360 Mainstart:
370     STATUS @Lev1;RETURN("VALUE":Lev1$)
380     STATUS @Lev2;RETURN("VALUE":Lev2$)
390     STATUS @Tim1;RETURN("VALUE":Tim1$)
400     STATUS @Tim2;RETURN("VALUE":Tim2$)
410     STATUS @Fac1;RETURN("VALUE":Fac1$)
420     STATUS @Fac2;RETURN("VALUE":Fac2$)
430     STATUS @Add1;RETURN("VALUE":Add1$)
440     STATUS @Add2;RETURN("VALUE":Add2$)
450     STATUS @Tim3;RETURN("VALUE":Tim3$)
460     STATUS @Sen1;RETURN("VALUE":Sen1$)
470     STATUS @Thres;RETURN("VALUE":Thres$)
480     STATUS @Notes;RETURN("VALUE":Notes$)
481     STATUS @Alphe;RETURN("VALUE":Alpha$)
490     !
500     IF Lev1$="" OR Lev2$="" OR Tim1$="" OR Tim2$="" OR Fac1$="" OR Fac2$="" OR Add1$=""
OR Add2$="" OR Tim3$="" OR Sen1$="" OR Thres$="" OR File$="" THEN
501     DIALOG "WARNING", "All necessary data not available"
520     ELSE
530         Errnum=0
540         Lev1=VAL(Lev1$)
550         IF Lev1=0 THEN
560             Lev1=2.5E-5
570         END IF
580         Lev2=VAL(Lev2$)
590         IF Lev2=0 THEN
600             Lev2=2.5E-5
610         END IF
620     !
630     IF Tim1$[1;1]="s" THEN
```

```

640         Tim1=VAL(Tim1$[2;8])
650     END IF
660     IF Tim1$[1;1]="m" THEN
670         Tim1=VAL(Tim1$[2;8])*60
680     END IF
690     IF Tim1$[1;1]="h" THEN
700         Tim1=VAL(Tim1$[2;8])*3600
710     END IF
720     IF Tim1$[1;1]="d" THEN
730         Tim1=VAL(Tim1$[2;8])*86400
740     END IF
750 !
760     IF Tim2$[1;1]="s" THEN
770         Tim2=VAL(Tim2$[2;8])
780     END IF
790     IF Tim2$[1;1]="m" THEN
800         Tim2=VAL(Tim2$[2;8])*60
810     END IF
820     IF Tim2$[1;1]="h" THEN
830         Tim2=VAL(Tim2$[2;8])*3600
840     END IF
850     IF Tim2$[1;1]="d" THEN
860         Tim2=VAL(Tim2$[2;8])*86400
870     END IF
880 !
890     IF Tim3$[1;1]="s" THEN
900         Tim3=VAL(Tim3$[2;8])
910     END IF
920     IF Tim3$[1;1]="m" THEN
930         Tim3=VAL(Tim3$[2;8])*60.
940     END IF
950     IF Tim3$[1;1]="h" THEN
960         Tim3=VAL(Tim3$[2;8])*3600.
970     END IF
980     IF Tim3$[1;1]="d" THEN
990         Tim3=VAL(Tim3$[2;8])*86400
1000    END IF
1010 !
1020    Fac1=VAL(Fac1$)
1030    Fac2=VAL(Fac2$)
1040    Plu1=VAL(Add1$)
1050    Plu2=VAL(Add2$)
1060    Sen1=VAL(Sen1$)
1070    Thre=VAL(Thres$)
1071    Rtemp$="25"
1080    Rtem=25.
1081    IF Alpha$="" THEN
1082        Alpha$="0.00115"
1083        Alph=.00115
1084    ELSE
1090        Alph=VAL(Alpha$)
1091    END IF
1100    IF Errnum=1 THEN
1110        RETURN
1120    END IF
1130 !
1140    CONTROL @Astart;SET("SENSITIVE":0)
1150    CONTROL @Astop;SET("SENSITIVE":1)
1151    CONTROL @Dstop;SET("SENSITIVE":1)
1160    GOSUB Constantpower
1170    IF Stopflag=0 THEN
1180        IF Thresflag=0 THEN
1190            DIALOG "INFORMATION","Analysis Complete"
1200        ELSE
1210            DIALOG "INFORMATION","Terminated: Max Power Exceeded"
1220        END IF
1230    ELSE
1240        DIALOG "INFORMATION","Terminated: Stopped By User"
1250    END IF
1260    CONTROL @Astart;SET("SENSITIVE":1)

```

```

1270     CONTROL @Astop;SET("VALUE":0)
1280     CONTROL @Astop;SET("SENSITIVE":0)
1281     CONTROL @Dstop;SET("VALUE":0)
1282     CONTROL @Dstop;SET("SENSITIVE":0)
1290     END IF
1300     RETURN
1310 !-----!
1320 !-----!
1330 ! Define datafile Subroutine
1340 !-----!
1350 Datafile:!
1360 Msg$="Select A Data File"
1370 DIALOG "FILE",Msg$;SET("PATTERN": "*.XLS"),RETURN("SELECTION":File$)
1380 CONTROL @Mainpanel;SET("TITLE": "CPS      Data File: "&File$)
1390 RETURN
1400 !-----!
1410 ! Define Main Panel Subroutine
1420 !-----!
1430 Makepanel:!
1440 ASSIGN @Mainpanel TO WIDGET "PANEL";SET("TITLE": "CPS")
1450 !
1460 !
1470 ! 1) Definition of Plotting Area
1480 ASSIGN @Plot TO WIDGET "XY GRAPH";SET("VISIBLE":0),PARENT @Mainpanel
1490     CONTROL @Plot;SET("TRACE BACKGROUND":0)
1500     CONTROL @Plot;SET("X":0)
1510     CONTROL @Plot;SET("Y":0)
1520     CONTROL @Plot;SET("HEIGHT":260)
1530     CONTROL @Plot;SET("WIDTH":640)
1540 ! CONTROL @Plot;SET("TRACE COUNT":1)
1550     CONTROL @Plot;SET("CURRENT AXIS": "X", "AXIS LABEL": "Time (sec)")
1560     CONTROL @Plot;SET("AUTOSCALE":1)
1570     CONTROL @Plot;SET("CURRENT AXIS": "Y", "AXIS LABEL": "Normalized Resistance")
1580     CONTROL @Plot;SET("AUTOSCALE":1)
1590     CONTROL @Plot;SET("CURRENT TRACE":1)
1600     CONTROL @Plot;SET("VISIBLE":1)
1610 !
1620 !-----!
1630 ! 2) Definition of pulse Definition panel
1640 ASSIGN @Pulse TO WIDGET "PANEL";PARENT @Mainpanel
1650     CONTROL @Pulse;SET("VISIBLE":0)
1660     CONTROL @Pulse;SET("X":5)
1670     CONTROL @Pulse;SET("Y":270)
1680     CONTROL @Pulse;SET("HEIGHT":185)
1690     CONTROL @Pulse;SET("WIDTH":245)
1700     CONTROL @Pulse;SET("BORDER":1)
1710     CONTROL @Pulse;SET("VISIBLE":1)
1720 ASSIGN @Plabel TO WIDGET "LABEL";PARENT @Mainpanel
1730     CONTROL @Plabel;SET("VISIBLE":0)
1740     CONTROL @Plabel;SET("X":15)
1750     CONTROL @Plabel;SET("Y":260)
1760     CONTROL @Plabel;SET("HEIGHT":20)
1770     CONTROL @Plabel;SET("WIDTH":140)
1780     CONTROL @Plabel;SET("BORDER":0)
1790     CONTROL @Plabel;SET("VALUE": "Pulse Definition")
1800     CONTROL @Plabel;SET("JUSTIFICATION": "CENTER")
1810     CONTROL @Plabel;SET("VISIBLE":1)
1820 ASSIGN @Pheader TO WIDGET "LABEL";PARENT @Pulse
1830     CONTROL @Pheader;SET("VISIBLE":0)
1840     CONTROL @Pheader;SET("X":100)
1850     CONTROL @Pheader;SET("Y":30)
1860     CONTROL @Pheader;SET("HEIGHT":20)
1870     CONTROL @Pheader;SET("WIDTH":120)
1880     CONTROL @Pheader;SET("BORDER":0)
1890     CONTROL @Pheader;SET("VALUE": "  1      2")
1900     CONTROL @Pheader;SET("JUSTIFICATION": "LEFT")
1910     CONTROL @Pheader;SET("VISIBLE":1)
1920 !
1930 ! Draw diagram
1940 !

```

```

1950 ASSIGN @Pline1 TO WIDGET "LABEL";PARENT @Pulse
1960 CONTROL @Pline1;SET("X":100)
1970 CONTROL @Pline1;SET("Y":30)
1980 CONTROL @Pline1;SET("HEIGHT":1)
1990 CONTROL @Pline1;SET("WIDTH":65)
2000 CONTROL @Pline1;SET("BORDER":1)
2010 CONTROL @Pline1;SET("VALUE":" ")
2020 CONTROL @Pline1;SET("VISIBLE":1)
2030 ASSIGN @Pline2 TO WIDGET "LABEL";PARENT @Pulse
2040 CONTROL @Pline2;SET("X":165)
2050 CONTROL @Pline2;SET("Y":10)
2060 CONTROL @Pline2;SET("HEIGHT":20)
2070 CONTROL @Pline2;SET("WIDTH":1)
2080 CONTROL @Pline2;SET("BORDER":1)
2090 CONTROL @Pline2;SET("VALUE":" ")
2100 CONTROL @Pline2;SET("VISIBLE":1)
2110 ASSIGN @Pline3 TO WIDGET "LABEL";PARENT @Pulse
2120 CONTROL @Pline3;SET("X":165)
2130 CONTROL @Pline3;SET("Y":10)
2140 CONTROL @Pline3;SET("HEIGHT":1)
2150 CONTROL @Pline3;SET("WIDTH":65)
2160 CONTROL @Pline3;SET("BORDER":1)
2170 CONTROL @Pline3;SET("VALUE":" ")
2180 CONTROL @Pline3;SET("VISIBLE":1)
2190 !
2200 ASSIGN @Plevel TO WIDGET "LABEL";PARENT @Pulse
2210 CONTROL @Plevel;SET("VISIBLE":0)
2220 CONTROL @Plevel;SET("X":5)
2230 CONTROL @Plevel;SET("Y":50)
2240 CONTROL @Plevel;SET("HEIGHT":20)
2250 CONTROL @Plevel;SET("WIDTH":80)
2260 CONTROL @Plevel;SET("BORDER":0)
2270 CONTROL @Plevel;SET("VALUE":"Level:")
2280 CONTROL @Plevel;SET("JUSTIFICATION":"LEFT")
2290 CONTROL @Plevel;SET("VISIBLE":1)
2300 ASSIGN @Pdtype TO WIDGET "LABEL";PARENT @Pulse
2310 CONTROL @Pdtype;SET("VISIBLE":0)
2320 CONTROL @Pdtype;SET("X":5)
2330 CONTROL @Pdtype;SET("Y":72)
2340 CONTROL @Pdtype;SET("HEIGHT":20)
2350 CONTROL @Pdtype;SET("WIDTH":80)
2360 CONTROL @Pdtype;SET("BORDER":0)
2370 CONTROL @Pdtype;SET("VALUE":"Duration:")
2380 CONTROL @Pdtype;SET("JUSTIFICATION":"LEFT")
2390 CONTROL @Pdtype;SET("VISIBLE":1)
2400 ASSIGN @Pmfac TO WIDGET "LABEL";PARENT @Pulse
2410 CONTROL @Pmfac;SET("VISIBLE":0)
2420 CONTROL @Pmfac;SET("X":5)
2430 CONTROL @Pmfac;SET("Y":94)
2440 CONTROL @Pmfac;SET("HEIGHT":20)
2450 CONTROL @Pmfac;SET("WIDTH":80)
2460 CONTROL @Pmfac;SET("BORDER":0)
2470 CONTROL @Pmfac;SET("VALUE":"Mfactor:")
2480 CONTROL @Pmfac;SET("JUSTIFICATION":"LEFT")
2490 CONTROL @Pmfac;SET("VISIBLE":1)
2500 ASSIGN @Pafac TO WIDGET "LABEL";PARENT @Pulse
2510 CONTROL @Pafac;SET("VISIBLE":0)
2520 CONTROL @Pafac;SET("X":5)
2530 CONTROL @Pafac;SET("Y":116)
2540 CONTROL @Pafac;SET("HEIGHT":20)
2550 CONTROL @Pafac;SET("WIDTH":80)
2560 CONTROL @Pafac;SET("BORDER":0)
2570 CONTROL @Pafac;SET("VALUE":"Afactor:")
2580 CONTROL @Pafac;SET("JUSTIFICATION":"LEFT")
2590 CONTROL @Pafac;SET("VISIBLE":1)
2600 ASSIGN @Pptime TO WIDGET "LABEL";PARENT @Pulse
2610 CONTROL @Pptime;SET("VISIBLE":0)
2620 CONTROL @Pptime;SET("X":5)
2630 CONTROL @Pptime;SET("Y":138)
2640 CONTROL @Pptime;SET("HEIGHT":20)

```

```

2650 CONTROL @Ptttime;SET("WIDTH":165)
2660 CONTROL @Ptttime;SET("BORDER":0)
2670 CONTROL @Ptttime;SET("VALUE":"Total Duration Time:")
2680 CONTROL @Ptttime;SET("JUSTIFICATION":"LEFT")
2690 CONTROL @Ptttime;SET("VISIBLE":1)
2700 ASSIGN @Pequ TO WIDGET "LABEL";PARENT @Pulse
2710 CONTROL @Pequ;SET("VISIBLE":0)
2720 CONTROL @Pequ;SET("X":22)
2730 CONTROL @Pequ;SET("Y":160)
2740 CONTROL @Pequ;SET("HEIGHT":20)
2750 CONTROL @Pequ;SET("WIDTH":220)
2760 CONTROL @Pequ;SET("BORDER":0)
2770 CONTROL @Pequ;SET("VALUE":"P=P'*(Mfactor)+(Afactor)")
2780 CONTROL @Pequ;SET("JUSTIFICATION":"LEFT")
2790 CONTROL @Pequ;SET("VISIBLE":1)
2800 !
2810 !
2820 ! 2b) Definition of Pulse Definition Edit boxes
2830 ASSIGN @Lev1 TO WIDGET "STRING";PARENT @Pulse
2840 CONTROL @Lev1;SET("VISIBLE":0)
2850 CONTROL @Lev1;SET("X":100)
2860 CONTROL @Lev1;SET("Y":50)
2870 CONTROL @Lev1;SET("HEIGHT":20)
2880 CONTROL @Lev1;SET("WIDTH":65)
2890 CONTROL @Lev1;SET("BORDER":1)
2900 CONTROL @Lev1;SET("VISIBLE":1)
2910 ASSIGN @Lev2 TO WIDGET "STRING";PARENT @Pulse
2920 CONTROL @Lev2;SET("VISIBLE":0)
2930 CONTROL @Lev2;SET("X":170)
2940 CONTROL @Lev2;SET("Y":50)
2950 CONTROL @Lev2;SET("HEIGHT":20)
2960 CONTROL @Lev2;SET("WIDTH":65)
2970 CONTROL @Lev2;SET("BORDER":1)
2980 CONTROL @Lev2;SET("VISIBLE":1)
2990 ASSIGN @Tim1 TO WIDGET "STRING";PARENT @Pulse
3000 CONTROL @Tim1;SET("VISIBLE":0)
3010 CONTROL @Tim1;SET("X":100)
3020 CONTROL @Tim1;SET("Y":72)
3030 CONTROL @Tim1;SET("HEIGHT":20)
3040 CONTROL @Tim1;SET("WIDTH":65)
3050 CONTROL @Tim1;SET("BORDER":1)
3060 CONTROL @Tim1;SET("VISIBLE":1)
3070 ASSIGN @Tim2 TO WIDGET "STRING";PARENT @Pulse
3080 CONTROL @Tim2;SET("VISIBLE":0)
3090 CONTROL @Tim2;SET("X":170)
3100 CONTROL @Tim2;SET("Y":72)
3110 CONTROL @Tim2;SET("HEIGHT":20)
3120 CONTROL @Tim2;SET("WIDTH":65)
3130 CONTROL @Tim2;SET("BORDER":1)
3140 CONTROL @Tim2;SET("VISIBLE":1)
3150 ASSIGN @Fac1 TO WIDGET "STRING";PARENT @Pulse
3160 CONTROL @Fac1;SET("VISIBLE":0)
3170 CONTROL @Fac1;SET("X":100)
3180 CONTROL @Fac1;SET("Y":94)
3190 CONTROL @Fac1;SET("HEIGHT":20)
3200 CONTROL @Fac1;SET("WIDTH":65)
3210 CONTROL @Fac1;SET("BORDER":1)
3220 CONTROL @Fac1;SET("VISIBLE":1)
3230 ASSIGN @Fac2 TO WIDGET "STRING";PARENT @Pulse
3240 CONTROL @Fac2;SET("VISIBLE":0)
3250 CONTROL @Fac2;SET("X":170)
3260 CONTROL @Fac2;SET("Y":94)
3270 CONTROL @Fac2;SET("HEIGHT":20)
3280 CONTROL @Fac2;SET("WIDTH":65)
3290 CONTROL @Fac2;SET("BORDER":1)
3300 CONTROL @Fac2;SET("VISIBLE":1)
3310 ASSIGN @Add1 TO WIDGET "STRING";PARENT @Pulse
3320 CONTROL @Add1;SET("VISIBLE":0)
3330 CONTROL @Add1;SET("X":100)
3340 CONTROL @Add1;SET("Y":116)

```

```

3350 CONTROL @Add1;SET("HEIGHT":20)
3360 CONTROL @Add1;SET("WIDTH":65)
3370 CONTROL @Add1;SET("BORDER":1)
3380 CONTROL @Add1;SET("VISIBLE":1)
3390 ASSIGN @Add2 TO WIDGET "STRING";PARENT @Pulse
3400 CONTROL @Add2;SET("VISIBLE":0)
3410 CONTROL @Add2;SET("X":170)
3420 CONTROL @Add2;SET("Y":116)
3430 CONTROL @Add2;SET("HEIGHT":20)
3440 CONTROL @Add2;SET("WIDTH":65)
3450 CONTROL @Add2;SET("BORDER":1)
3460 CONTROL @Add2;SET("VISIBLE":1)
3470 ASSIGN @Tim3 TO WIDGET "STRING";PARENT @Pulse
3480 CONTROL @Tim3;SET("VISIBLE":0)
3490 CONTROL @Tim3;SET("X":170)
3500 CONTROL @Tim3;SET("Y":138)
3510 CONTROL @Tim3;SET("HEIGHT":20)
3520 CONTROL @Tim3;SET("WIDTH":65)
3530 CONTROL @Tim3;SET("BORDER":1)
3540 CONTROL @Tim3;SET("VISIBLE":1)
3550 !
3560 !-----
3570 ! 3) Definition of Date compression panel
3580 ASSIGN @Dcompress TO WIDGET "PANEL";PARENT @Mainpanel
3590 CONTROL @Dcompress;SET("VISIBLE":0)
3600 CONTROL @Dcompress;SET("X":255)
3610 CONTROL @Dcompress;SET("Y":270)
3620 CONTROL @Dcompress;SET("HEIGHT":40)
3630 CONTROL @Dcompress;SET("WIDTH":190)
3640 CONTROL @Dcompress;SET("BORDER":1)
3650 CONTROL @Dcompress;SET("VISIBLE":1)
3660 ASSIGN @Dlabel TO WIDGET "LABEL";PARENT @Mainpanel
3670 CONTROL @Dlabel;SET("VISIBLE":0)
3680 CONTROL @Dlabel;SET("X":265)
3690 CONTROL @Dlabel;SET("Y":260)
3700 CONTROL @Dlabel;SET("HEIGHT":20)
3710 CONTROL @Dlabel;SET("WIDTH":140)
3720 CONTROL @Dlabel;SET("BORDER":0)
3730 CONTROL @Dlabel;SET("VALUE":"Data Compression")
3740 CONTROL @Dlabel;SET("JUSTIFICATION":"CENTER")
3750 CONTROL @Dlabel;SET("VISIBLE":1)
3760 ASSIGN @Dsensitive TO WIDGET "LABEL";PARENT @Dcompress
3770 CONTROL @Dsensitive;SET("VISIBLE":0)
3780 CONTROL @Dsensitive;SET("X":5)
3790 CONTROL @Dsensitive;SET("Y":15)
3800 CONTROL @Dsensitive;SET("HEIGHT":20)
3810 CONTROL @Dsensitive;SET("WIDTH":190)
3820 CONTROL @Dsensitive;SET("BORDER":0)
3830 CONTROL @Dsensitive;SET("VALUE":"Sensitivity: %")
3840 CONTROL @Dsensitive;SET("JUSTIFICATION":"LEFT")
3850 CONTROL @Dsensitive;SET("VISIBLE":1)
3860 !
3870 !
3880 ! 3a) Definition of Data compression edit boxes
3890 ASSIGN @Sen1 TO WIDGET "STRING";PARENT @Dcompress
3900 CONTROL @Sen1;SET("VISIBLE":0)
3910 CONTROL @Sen1;SET("X":105)
3920 CONTROL @Sen1;SET("Y":15)
3930 CONTROL @Sen1;SET("HEIGHT":20)
3940 CONTROL @Sen1;SET("WIDTH":60)
3950 CONTROL @Sen1;SET("BORDER":1)
3960 CONTROL @Sen1;SET("VISIBLE":1)
3970 !
3980 !-----
3990 !
4000 ! 4) Definition of Threshold panel
4010 ASSIGN @Threshold TO WIDGET "PANEL";PARENT @Mainpanel
4020 CONTROL @Threshold;SET("VISIBLE":0)
4030 CONTROL @Threshold;SET("X":255)
4040 CONTROL @Threshold;SET("Y":320)

```

```

4050 CONTROL @Threshold;SET("HEIGHT":40)
4060 CONTROL @Threshold;SET("WIDTH":190)
4070 CONTROL @Threshold;SET("BORDER":1)
4080 CONTROL @Threshold;SET("VISIBLE":1)
4090 ASSIGN @Tlabel TO WIDGET "LABEL";PARENT @Mainpanel
4100 CONTROL @Tlabel;SET("VISIBLE":0)
4110 CONTROL @Tlabel;SET("X":265)
4120 CONTROL @Tlabel;SET("Y":310)
4130 CONTROL @Tlabel;SET("HEIGHT":20)
4140 CONTROL @Tlabel;SET("WIDTH":80)
4150 CONTROL @Tlabel;SET("BORDER":0)
4160 CONTROL @Tlabel;SET("VALUE":"Threshold")
4170 CONTROL @Tlabel;SET("JUSTIFICATION":"CENTER")
4180 CONTROL @Tlabel;SET("VISIBLE":1)
4190 ASSIGN @Maxp TO WIDGET "LABEL";PARENT @Threshold
4200 CONTROL @Maxp;SET("VISIBLE":0)
4210 CONTROL @Maxp;SET("X":5)
4220 CONTROL @Maxp;SET("Y":15)
4230 CONTROL @Maxp;SET("HEIGHT":20)
4240 CONTROL @Maxp;SET("WIDTH":120)
4250 CONTROL @Maxp;SET("BORDER":0)
4260 CONTROL @Maxp;SET("VALUE":"Max Power:")
4270 CONTROL @Maxp;SET("JUSTIFICATION":"LEFT")
4280 CONTROL @Maxp;SET("VISIBLE":1)
4290 !
4300 !
4310 ! 4a) Definition of Data compression edit boxes
4320 ASSIGN @Thres TO WIDGET "STRING";PARENT @Threshold
4330 CONTROL @Thres;SET("VISIBLE":0)
4340 CONTROL @Thres;SET("X":105)
4350 CONTROL @Thres;SET("Y":15)
4360 CONTROL @Thres;SET("HEIGHT":20)
4370 CONTROL @Thres;SET("WIDTH":60)
4380 CONTROL @Thres;SET("BORDER":1)
4390 CONTROL @Thres;SET("VISIBLE":1)
4400 !
4410 !
4420 ! 5) Definition of view panel apply and stop pushbuttons
4430 ASSIGN @Astart TO WIDGET "PUSHBUTTON";PARENT @Mainpanel
4440 CONTROL @Astart;SET("VISIBLE":0)
4450 CONTROL @Astart;SET("X":455)
4460 CONTROL @Astart;SET("Y":270)
4470 CONTROL @Astart;SET("HEIGHT":22)
4480 CONTROL @Astart;SET("WIDTH":165)
4490 CONTROL @Astart;SET("BORDER":0)
4500 CONTROL @Astart;SET("LABEL":"Start Analysis")
4510 CONTROL @Astart;SET("SENSITIVE":1)
4520 CONTROL @Astart;SET("VISIBLE":1)
4530 ASSIGN @Astop TO WIDGET "TOGGLEBUTTON";PARENT @Mainpanel
4540 CONTROL @Astop;SET("VISIBLE":0)
4550 CONTROL @Astop;SET("X":455)
4560 CONTROL @Astop;SET("Y":297)
4570 CONTROL @Astop;SET("HEIGHT":22)
4580 CONTROL @Astop;SET("WIDTH":165)
4590 CONTROL @Astop;SET("BORDER":0)
4600 CONTROL @Astop;SET("LABEL":"Stop Analysis")
4610 CONTROL @Astop;SET("VALUE":0)
4620 CONTROL @Astop;SET("SENSITIVE":0)
4630 CONTROL @Astop;SET("VISIBLE":1)
4641 ASSIGN @Dstop TO WIDGET "TOGGLEBUTTON";PARENT @Mainpanel
4642 CONTROL @Dstop;SET("VISIBLE":0)
4643 CONTROL @Dstop;SET("X":455)
4644 CONTROL @Dstop;SET("Y":350)
4645 CONTROL @Dstop;SET("HEIGHT":22)
4646 CONTROL @Dstop;SET("WIDTH":165)
4647 CONTROL @Dstop;SET("BORDER":0)
4648 CONTROL @Dstop;SET("LABEL":"Freeze Display")
4649 CONTROL @Dstop;SET("VALUE":0)
4650 CONTROL @Dstop;SET("SENSITIVE":0)
4651 CONTROL @Dstop;SET("VISIBLE":1)

```



```

4652 ASSIGN @Dfile TO WIDGET "PUSHBUTTON";PARENT @Mainpanel
4662     CONTROL @Dfile;SET("VISIBLE":0)
4672     CONTROL @Dfile;SET("X":455)
4682     CONTROL @Dfile;SET("Y":324)
4692     CONTROL @Dfile;SET("HEIGHT":22)
4702     CONTROL @Dfile;SET("WIDTH":165)
4712     CONTROL @Dfile;SET("BORDER":0)
4722     CONTROL @Dfile;SET("LABEL":"Data File")
4732     CONTROL @Dfile;SET("SENSITIVE":1)
4742     CONTROL @Dfile;SET("VISIBLE":1)
4752 !
4762 !
4772 ! 6) Definition of notes
4782 ASSIGN @Notest TO WIDGET "PANEL";PARENT @Mainpanel
4792     CONTROL @Notest;SET("VISIBLE":0)
4802     CONTROL @Notest;SET("X":255)
4812     CONTROL @Notest;SET("Y":415)
4822     CONTROL @Notest;SET("HEIGHT":40)
4832     CONTROL @Notest;SET("WIDTH":360)
4842     CONTROL @Notest;SET("BORDER":1)
4852     CONTROL @Notest;SET("VISIBLE":1)
4862 ASSIGN @Nlabel TO WIDGET "LABEL";PARENT @Mainpanel
4872     CONTROL @Nlabel;SET("VISIBLE":0)
4882     CONTROL @Nlabel;SET("X":265)
4892     CONTROL @Nlabel;SET("Y":405)
4902     CONTROL @Nlabel;SET("HEIGHT":20)
4912     CONTROL @Nlabel;SET("WIDTH":140)
4922     CONTROL @Nlabel;SET("BORDER":0)
4932     CONTROL @Nlabel;SET("VALUE":"Notes or Comments")
4942     CONTROL @Nlabel;SET("JUSTIFICATION":"CENTER")
4952     CONTROL @Nlabel;SET("VISIBLE":1)
4962 !
4972 !
4982 ! 6a) Definition of notes edit boxes
4992 ASSIGN @Notes TO WIDGET "STRING";PARENT @Notest
5002     CONTROL @Notes;SET("VISIBLE":0)
5012     CONTROL @Notes;SET("X":5)
5022     CONTROL @Notes;SET("Y":10)
5032     CONTROL @Notes;SET("HEIGHT":20)
5042     CONTROL @Notes;SET("WIDTH":345)
5052     CONTROL @Notes;SET("BORDER":1)
5062     CONTROL @Notes;SET("VISIBLE":1)
5072 !
5082 ! 7) Definition of Alpha
5092 ASSIGN @Alphaw TO WIDGET "PANEL";PARENT @Mainpanel
5102     CONTROL @Alphaw;SET("VISIBLE":0)
5112     CONTROL @Alphaw;SET("X":255)
5122     CONTROL @Alphaw;SET("Y":370)
5132     CONTROL @Alphaw;SET("HEIGHT":40)
5142     CONTROL @Alphaw;SET("WIDTH":190)
5152     CONTROL @Alphaw;SET("BORDER":1)
5162     CONTROL @Alphaw;SET("VISIBLE":1)
5172 ASSIGN @Alphal TO WIDGET "LABEL";PARENT @Mainpanel
5182     CONTROL @Alphal;SET("VISIBLE":0)
5192     CONTROL @Alphal;SET("X":265)
5202     CONTROL @Alphal;SET("Y":360)
5212     CONTROL @Alphal;SET("HEIGHT":20)
5222     CONTROL @Alphal;SET("WIDTH":60)
5232     CONTROL @Alphal;SET("BORDER":0)
5242     CONTROL @Alphal;SET("VALUE":"Alpha")
5252     CONTROL @Alphal;SET("JUSTIFICATION":"CENTER")
5262     CONTROL @Alphal;SET("VISIBLE":1)
5272 !
5282 !
5292 ! 7a) Definition of alpha edit boxes
5302 ASSIGN @Alphe TO WIDGET "STRING";PARENT @Alphaw
5312     CONTROL @Alphe;SET("VISIBLE":0)
5322     CONTROL @Alphe;SET("X":5)
5332     CONTROL @Alphe;SET("Y":10)
5342     CONTROL @Alphe;SET("HEIGHT":20)

```

```

5352 CONTROL @Alphe;SET("WIDTH":160)
5362 CONTROL @Alphe;SET("BORDER":1)
5372 CONTROL @Alphe;SET("VISIBLE":1)
5382 CONTROL @Alphe;SET("VALUE":".00115")
5392 !
5402 RETURN
5412 !
5422 !-----
5432 !-----
5442 !
5452 Constantpower: !
5462 !
5472 !
5482 ! Setup the Keithley
5492 ! -----
5502 REMOTE 716
5512 OUTPUT 716;"F1,0X"
5522 OUTPUT 716;"L110,0"
5532 OUTPUT 716;"POX" !filter 0
5542 OUTPUT 716;"S1X" !med. sampling time
5552 OUTPUT 716;"R1X"
5562 OUTPUT 716;"G4,2,0X"
5563 !
5565 !RESET dmm
5566 REMOTE 722
5568 OUTPUT 722;"*RST"
5569 !
5572 ASSIGN @File TO File$;FORMAT ON
5582 !
5592 OUTPUT @File;Notes$
5602 OUTPUT @File;"Start Date and Time "&DATE$(TIMEDATE)&" "&TIME$(TIMEDATE)
5612 OUTPUT @File;"Finsh Date and Time "&DATE$(TIMEDATE+Tim3)&" "&TIME$(TIMEDATE+Tim3)
5622 OUTPUT @File;"P1 inital = "&Lev1$&" W"
5632 OUTPUT @File;"P1 lenght = "&Tim1$
5642 OUTPUT @File;"P1 = P1' * "&Fac1$&" + "&Add1$
5652 OUTPUT @File;"P2 inital = "&Lev2$&" W"
5662 OUTPUT @File;"P2 lenght = "&Tim2$
5672 OUTPUT @File;"P2 = P2' * "&Fac2$&" + "&Add2$
5682 OUTPUT @File;"Data compression senitivity = "&Sen1$&" %"
5692 OUTPUT @File;"Alpha = "&Alpha$&" ohms/'c"
5702 OUTPUT @File;"Room Tempure = "&Rtemp$&" 'c"
5712 OUTPUT @File;"Max power threshold = "&Thres$&" W"
5722 OUTPUT @File;"Total time = "&Tim3$
5732 OUTPUT @File;"Time is seconds",",Set power in Watts",",,Power realized in
Watts",",,,Resistance in ohms",",,,,Tempature",",,,,,Comments"
5742 !
5752 Pset=Lev1
5762 Psetlast=Lev1
5772 IF Fac2=0 THEN
5782 Lev2=Add2
5792 ELSE
5802 Lev2=(Lev2-Plu2)/Fac2
5812 END IF
5813 Psetsign=Pset/ABS(Pset)
5814 Pset=ABS(Pset)
5815 Psetlast=Pset
5816 Psetlastsign=Psetsign
5818 Psetold=Pset
5819 Psetoldsign=Psetsign
5822 !
5832 !----- Determine the initial values
5842 Ipolyinit=.0001
5852 Temp$="B"&VAL$(Ipolyinit)&","0,0"
5862 OUTPUT 716;Temp$
5872 OUTPUT 716;"N1X"
5882 OUTPUT 716;"H0X"
5892 ENTER 716;Meas$
5902 Vpoly=VAL(Meas$)
5912 Rpoly=Vpoly/Ipolyinit
5922 Rpolylast=Rpoly

```

```

5932 Rplot(1)=1
5942 Rpolyroom=Rpoly
5952 !
5962 IF Alph=0. THEN
5972     Ipoly=SQRT(Pset/Rpoly)*Psetsign !first valid value of Ipoly
5982 ELSE
5992     Atem=(((Rpoly/Rpolyroom)-1)/Alph)+Rtem
6002     Ipoly=SQRT(Pset/(Rpolyroom*(1+Alph*(Pset*(Atem/(Vpoly*Ipolyinit))-
Rtem))))*Psetsign
6012     Atemold=Atem
6022 END IF
6032 Temp$="B"&VAL$(Ipoly)&","0,0"
6042 !
6052 !
6062 !
6072 !----- Determine the starting time
6082 Newtime=0
6092 Oldtime=0
6102 Savetime=0
6112 Pulsetime=0
6122 Pulse=1
6132 Account=2
6142 Accountupper=36+1
6152 Runningave=0.
6162 Rsetflag=1
6172 Stopflag=0
6182 Thresflag=0
6192 Timevalue(1)=0
6202 !
6212 IF Tim3/8640<10 THEN
6222     Plotmax=10 !min 10 for plotmax
6232 ELSE
6242     Plotmax=Tim3/8640
6252 END IF
6262 !
6272 !
6282 Inittime=TIMEDATE
6292 Pulsestart=Inittime
6302 Plottime=Inittime
6303 !
6305 !dmm start value
6306 OUTPUT 722;"MEAS:VOLT:DC?"
6307 ENTER 722;Id
6308 !
6312 OUTPUT @File;Newtime,0,(Ipolyinit*Vpoly),Rpoly,Id,Atem,"Start"
6322 Ipolyold=Ipoly
6332 Vpolyold=Vpoly
6342 Rpolyold=Rpoly
6343 Idold=Id
6352 !
6362 !
6372 Keithleyloop: !
6382 !
6392 ! Start the Constant Power Loop
6402 ! -----
6412 !
6422 OUTPUT 716;Temp$
6432 OUTPUT 716;"HOX"
6442 ENTER 716;Meas$
6443 !
6445 !dmm measurement
6446 OUTPUT 722;"MEAS:VOLT:DC?"
6447 ENTER 722;Id
6448 !
6452 Oldtime=Newtime
6462 Newtime=TIMEDATE-Inittime
6472 Pulsetime=TIMEDATE-Pulsestart
6482 Vpoly=VAL(Meas$)
6492 Rpoly=Vpoly/Ipoly
6502 !

```

```

6512 IF Rsetflag=1 THEN
6522   Rsetflag=0
6532   Rinit=Rpoly
6542 END IF
6552 IF ABS(Vpoly*Ipoly)>Thre THEN
6562   OUTPUT @File;Oldtime,Psetlast*Psetlastsign,(Vpolyold*Ipolyold),Rpolyold,Idold
6572   OUTPUT @File;Newtime,Pset*Psetsign,(Vpoly*Ipoly),Rpoly,Id,"Max Power exceeded:
Analysis terminated!"
6582   Thresflag=1
6592   GOTO Thresdone
6602 END IF
6603 !
6617 !
6622 ! Determine if power has changed by user given percent
6623 Sen=Seni/100
6632 IF ABS((Psetlast-Vpoly*Ipoly)/Psetlast)>Sen OR ABS((Rpolylast-Rpoly)/Rpolylast)>Sen
OR ABS((Idold-Id)/Idold)>Sen OR Psetsign<>Psetoldsign THEN
6642   IF NOT (Savetime=Oldtime) THEN
6652     OUTPUT
@File;Oldtime,Psetlast*Psetlastsign,(Vpolyold*Ipolyold)*Psetlastsign,Rpolyold,Idold
6662     END IF
6672     Rpolylast=Rpoly
6682     Savetime=Newtime
6692     Psetlast=Pset
6693     Psetlastsign=Psetsign
6694     !
6696     !REMOTE 722
6697     !OUTPUT 722;"MEAS:VOLT:DC?"
6698     !ENTER 722;Id
6699     !LOCAL 722
6702     OUTPUT @File;Newtime,Pset*Psetsign,(Vpoly*Ipoly)*Psetsign,Rpoly,Id
6712   END IF
6722   !
6732   Rpolyold=Rpoly
6742   Vpolyold=Vpoly
6752   Ipolyold=Ipoly
6762   Idold=Id
6772   !
6782   Ipoly=SQRT(Pset/Rpoly)*Psetsign
6792   IF Pulse=1 AND Pulsetime>Tim1 THEN
6802     Pulse=2
6812     Psetold=Pset
6813     Psetoldsign=Psetsign
6822     Pset=Lev2*Fac2+Plu2
6823     Psetsign=Pset/ABS(Pset)
6824     Pset=ABS(Pset)
6832     IF Pset<.0001 THEN
6842       Pset=.0001
6852     END IF
6862     Lev2=Pset*Psetsign
6872     Pulsestart=TIMEDATE-(Pulsetime-Tim1)
6882     Pulsetime=0
6892     IF Alph=0 THEN
6902       Ipoly=SQRT(Pset/Rpoly)*Psetsign !first valid value of Ipoly
6912     ELSE
6922       Atem=(((Rpoly/Rpolyroom)-1)/Alph)+Rtem)
6932       Ipoly=SQRT(Pset/(Rpolyroom*(1+Alph*(Pset*(Atem/(Vpoly*Ipolyold))-
Rtem))))*Psetsign
6942       IF ABS((Atemold-Atem)/Atemold)*100>Seni THEN
6952         OUTPUT
@File;Newtime,Psetold*Psetoldsign,(Vpoly*Ipolyold)*Psetoldsign,Rpoly,Id,Atem
6962         Atemold=Atem
6972       END IF
6982     END IF
6992   END IF
7002   IF Pulse=2 AND Pulsetime>Tim2 THEN
7012     Pulse=1
7022     Psetold=Pset
7023     Psetoldsign=Psetsign
7032     Pset=Lev1*Fac1+Plu1

```

```

7033 Psetsign=Pset/ABS(Pset)
7034 Pset=ABS(Pset)
7042 IF Pset<.0001 THEN
7052     Pset=.0001
7062 END IF
7072 Lev1=Pset*Psetsign
7082 Pulsestart=TIMEDATE-(Pulsetime-Tim2)
7092 Pulsetime=0
7102 IF Alph=0 THEN
7112     Ipoly=SQRT(Pset/Rpoly)*Psetsign !first valid value of Ipoly
7122 ELSE
7132     Atem=(( (Rpoly/Rpolyroom)-1)/Alph)+Rtem
7142     Ipoly=SQRT(Pset/(Rpolyroom*(1+Alph*(Pset*(Atem/(Vpoly*Ipolyold))-
Rtem))))*Psetsign
7152     IF ABS((Atemold-Atem)/Atemold)*100>Seni THEN
7162         OUTPUT
@File;Newtime,Psetold*Psetoldsign,(Vpoly*Ipolyold)*Psetoldsign,Rpoly,Id,Atem
7172         Atemold=Atem
7182     END IF
7192 END IF
7202 END IF
7212 !
7222 Temp$="B"&VAL$(Ipoly)&","0,0"
7232 !
7242 IF TIMEDATE-Plottime>=Plotmax THEN
7252     Plottime=TIMEDATE
7262     Rplot(Acount)=Rpoly/Rinit
7272     Timevalue(Acount)=Newtime
7273     STATUS @Dstop;RETURN("VALUE":Stopdis)
7274     IF Stopdis=0 THEN
7282         CONTROL @Plot;SET("POINT CAPACITY":Acount)
7292         CONTROL @Plot;SET("X DATA":Timevalue(*))
7302         CONTROL @Plot;SET("Y DATA":Rplot(*))
7303     END IF
7312     Runningave=Runningave+Rplot(Acount)
7322     Acount=Acount+1
7332     IF Acount>Acountupper THEN
7342         Rplot(Acount-36)=Runningave/36.
7352         Runningave=0.
7362         Acountupper=Acountupper+1
7372         Acount=Acountupper-36+1
7382     END IF
7392 END IF
7402 STATUS @Astop;RETURN("VALUE":Stopflag)
7412 IF Stopflag=1 THEN
7422     OUTPUT @File;Oldtime,Psetlast,(Vpolyold*Ipolyold),Rpolyold,Idold
7432     OUTPUT @File;Newtime,Pset,(Vpoly*Ipoly),Rpoly,Id,"Analysis terminated by User"
7442     GOTO Thresdone
7452 END IF
7462 IF Newtime>Tim3 THEN
7472     GOTO Keithleydone
7482 END IF
7492 GOTO Keithleyloop
7502 !
7512 Keithleydone: !
7522 OUTPUT @File;Newtime,Pset,(Vpolyold*Ipolyold),Rpolyold,Idold,"end"
7532 !
7542 Thresdone: !
7552 OUTPUT 716;"NOX"
7562 LOCAL 716
7563 LOCAL 722
7582     CONTROL @Plot;SET("POINT CAPACITY":Acount-1)
7592     CONTROL @Plot;SET("X DATA":Timevalue(*))
7602     CONTROL @Plot;SET("Y DATA":Rplot(*))
7603 RETURN
7612 END

```

## Appendix C

### Automated pressure measurement system program

This is a typical source code to measure the pressure by the input power change when the photodetector output is constrained at a certain value. Different micro-radiator may require different calibration equations for a better accuracy.

```
10 !-----!
20 !-----!
30 REAL Pd,Pd1,R,Ipolyinit,Vpoly,Rpoly,Pinit,P,P1,Ra,Ra1,Pres,Pres1
31 REAL Dif,Ipoly
40 DIM Temp$(50)
45 !Pop-up questions:
50 INPUT "PHOTODETECTOR SIGNAL PD=? (uA)",Pd
60 Pd1=Pd
70 INPUT "READY TO MEASURE PRESSURE?",R$
80 IF R$="N" THEN
90 PRINT "ONCE YOU'RE READY, RUN AGAIN"
100 END IF
110 IF R$="Y" OR R$="" THEN
120 PRINT "PLEASE WAIT ..."
130 END IF
140 !SETUP KEITHLEY AND DMM
150 REMOTE 716
160 OUTPUT 716;"F1,0X"
170 OUTPUT 716;"L110,0"
180 OUTPUT 716;"P0X"
190 OUTPUT 716;"S1X"
200 OUTPUT 716;"R1X"
210 OUTPUT 716;"G4,2,0X"
220 !RESET DMM
230 REMOTE 722
240 OUTPUT 722;"*RST"
250 !Measure room temperature resistance
260 Ipolyinit=.0001
270 Temp$="B"&VAL$(Ipolyinit)&","0,0"
280 OUTPUT 716;Temp$
290 OUTPUT 716;"N1X"
300 OUTPUT 716;"H0X"
310 ENTER 716;Meas$
320 Vpoly=VAL(Meas$)
330 Rpoly=Vpoly/Ipolyinit
335 !Initial heating power
340 Pinit=.005
350 Ipoly=SQRT(Pinit/Rpoly)
360 Temp$="B"&VAL$(Ipoly)&","0,0"
370 OUTPUT 716;Temp$
380 OUTPUT 716;"H0X"
390 ENTER 716;Meas$
400 Vpoly=VAL(Meas$)
410 P=Ipoly*Vpoly
```

```

420 OUTPUT 722;"MEAS:VOLT:DC?"
430 ENTER 722;Ral
440 Dif=ABS(Ral+Pd1)
450 Ra=ABS(Ral)
455 !Check difference, use big step if difference is big
460 IF Dif<=.1 THEN
465 ! Check if getting close to the constant value
470 IF Dif<=.05 THEN
480 P1=P*1000
490 !Pres=-.0843*P1*P1*P1*P1+8.6107*P1*P1*P1-216.99*P1*P1+2143.9*P1-7213
500 IF P1>=33.89 THEN
510 !Pres1=.0014*P1*P1*P1*P1*P1*P1-
.1942*P1*P1*P1*P1*P1+10.772*P1*P1*P1*P1
520 !Pres=Pres1-298.94*P1*P1*P1+4319.6*P1*P1-30304*P1+80195
531 Pres=-.0843*P1*P1*P1*P1+8.6107*P1*P1*P1-216.99*P1*P1+2143.9*P1-7213
532 GOTO 572
534 END IF
542 IF P1<33.89 THEN
552 Pres=.0143*P1*P1*P1*P1-.4553*P1*P1*P1+7.858*P1*P1-31.748*P1-21.043
562 END IF
572 PRINT "POWER=",P1
582 PRINT "PRESSRE=",Pres
592 GOTO 802
602 END IF
612 IF Ra>Pd1 THEN
622 Ipoly=Ipoly-1.E-6
632 GOTO 360
642 END IF
652 IF Ra<Pd1 THEN
662 Ipoly=Ipoly+1.E-6
672 GOTO 360
682 END IF
692 END IF
702 IF Dif>.1 THEN
712 IF Ra>Pd1 THEN
722 Ipoly=Ipoly-1.E-5
732 GOTO 360
742 END IF
752 IF Ra<Pd1 THEN
762 Ipoly=Ipoly+1.E-5
772 GOTO 360
782 END IF
792 END IF
802 OUTPUT 716;"NOX"
810 ! reset SMU and DMM
812 LOCAL 716
822 LOCAL 722
832 END

```

## Appendix D

### ANSYS Input File

This is the input file for building the numerical model in ANSYS to simulate the temperature profile of micro-radiator. The data are directly extracted from L-Edit.

```
/title, CMOS Micro-radiator
/units, si
/prep7
!
k,1,147.50, 160.00
k,2, 159.00, 160.00
k,3, 159.00, 150.00
k,4, 152.50, 150.00
k,5, 61.00, 60.00
k,6, 61.00, 70.00
k,7, 67.50, 70.00
k,8, 72.50, 60.00
k,9, 142.50, 65.00
k,10, 147.50, 65.00
k,11, 137.50, 60.00
k,12, 152.50, 60.00
k,13, 122.50, 65.00
k,14, 127.50, 65.00
k,15, 117.50, 60.00
k,16, 132.50, 60.00
k,17, 102.50, 65.00
k,18, 107.50, 65.00
k,19, 97.50,60.00
k,20, 112.50, 60.00
k,21, 82.50, 65.00
k,22, 87.50, 65.00
k,23, 77.50, 60.00
k,24, 92.50, 60.00
k,25, 127.50, 160.00
k,26, 142.50, 160.00
k,27, 132.50, 155.00
k,28, 137.50, 155.00
k,29,107.50, 160.00
k,30, 122.50, 160.00
k,31, 112.50, 155.00
k,32, 117.50, 155.00
k,33, 87.50, 160.00
k,34, 102.50, 160.00
k,35, 92.50, 155.00
k,36, 97.50, 155.00
k,37,67.50, 160.00
```



k,38, 82.50, 160.00  
k,39, 72.50, 155.00  
k,40, 77.50, 155.00  
k,41, 50.00, 170.00  
k,42, 155.00, 170.00  
k,43, 208.00, 220.00  
k,44, 0.00, 0.00  
k,46, 0.00, 12.00  
k,47, 50.00, 65.00  
k,48, 220.00, 220.00  
k,50, 170.00, 155.00  
k,51, 220.00, 202.00  
k,52, 170.00, 50.00  
k,53, 65.00, 50.00  
k,54, 18.00, 0.00  
k,55, 147.50, 165.00  
k,56, 156.50, 165.00  
k,57, 72.50, 55.00  
k,58, 63.50, 55.00  
k,59, 220.00, 211.00  
k,60, 214.00, 220.00  
k,61, 9.00, 0.00  
k,62, 0.00, 6.00  
k,63, 0.0, 220.0  
k,64,220.0,0.0

!  
l,1, 2  
l, 3, 2  
l, 4, 3  
l, 5, 6  
l, 6, 7  
l, 5, 8  
l, 9, 10  
l, 11, 12  
l, 13, 14  
l, 15, 16  
l, 17, 18  
l, 19, 20  
l, 21, 22  
l, 23, 24  
l, 25, 26  
l,27, 28  
l,29, 30  
l,31, 32  
l,33, 34  
l,35, 36  
l,37, 38  
l,39, 40  
l,10, 1  
l,12, 4

l,19, 36  
l,17, 34  
l,23, 40  
l,21, 38  
l,18, 29  
l,20, 31  
l,14, 25  
l,16, 27  
l,15, 32  
l,13, 30  
l,11, 28  
l,9, 26  
l,22, 33  
l,24, 35  
l,7, 37  
l,8, 39  
l,41, 42  
l,42, 43  
l,46, 47  
l,47, 41  
l,50, 51  
l,52, 50  
l,53, 52  
l,54, 53  
l,1,55  
l,55, 56  
l,57, 8  
l,58, 57  
l,3,59  
l,56, 60  
l,61, 58  
l,62, 6  
l,44,61  
l,61,54  
l,44,62  
l,62,46  
l,48,60  
l,60,43  
l,48,59  
l,59,51  
!

a, 1, 2, 3, 4, 12, 11, 28, 27, 16, 15, 32, 30, 13, 14, 25, 26, 9, 10  
a, 30, 32, 31, 20, 19, 36, 35, 24, 23, 40, 38, 21, 22, 33, 34, 17, 18, 29  
a, 38, 40, 39, 8, 5, 6, 7, 37  
a, 44, 61, 58, 57, 8, 5, 6, 62  
a, 48, 59, 3, 2, 1, 55, 56, 60  
a, 62, 46, 47, 41, 42, 43, 60, 56, 55, 1, 10, 9, 26, 37, 7, 6  
a, 25, 14, 13, 30  
a, 29, 18, 17, 34  
a, 33, 22, 21, 38

a, 61, 54, 53, 52, 50, 51, 59, 3, 4, 12, 11, 28, 27, 16, 8, 57, 58  
a, 15, 32, 31, 20  
a, 19, 36, 35, 24  
a, 23, 40, 39, 8  
a, 63,46,47,41,42,43  
a,54,53,52,50,51,64  
!  
aadd, 1, 2, 3  
aadd, 6, 7, 8, 9  
aadd, 10, 11, 12, 13  
aglue, all  
!  
MP, KXX, 1, 34  
MP, DENS, 1, 2320  
MP, C, 1, 700  
!  
MP, KXX, 2, 1.4  
MP, DENS, 2, 2190  
MP, C, 2, 1400  
!  
MP, KXX, 3, 237  
MP, DENS, 3, 2700  
MP, C, 3, 896  
!  
MP,KXX,4,0.025  
MP,DENS,4,1.21  
MP,C,4,1010  
!  
/eof